DOCTORAL SCHOOL
MEDITERRANEA UNIVERSITY OF REGGIO CALABRIA

DEPARTMENT OF INFORMATION ENGINEERING, INFRASTRUCTURES AND SUSTAINABLE ENERGY
(DIIES)

PHD IN
INFORMATION ENGINEERING

S.S.D. ING-INF/01
XXVIII CYCLE

PHYSICAL AND CHEMICAL SENSORS BASED ON LOW DIMENSIONAL AND BULK CARBON MATERIALS

CANDIDATE
Angela MALARA

ADVISOR
Prof. Francesco Giuseppe DELLA CORTE

COORDINATOR
Prof. Claudio DE CAPUA

REGGIO CALABRIA, FEBRUARY 2016

Finito di stampare nel mese di **Febbraio 2016**

Edizione CSdA Centro Stampa d'Ateneo

Collana *Quaderni del Dottorato di Ricerca in Ingegneria dell'Informazione*
Curatore *Prof. Claudio De Capua*

ISBN 978-88-99352-09-7

Università degli Studi *Mediterranea* di Reggio Calabria
Salita Melissari, Feo di Vito, Reggio Calabria

ANGELA MALARA

PHYSICAL AND CHEMICAL SENSORS BASED ON LOW DIMENSIONAL AND BULK CARBON MATERIALS

The Teaching Staff of the PhD course in
INFORMATION ENGINEERING
consists of:

Claudio DE CAPUA (coordinator)
Raffaele ALBANESE
Giovanni ANGIULLI
Giuseppe ARANITI
Francesco BUCCAFURRI
Giacomo CAPIZZI
Rosario CARBONE
Riccardo CAROTENUTO
Salvatore COCO
Mariantonia COTRONEI
Lorenzo CROCCO
Francesco DELLA CORTE
Lubomir DOBOS
Fabio FILIANOTI
Domenico GATTUSO
Sofia GIUFFRE'
Giovanna IDONE
Antonio IERA
Tommaso ISERNIA
Fabio LA FORESTA
Gianluca LAX
Aime' LAY EKUAKILLE
Giovanni LEONE
Massimiliano MATTEI
Antonella MOLINARO
Andrea MORABITO
Carlo MORABITO
Giuseppe MUSOLINO
Roberta NIPOTI
Fortunato PEZZIMENTI
Nadia POSTORINO
Ivo RENDINA
Francesco RICCIARDELLI
Domenico ROSACI
Giuseppe RUGGERI
Francesco RUSSO
Giuseppe SARNE'
Valerio SCORDAMAGLIA
Domenico URSINO
Mario VERSACI
Antonino VITETTA

Contents

List of Figures

Introduction

Sensors are increasingly impacting the technological innovation, driving the development of the next generation electronic appliances. They can be considered the building block of control systems and are essential in order to interface the surrounding environment with the electronic circuits.

The need of monitoring physical and chemical quantities within a number of application areas, such as robotics, industrial processes, medical diagnostics and environmental controls, has increasingly contributed to the development of a huge number of sensors.

Current research interest is mainly addressed to the development of novel sensors characterized by high performances, small size and low production cost. The increasing demand for faster and more affordable devices is slowly revealing the limits of sensors based on traditional materials. New challenges in terms of increasing complexity, speed and miniaturization have to be faced.

In this thesis, it will be discussed a set of novel chemical and physical sensors. All the considered devices have been developed using carbon-based materials, both in bulk and low dimensional form.

Carbon, among the most abundant elements in the universe, is envisaged as a potential alternative material in electronic applications, meant to be complementary or supporting to traditional ones. It is known for its excellent properties, especially when considered in stable compounds with other elements, such as in silicon carbide (SiC). Indeed, SiC is receiving a lot of attention since it is slowly replacing silicon in harsh environment applications where high performances are needed. Even if conventional electronics greatly advanced throughout the past decades, most of the developed devices are not able to operate in harsh environments, when high temperatures are combined with high-power, high frequency and high doses of radiation. Therefore increasing attention has been devoted to SiC, currently

the most mature among the wide-bandgap semiconductors, well-suited for all those devices devised to operate in harsh conditions. Indeed, SiC has very high breakdown field, outstanding radiation hardness, excellent chemical and mechanical rigidity, good thermal conductivity and as such is an excellent candidate for photo-detection in high- temperature and radiation conditions.

Carbon is able to form several distinct structures not only in its bulk configuration but even more in its low dimensional form. In the age of nanoscience and nanotechnology, nanomaterials have created great excitement and expectations for microelectronics improvement, as well as for other fields, given the multidisciplinary interest. Materials have extremely unique properties when they are considered in the nanoscale, with at least one dimension in the nanometer size. The use of such nanostructured materials in electronic devices requires an accurate control of their properties, mainly dependent on the synthesis methods. Carbon-based nanomaterials, as graphene and nanotubes, are playing a more and more central role in sensing applications, thanks to their outstanding properties and the high surface to volume ratio.

Therefore, chemical sensors for the detection of hazardous substances, likely among the most treated sensing applications, have been realized with graphene and carbon nanotubes. In this thesis a graphene/silicon Schottky diode, with graphene acting as the sensing layer, has been designed and realized for the detection of gaseous NH_3, whereas a metal oxide semiconductor (MOS) structure, based on carbon nanotubes and their hybrid compounds with metal oxides, has instead allowed the monitoring of gaseous H_2. Moreover, the versatility of the synthesized hybrid materials was also proved through the electrochemical sensing of a liquid analyte as H_2O_2.

Finally a physical sensor, able to work in the optical field as an UV photodiode, was realized using a p-i-n structure. The device, designed to act as a flame detector, was entirely realized in SiC, whose excellent properties have been exploited to improve device performance.

The thesis has been arranged in six chapters. Chapters 1-3 are related to chemical sensors based on low dimensional carbon materials, whereas Chapters 4-6 are referred to physical sensors based on bulk carbon. An

overview of the basic physical and electronic operating principles of the devices is presented in Chapter 1 and Chapter 4, for chemical and physical sensors respectively. In Chapter 2 low dimensional carbon materials are presented together with the experimental part related to their synthesis and characterization. In Chapter 5 silicon carbide and its characterization are instead considered. In Chapter 3 and Chapter 6 experimental results for chemical and physical sensors are reported, respectively. The experimental activity here presented was carried out in different laboratories, specifically at the University Mediterranea of Reggio Calabria, the Enea Portici Research Center and the University of Messina.

1
Chemical Sensors

Chemical sensors, due to their simplicity, low cost, small size and ability to be integrated into electronic devices, are extensively used in a variety of fields.
In this chapter the operating mechanisms of the developed sensing devices will be reviewed. The metal/semiconductor Schottky junction and the metal oxide/semiconductor structure will be discussed along with the basic electrochemical principles.

1.1 Introduction

Sensors are increasingly impacting the technological innovation since they are essential to interface the surrounding environment with the electronic circuits, being central to almost all modern control systems.

Advances in sensor technology have provided a vast array of measuring devices that are extensively used within a number of application areas, such as robotics, industrial processes, vehicle monitoring, medical diagnostics, environmental controls, safety and comfort.

Over the past decades, due to their simplicity, small size, low cost and ability to be integrated into electronic devices, chemical sensors have seen an increase in their applications. Basically, a chemical sensor can be defined as a device that transforms chemical information, originated from a chemical reaction of the analyte or from a physical property of the system, into an analytically useful signal [1]. Chemical sensors contain two basic functional units: a receptor part and a transducer part. In the receptor the chemical information is transformed such to be measured by the transducer. The transducer is instead capable of transforming the chemical information about the sample into a useful signal.

The fundamental characteristics of sensing devices are reported in Table 1.

Table 1. 1 Fundamental characteristics of sensors.

Characteristics	*Description*
Accuracy	It defines how correctly the sensor output represents the true value
Resolution	It signifies the smallest incremental change in the measurand that will result in a detectable increment in the output signal
Sensitivity	It is defined as the change in output of the sensor per unit change in the parameter being measured
Linearity	It defines the direct proportionality of the output to the input over its entire range
Response Time	It defines the time taken by a sensor to arrive at a stable value
Dynamic Range	It defines the range of input signals that will result in a meaningful output for the sensor
Selectivity	It defines the ability to measure a single component in the presence of others
Noise	It refers to random fluctuations in the output signal when the measurand is not changing.
Stability	It is the ability to produce the same output value when measuring a fixed input over a period of time
Hysteresis	It is the difference between output readings for the same measurand, when approached while increasing from the minimum value and while decreasing from the maximum value
Drift	It is the gradual change in the response while the measurand concentration remains constant
Reproducibility	It is the ability to reproduce responses

Chemical sensors may be classified according to their operating principle, such as electrical and electrochemical [1]. In electrical devices, i.e. gas sensors, the signal arises from the change of electrical properties, whereas in electrochemical ones, the signal is due to the electrochemical interaction between analyte and electrode.

In the following, the operating mechanisms of the three developed chemical sensors will be reviewed.

1.2 Gas sensing application of a Metal-Semiconductor Schottky diode

The Schottky diode, based on a potential barrier formed at the interface between a metal and a semiconductor material, is one among the most commonly used electronic devices. The rectification property of metal–

semiconductor contacts was discovered by Braun in 1874 but it was just in 1926 that the use as a rectifier diode was proposed by Lilienfeld [2]. The first theory was developed by Mott in 1939 and promptly extended by Schottky and Davydov. Finally, in 1942 Bethe further enhanced the theory introducing the thermionic-emission model which accurately describes the electrical behavior of the junction [3].

Due to its simple structure, a Schottky diode is a basic component for several devices. In particular, it has been widely investigated as a gas sensor and the first ever reported Schottky diode gas sensor, based on a palladium/silicon dioxide/silicon structure, was shown to be able to detect hydrogen [4, 5].

The fabrication of gas-sensitive Schottky barrier diodes simply consists in the deposition of a catalytic metal layer over a semiconductor substrate. Metals are deposited on the semiconductor and function as both a Schottky contact and a catalyst for the dissociation of gas [6]. Most commonly used metals are the transition ones such as platinum, palladium and nichel, whereas among the different semiconductor substrates n-type Si, GaAs and InP are usually employed.

Recently, a new innovative material as graphene has been demonstrated to form junctions with semiconductor materials showing rectifying characteristics and behaving as gas sensors. Till now few works have been reported in literature. Tongay et al. [7] demonstrated that a multi-layer-graphene/n-Si has a modular barrier height if exposed to bromine. Kim et al. [8] described the variation of the main Schottky junction parameters after exposure to various analytes and in the meanwhile assessed the good stability and reproducibility of their devices. Uddin et al. [9] showed that a graphene/Si junction, with functionalized graphene, is 10 times more sensitive to H_2 with respect to a chemiresistor and the sensitivity level is modulated with the reverse applied voltage.

The main novelty of this sort of devices, where graphene operates as a metal, is the tunable Schottky barrier height (SBH), a feature which makes the graphene/semiconductor junction suitable for applications even in other fields such as photo-detection, high-speed communications and solar cells

[10]. Because of graphene outstanding properties in the sensing field, the Schottky junction, herein considered, was proved to act as a performing sensing device.

Previously, metal-semiconductor junction theory and electrical characterization are briefly introduced.

1.2.1 Metal-Semiconductor junction

A metal-semiconductor junction is formed at the interface between a metallic and a semiconductor material. Additional interfacial layers, such as a native oxide, may be contained even if, generally, the presence of those layers and their impact on the electrical properties are not considered for practical reasons. On account of material properties, such as metal and semiconductor work functions, and substrate doping type, metal-semiconductor junctions can be ohmic or rectifying [11].

It is therefore possible to distinguish four combinations of metal-semiconductor junctions, illustrated in Fig. 1.1. For each n- or p- type substrate, the relative values of metal and silicon work functions determine the formation of an ohmic or a rectifying contact, the latter also known as Schottky barrier [3].

The band structure of a rectifying Schottky barrier, formed by a n-type semiconductor and a metal, whose work function is larger than the semiconductor one, will be considered in the following discussion, in analogy to the experimentally realized junction.

The ideal energy band diagram of isolated metal and n-type semiconductor before making contact is shown in Fig. 1.2. The parameters ϕ_m and ϕ_s are the metal and semiconductor work functions, respectively defined as the energy difference between the Fermi level E_F and the vacuum level, the latter used as a reference level. It is also indicated the electron affinity χ, the energy difference between the conduction band E_C and the vacuum level in the semiconductor.

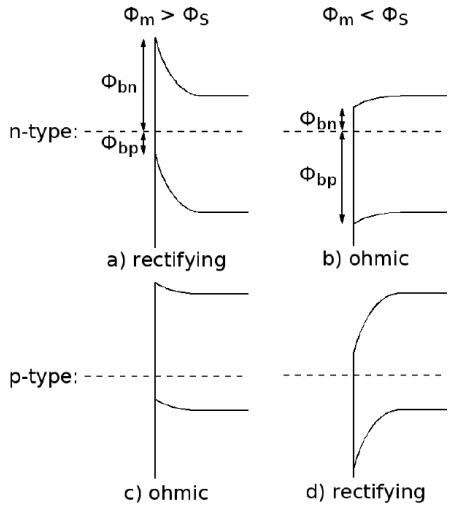

Fig. 1. 1 Band structures of metal-semiconductor contacts. Four combinations of various possible metal work functions ($\boldsymbol{\phi_m > \phi_s}$ and $\boldsymbol{\phi_m < \phi_s}$) on differently doped semiconductor substrates (n- and p-type) are shown [3].

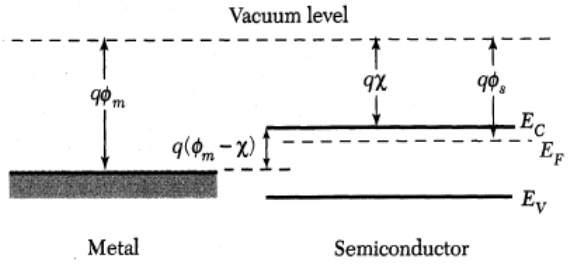

Fig. 1. 2 Energy band diagram of an isolated metal and a n-type semiconductor before contact [3].

Before contact, conduction and valence bands (E_V) in the metal partially overlap, whereas they are separated by a band gap in the semiconductor. When the two materials are put into contact, the Fermi levels in both metal and semiconductor, under thermal equilibrium, must be equal, as well as the vacuum level must be continuous. The new condition is schematically depicted in Fig. 1.3.

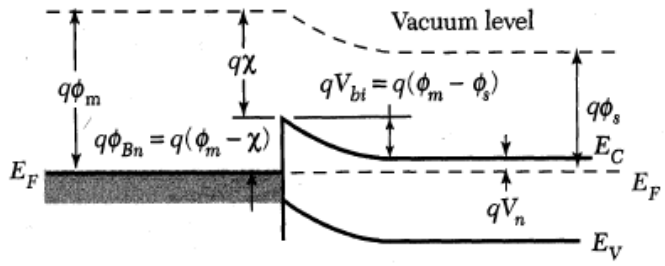

Fig. 1. 3 Energy band diagram of an isolated metal and a n-type semiconductor in contact [3].

A charge transfer from one side to the other takes place. Electrons from the semiconductor flow into the lower energy states in the metal, leaving positively charged donor atoms in the semiconductor. The separation of charges leads to the creation of a space charge region and thus the formation of an electric field in the junction region. qV_{bi} (expressed in eV being q the electric charge) is the built-in potential that is seen by the electrons in the conduction band trying to move into the metal [3]:

$$qV_{bi}=q\phi_{Bn}-qV_n \qquad (1.\ 1)$$

The qV_n value is the distance between the bottom of the conduction band and the Fermi level. The parameter $q\phi_{Bn}$ is the ideal barrier height of the semiconductor contact. This barrier, known as the Schottky barrier, is the difference between the metal work function and the semiconductor electron affinity:

$$q\phi_{Bn}=q\phi_m-q\chi \qquad (1.\ 2)$$

Besides the thermal equilibrium state, different biasing conditions are possible. If a reverse bias is considered, a positive voltage is applied to the semiconductor with respect to the metal. The semiconductor/metal barrier height increases by a voltage V_R, while $q\phi_{Bn}$ remains constant. On the contrary, a forward bias is obtained when a positive voltage is applied to the metal with respect to the semiconductor. In this case the semiconductor/metal barrier V_{bi} reduces, while $q\phi_{Bn}$ remains constant again. Because of the reduction of the barrier height of a voltage V_F, electrons can

easily flow from the semiconductor to the metal. Energy band diagrams are shown in Fig. 1.4.

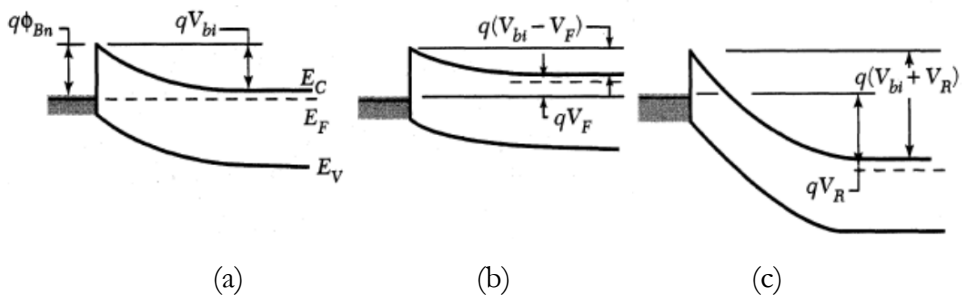

Fig. 1. 4 Different biasing conditions on the energy band diagrams of metal/n-type semiconductor; (a) thermal equilibrium, (b) forward and (c) reverse bias, determining a V_{bi} reduction and increase respectively (adapted from [3]).

The metal is assumed to be a perfect conductor and the charge, transferred to it from the semiconductor, exists in a very narrow region at the metal surface. The extent of the space charge in the semiconductor is W. The generated electric field opposes to the motion of electrons from the semiconductor to the metal. Charge and electric field distributions are shown in Fig. 1.5.

In detail, charge is $\varrho_s = qN_D$ for x <W and $\varrho_s = 0$ for x> W. Electric field decreases linearly with distance until it vanishes at the edge of the depletion layer and has the maximum value located at the physical metal/semiconductor interface.

Therefore the electric field distribution and the voltage across the space charge region, which is represented by the area under the field curve, can be respectively obtained with the following equations:

$$|\varepsilon(x)| = \frac{qN_D}{\epsilon_s}(W-x) = \varepsilon_m - \frac{qN_D}{\epsilon_s}x \qquad (1.3)$$

$$V_{bi}-V = \frac{\varepsilon_m W}{2} = \frac{qN_D W^2}{2\epsilon_s} \qquad (1.4)$$

The depletion-layer width W is expressed as $W = \sqrt{\frac{2\epsilon_s(V_{bi}-V)}{qN_D}}$

in which the voltage V is equal to V_F for forward bias and to $-V_R$ for reverse bias. Finally, it is also possible to evaluate the space-charge density, Q_{SC}, in the semiconductor and the depletion layer capacitance C per unit area given by:

$$Q_{SC}=qN_D W=\sqrt{2q\epsilon_s N_D(V_{bi}-V)} \quad (1.5)$$

$$C=\left|\frac{\partial Q_{SC}}{\partial V}\right|=\sqrt{\frac{q\epsilon_s N_D}{2(V_{bi}-V)}}=\frac{\epsilon_s}{W} \quad (1.6)$$

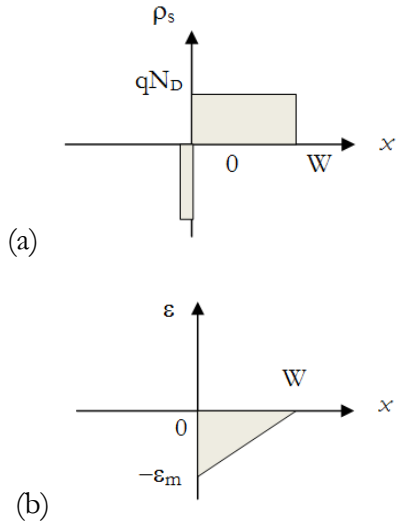

Fig. 1.5 Charge distribution (a) and electric field distribution (b) in a metal semiconductor contact (adapted from [3]).

1.2.2 Characterization of a Metal-Semiconductor junction

Generally, in a simple p-n junction current transport is mainly due to minority carriers. In a Schottky barrier instead, the current transport is mainly due to majority carriers. Moreover, for Schottky diodes operating near room temperature, the dominant transport mechanism is thermionic emission of majority carriers from the semiconductor over the potential barrier into the metal [3].

Thus, considering the thermionic emission process, net current is assumed to be zero, at thermal equilibrium, since the current density is

balanced by two equal and opposite flows. Electrons in the semiconductor flow into the metal and simultaneously an opposing balanced flow of electrons from metal into the semiconductor is generated. These current components, from metal to semiconductor and vice versa, respectively named J_{MS} and J_{SM}, are proportional to the density of electrons at the boundary.

$$|J_{MS}|=|J_{SM}|\propto n_s \tag{1. 7}$$

At the semiconductor surface an electron can be thermionically emitted into the metal if its energy is above the barrier height. Here the semiconductor work function ϕ_s is replaced by ϕ_{Bn}:

$$n_s=N_C e^{\left(-\frac{q\phi_{Bn}}{kT}\right)} \tag{1. 8}$$

where N_c, is the density of states in the conduction band. At thermal equilibrium, being C_1 a proportionality constant:

$$|J_{MS}|=|J_{SM}|=n_s=C_1 N_C e^{\left(-\frac{q\phi_{Bn}}{kT}\right)} \tag{1. 9}$$

when a forward bias V, is applied to the contact, the electrostatic potential difference across the barrier is reduced, and the electron density at the surface increases to:

$$n_s=N_C e^{\left(-\frac{q(\phi_{Bn}-V_F)}{kT}\right)} \tag{1. 10}$$

The current J_{SM} that results from the electron flow out of the semiconductor is therefore altered by the same factor. The flux of electrons from the metal to the semiconductor, however, remains the same because the barrier ϕ_{Bn} remains at its equilibrium value [12]. The net current under forward bias is then:

$$\begin{aligned} J=J_{MS}-J_{SM}&=C_1 N_C e^{\left(-\frac{q(\phi_{Bn}-V_F)}{kT}\right)}-C_1 N_C e^{\left(-\frac{q\phi_{Bn}}{kT}\right)} \\ &=C_1 N_C e^{\left(-\frac{q\phi_{Bn}}{kT}\right)}\left[e^{\frac{qV_F}{kT}}-1\right] \end{aligned} \tag{1. 11}$$

Using the same argument for the reverse-bias condition, the expression for the net current is the same as before, except of V_F that is replaced by $-V_R$.

The coefficient C_1N_C is found to be equal to A^*T^2, where A^* is the effective Richardson constant, and T is the absolute temperature.

Finally, the current-voltage characteristic of a metal-semiconductor contact under thermionic emission condition is:

$$J=J_s\left(e^{\frac{qV}{\eta kT}}-1\right) \quad \text{with} \quad J_s=A^*T^2e^{\left(-\frac{q\phi_{Bn}}{kT}\right)} \tag{1. 12}$$

where J_s is the saturation current density and V, the applied voltage, is positive for forward bias and negative for reverse bias; η is the ideality factor, a dimensionless number which takes into account the phenomena that deviate the characteristic from the ideal behavior, such as the inhomogeneity of the contact area between metal and semiconductor, the variation of SBH due to temperature and voltage, and other effects of the second order. Typically, for commercial diodes, the ideality factor is between 1 and 2; it decreases with temperature and with the increase of the reverse voltage [13].

Ideality factor and saturation current can be calculated by fitting the theoretical I–V equation. By extrapolating the forward I-V curve to V = 0, the slope is η whereas J_s can be easily find out. From its equation it is finally possible to obtain the barrier height.

It should be also considered that in addition to the majority carrier current, due to electrons, a minority carrier current exists in a metal n-type semiconductor contact because of hole injection from the metal to the semiconductor. Anyway, since the minority carrier current is usually orders of magnitude smaller than the majority carrier current, the Schottky diode is generally considered a unipolar device.

In conclusion, it is worthwhile spending few words on the earlier mentioned assumptions. The barrier height was previously assumed not to vary once voltage is applied to a Schottky barrier junction. Actually, the shape and height of the barrier are altered. The barrier becomes more rounded and the height is reduced with increasing electric field [3]. These changes are due to both image force lowering and dipole lowering. They both act by reducing the effective barrier height, which in turn increases carrier transport.

The analysis of a real Schottky junction introduces some uncertainties. For example, the ideality factor takes into account the deviation of the exponential characteristic from its theoretical formulation caused by multiple physical causes, such as destruction of the semiconductor crystal at the interface or the oxide layer between metal and semiconductor. Moreover, it is observed experimentally that the SBH is less than that theoretically described. Another key aspect in the realization of real devices is the presence of a series resistance R_s, as shown in Fig. 1.6. Indeed, in the characterization of a real Schottky junction the voltage V is applied from the outside to the series of the Schottky diode and the resistance series R_s, and is therefore different from the voltage V_d across the diode.

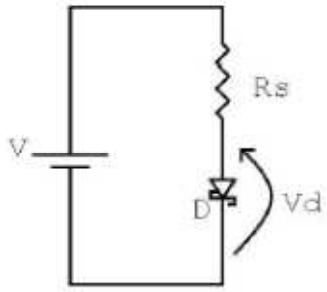

Fig. 1. 6 Equivalent circuit of a Schottky diode.

Therefore, the previously provided model should be refined by taking into account the series resistance:

$$J=J_s\left(e^{\frac{q(V-IR_s)}{\eta kT}}-1\right) \qquad (1.\ 13)$$

that for V> 3kT/q can be approximated by:

$$J=J_s e^{\frac{q(V-IR_s)}{\eta kT}} \qquad (1.\ 14)$$

The characterization methods are pointed towards the extrapolation of the parameters that actually describe a real Schottky diode. The simplest technique is based on the current-voltage characteristic.

From the current-voltage characteristic, η and R_s can be derived being unknown the area of the junction, and even $\phi_B$can be evaluated, in the case A and A* are both known.

The method has been proposed by Cheung [14]. It is possible to rewrite the last equation as:

$$V=R_S I+\eta\phi_B+\frac{kT}{q}\eta\ln\left(\frac{I}{AA^*T^2}\right) \quad (1.15)$$

Differentiating with respect to I and arranging the equation, it is obtained the following:

$$\frac{dV}{d\,\ln I}=R_S I+\frac{kT}{q}\eta \quad (1.16)$$

By Plotting dV/d lnI versus I, a line, whose intercepts is $\eta kT/q$ and slope R_s, is derived. Thus, being known the experimental values I and V, η and R_s can be calculated. It is worthwhile to note that this procedure can be carried out with just a single I-V characteristic, being unknown the area of the junction. Instead, in order to calculate ϕ_B the function H(I) is defined:

$$H(I)=V-\frac{kT}{q}\eta\ln\left(\frac{I}{AA^*T^2}\right) \quad (1.17)$$

By the substitution of equation (1.17) in (1.15) it is obtained:

$$H(I)=R_S I+\eta\phi_B \quad (1.18)$$

where the value of ϕ_B is derived with the previous explained method.

By a linear regression of the experimental data, ϕ_B and R_s are respectively obtained. Furthermore, ϕ_B can be also derived through the values of the reverse saturation current:

$$\phi_B=\frac{kT}{q}\ln\left(\frac{AA^*T^2}{I_s}\right) \quad (1.19)$$

1.3 Metal Oxide Semiconductor (MOS) gas sensor

Metal oxide semiconductor gas sensors are utilized in a variety of different roles. They are relatively inexpensive compared to other sensing technologies, robust, lightweight, long lasting and benefit from high material sensitivity and quick response times [15].

Basically, metal oxide semiconductors, also known as chemoresistive gas sensors, are made of a sensing element, a metal oxide presenting semiconductive properties that is deposited on a heated insulating substrate between two metallic electrodes, as schematically depicted in Fig 1.7. The heating element, usually platinum or one of its alloys, is necessary in order to control and maintain the temperature in the appropriate working conditions.

Since the early 1950s, it has been known that some semiconductor materials modified their resistance, depending on the atmosphere they were in contact with [16]. Later in 1962 it has been first demonstrated, using zinc oxide thin film as sensing layers, that absorption or desorption of a gas on the surface of a metal oxide changes the conductivity of the material [17]. Despite further investigations on the effects achievable with oxide semiconductors modified by the addition of noble metals (e.g., Pt, Pd, Ir, Rh), it was just at the beginning of the 1970s that Taguchi succeeded in the development and commercialization of the first chemoresistive gas sensor device for practical applications using tin dioxide (SnO_2) as the sensitive material [18].

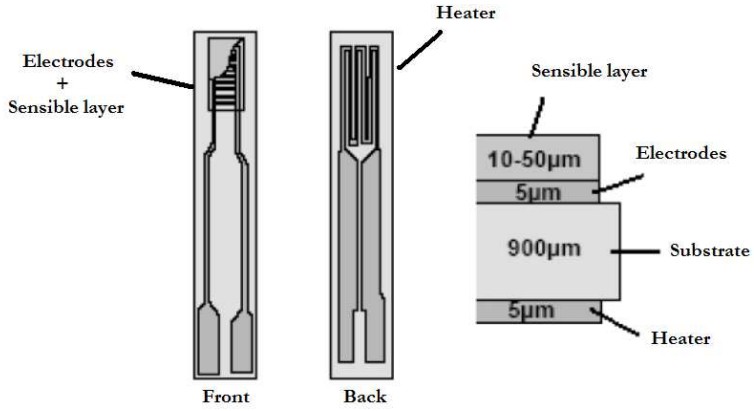

Fig. 1. 7 Semiconductor gas sensor scheme.

Nowadays, the demand for high performance gas sensors with high sensitivity and selectivity, fast response, together with low power

consumption and high device reliability, is continuously increasing. In order to better explain the potentiality of such devices, it is necessary to examine the semiconductive properties of the sensitive element.

Because of their advantages in good thermal and chemical stability, low cost and production flexibility, metal oxides are attractive materials for the fabrication of gas sensing devices. Typically, just few among the most used metal oxide semiconducting film materials are tin oxide (SnO_2), tungsten trioxide (WO_3), zinc oxide (ZnO) and titanium dioxide (TiO_2). These oxides, also used in combination with other materials, are properly synthesized and processed in order to be deposited over the substrate in the form of a layer, whose morphology and compositions are envisaged as the key parameters in determining the chemoresistor properties. The most interesting characteristic of this kind of semiconductor oxides derived by their energy band gap structure, thanks to which little perturbation of the intrinsic state can be traduced in an electrical conductivity change.

The analyte recognition process occurs either at the surface of the sensing element or in the bulk of the material, changing the density of charge carriers available. This change in charge carrier concentration serves to alter the conductivity. Electrodes, also in contact with the sensitive element, measure the change in conductivity which resulted to be related to the analyte concentration.

A lot of factors may affect metal oxide chemosensors performance. The choice of the sensitive materials, which should be endowed with a specific combination of chemical and physical properties, as well as their synthesis procedure, are big issues. Even crystal size and shape play an important role. It is in fact well recognized that by reducing the particle size of the sensing material in the nanometer range, the sensitivity of chemoresistive gas sensors is greatly improved both for the large specific surface offered and for the influence in reducing the surface charge density. Nonetheless, the addition of foreign elements with the role of sensitizers or conductivity modifiers are also some of the factors influencing the sensor response [19]. Lots of factors validate these sensing devices as very efficient. First of all their sensitivity may result really elevate till concentration values of

few part per billion or less [20]. This is mainly due to film structure; in fact, it is highly desirable for metal oxide semiconductor sensors to have a large surface area, so as to adsorb as much of the target analyte as possible on the surface, giving a stronger and more measurable response. What is more, they show good selectivity towards different gaseous species. This is obviously due to material choice; indeed, the same material can even show a different selectivity according to its structure or upon varying the operation temperature.

However the large band gap of metal oxide, hinder their extensive use. To overcome this problem conductive carbonaceous additive have been used. Indeed, CNT, due to their intrinsic electrical properties, appear as an ideal support for various metal oxide sensing layers, i.e. TiO_2. In particular, hybrids composites based on carbon nanotubes have been reported to enhance the sensing performance of TiO_2 sensors, by reducing the working temperature from 300°C as reported by Jun et al. [21] to near room temperature, demonstrated by De Luca et al. [22]. Moreover, addition of CNT to TiO_2 resulted in enhanced sensitivity of the oxide towards analytes [23].

Therefore in this work, an innovative nanostructured material based on TiO_2, carbon nanotubes and platinum was synthesized and tested as sensing element of a metal oxide gas sensor, for the detection of hazardous compounds, as hydrogen.

It is worthwhile to note that in spite of the simple working principle of chemoresistive gas sensor, the gas-sensing mechanism involved is fairly complex. A number of factors should be considered. In the following, a brief discussion of the main aspects is presented.

1.3.1 MOS operating principles

Band theory, applied to metal oxide gas sensors, states that electrons in a crystal can only adopt energy values which stay inside specific bands of energy, the valence band and the conduction band, which characterized three main classes of materials (Fig. 1.8). Insulators have a large gap between the valence and conduction band and electronic conduction does not occur since too much energy is required to promote the electron into the conduction

band. On the contrary, conductors have the Fermi level lying within the conduction band and result always conductive. Semiconductors have instead a sufficiently large energy gap (in the region of 0.5–5.0 eV) so that at energies below the Fermi level, conduction is not observed. Above the Fermi level, electrons can start to occupy the conduction band, resulting in an increase in conductivity. The latter is the needed process for this kind of devices. In fact, the target gas interacts with the surface of the metal oxide film, changing the charge carrier concentration and thus altering the conductivity of the material.

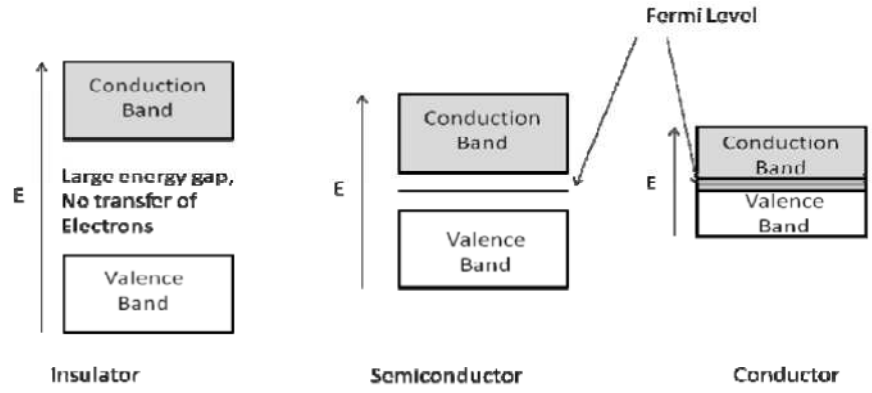

Fig. 1. 8 Schematic band diagram of insulator, semiconductor and conductor materials [15].

The mechanisms that cause gas response are still controversial, but essentially trapping of electrons at adsorbed molecules and band bending induced by these charged molecules are responsible for a change in conductivity [24]. It is possible to distinguish two different mechanisms regarding the electrical conductivity whether the bulk or the surface of the grains are interested. Indeed, the favored gas-sensing mechanism is based on the gas/semiconductor surface interaction which mainly occurs at the grain boundaries of the polycrystalline oxide film. In fact, since the films are deposited at elevated temperatures or annealed after deposition, they typically exhibit a polycrystalline microstructure. These regions have unsaturated bonds which favour the interaction with the gas, and then the variation of conductivity. Thus each crystallite is connected to the other by a grain-boundary, representing a potential barrier, known as Schottky barrier, across which electrons have to move. The height of the potential barrier is

dependent on a variety of parameters, which include film deposition, temperature, gas environment, and metal electrodes [25].

The interaction of the analyte gas with the sensing film can change the barrier height and consequently the number of free carriers. This in turn results in a change of the electrical resistance of the film.

The fundamental mechanism of gas sensing based on metal oxide semiconductor depend on the reaction between the oxygen surface chemical species and the gas molecules, reducing or oxidizing, to be detected. In fact, under an air atmosphere, the oxygen molecules can be absorbed on the surface of the metal oxides and extract electrons from the conduction band, forming oxygen ions at the surface. This will cause a band bending and the formation of an electron depleted region, so called space-charge layer. Reaction of these oxygen species with reducing gases decreases and can reverse the band bending. Then, the Schottky barrier between two grains is lowered and it would be easy for electrons to conduct in the sensing layers through different grains, resulting in an increased conductivity (Fig. 1.9).

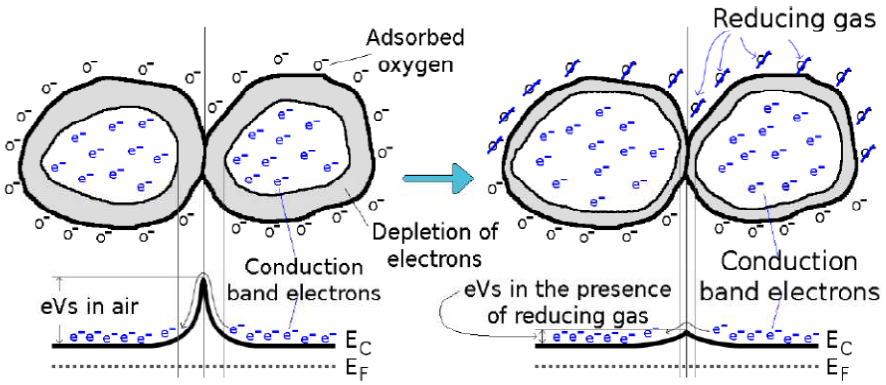

Fig. 1. 9 Schematic representation of the adsorbed oxygen species that create the surface-charge layer, responsible for the intergranular potential barrier that conduction electrons have to overcome.

For a n-type semiconductor the majority charge carriers are electrons and, upon interaction with a reducing gas, an increase in conductivity occurs, while an oxidizing gas decreases it. Conversely, in p-type semiconductor, holes are the majority charge carriers; hence, the opposite effects are observed.

The simplest response model [26] states that the change in resistance is proportional to the concentration of the gas [X] and to a sensitivity parameter A, considered constant for a given material at a given temperature:

$$\frac{R}{R_0} = 1 + A[X] \qquad (1.\ 20)$$

with R and R_0 the resistance after exposure to analyte gas and the baseline resistance, respectively. However it should be considered that the only parts of the material that exhibit a response to the target gas, are the areas where gas can interact at the surface. The material is split into three regions namely the surface, the bulk and the neck or particle boundary (Fig. 1.10).

The distance between the surface and the particle boundary is called the Debye length, the distance at which charge separation can occur. The equation for the response is:

$$G_T = \gamma_{PB}(1 + A[X]) + \frac{1}{\frac{1}{\gamma_B} + \frac{1}{\gamma_S(1 + A[X])}} \qquad (1.\ 21)$$

where $G_T = R_T/R_{T,0}$ is the response, with R_T the total sensor resistance and $R_{T,0}$ the baseline resistance in dry air and γ_{PB}, γ_B,and γ_S are the response to the gas target of the three different regions being $\gamma_x = R_{x,0}/R_{T,0}$ (x denotes particle boundary PB, bulk B or surface S) the ratio of the baseline of x to the total baseline of sensor resistance [15].

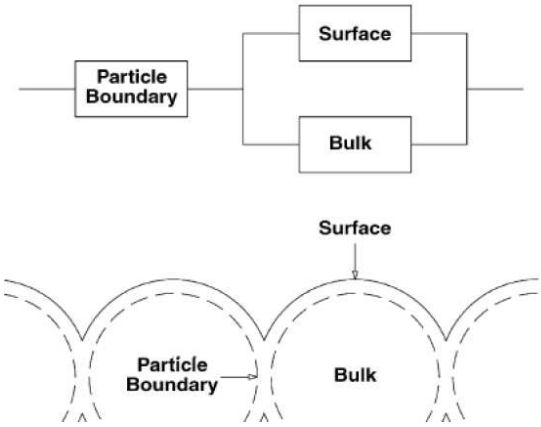

Fig. 1. 10 Materials structure and positions of surface, bulk and particle boundary [26].

Response is directly related to grain and particle boundary size in the material. Indeed, the relative contribution from the three regions can differ. For very small grain sizes, the grain can be considered to contain no bulk area at all and the simpler model is used. If the grains are too much large, the contribution to the resistance or conductivity is negligible, thus surface has a constant resistance.

Generally, when a gas arrives at the surface of a sensor, different interaction mechanisms between the solid surface and gas molecules are possible: it interacts both physically and chemically. Physical adsorption mechanism, known as physisorption, is characterized by weak interaction forces. It simply relies on electrostatic van der Waals interactions. No charge exchange is detected and low temperatures seems to favor the process. The enthalpy of formation of the bonds that characterize the physical adsorption is very small, commonly between 5 - 45 kJ/mol [27]. Chemical adsorption, the so called chemisorptions, in contrast to the previous one, is a chemical adsorption characterized by binding forces of the same order of magnitude as that of the chemical bonds. It occurs a real charge transfer between the adsorbed molecule and the surface of the adsorbent material. The enthalpy of adsorption is in a range of energies between 80-400 kJ/mol [27].

It can be deduced that in physisorption no appreciable useful signal in terms of change of conductivity of the semiconductor material is detected. On the contrary, in the case of chemisorption, characterized by a charge exchange between the adsorbate and adsorbent, significative variation of conductivity is registered.

Usually, an intermediate mechanism between the two previous processes is favored, namely ionosorption. In this case the interaction is of electrostatic nature as in the physisorption, since the adsorbate captures an electron or hole and held it to the surface by electrostatic attraction. Even if exchange of charges takes place, chemical bonds do not occur differently to what happen in chemisorption process.

From an analytical point of few, these phenomena are well described by surface coverage and Lennard-Jones models [27].

1.4 Electrochemical sensors

The history of electrochemical sensors starts with the development of the glass electrode by Cremer in 1906 [28]. Despite this, the first reported electrochemical sensors, used for oxygen monitoring, are dated back to the 1950s. Since then, the increasing need of such devices in a variety of fields led to the development of new performing sensors. Thanks to the existing sensing technologies along with the development of innovative sensor materials, possibilities to develop new generation sensors, always more miniaturized and with much improved performance are emerging.

The purpose of this kind of sensors is to transform the effect of the electrochemical interaction between a target analyte and an electrode/electrolyte interface, into a useful signal. Ideally, such a device is capable of responding continuously and reversibly without perturbing the sample. According to its use, when developing electrochemical sensors some properties such as physical size, geometry and components are usually carefully defined in order to match with the final applications. Even the electrolyte composition as well as the sensing electrode material are selected based on the chemical reactivity of the target analyte.

Currently, electrochemical sensors are being extensively used and play an essential role in the fields of environmental monitoring, disaster prevention, clinical diagnostics and on-site industrial analysis, meet the expanding need for rapid, simple and economic methods of determination of numerous analytes [28].

Recently, great attention has been paid to the research and application of TiO_2 for electrochemical sensors design [29]. In particular, CNT/TiO_2 nanostructures and CNT/TiO_2/Pt nanocomposites are reported to possess excellent electrocatalytic activity towards hydrogen peroxide (H_2O_2), [30]. However, in these works, sophisticated techniques such as electrochemical anodisation, electrochemical deposition or photo induced deposition have been used for the growth of complex nanostructures [31].

A brief introduction on the main used electroanalytical techniques will be presented in the following.

1.4.1 Electrochemical techniques

Electrochemical sensors are based on an electrochemical cell which employs a three-electrode arrangement in a properly electrolyte solution. The processes and factors that affect the transport of charge across the interface between chemical phases, electrodes and electrolyte are considered. Electrochemical sensing usually requires a reference electrode, a counter or auxiliary electrode and a working electrode. A necessary condition is that these electrodes have to be both conductive and chemically stable. The reference electrode is generally made from Ag/AgCl and it is used to maintain a known and stable potential. The working electrode operates as the transduction element in the reaction, while the counter electrode establishes a connection to the electrolytic solution so that a current can be applied to the working electrode [32]. The applied current or potential, among electrodes, determines a charge transport through the electrode by the movement of electrons (and holes) whereas, the electrolyte phase charge is carried by the movement of ions. In electrochemical sensors the applied current or potential may vary according to the operation mode as well as the specific design of the electrochemical cell. Mode selection is often intended to enhance the sensitivity and selectivity of a particular sensor [33].

Electrochemical sensors can be classified according to the signal transduction mode. Reactions are generally detected just in proximity to the electrode surface, therefore electrodes, in terms of material, surface modification and dimensions play a crucial role in the performance of electrochemical sensors.

In detail, the voltammetry technique continuously measures the current resulting from the oxidation or reduction process of an electro-active species in the reaction, at a scanned or fixed potential. Since this implies a varying voltage, common applied methods are cyclic, squarewave and stripping voltammetry. Typically when the current is measured while the electrode is held at constant potentials, this is referred to amperometry a sub-class of voltammetry. The value of the measured current is directly proportional to the bulk concentration of the analyte [32].

In the potentiometry technique, the analytical information is obtained by measuring the accumulation of a charge potential at the working electrode compared to the reference electrode when no significant current flows between them. It provides therefore information about the ion activity in an electrochemical reaction. In this case, the relationship between the concentration and the potential is governed by the Nernst equation:

$$E=E_0+\frac{RT}{nF}\ln\frac{a^0}{a^R} \quad (1.\ 22)$$

where E_0 is the standard electrode potential calculated to the idealized Standard Hydrogen Electrode (SHE) and $a^0$and a^R are the activities of the oxidized and reduced species, *R* is the universal gas constant, T is the absolute temperature in Kelvin degrees, F is the Faraday constant and *n* is the number of moles of electrons exchanged in the electrochemical reaction. As evident, a linear relation exists between the measured potential *E* and the natural logarithm of the activities ratio of reactant and product. The slope value of this curve governs the sensitivity of the potentiometric sensor.

Conductometry technique is based on the measurement of system conductivity in the presence of a given solute concentration. The sensing effect is based on the change of the number of mobile charge carriers in the electrolyte. Conductivity results to be a linear function of the ion concentration. In particular, it has been established that the conductance of a homogeneous solution is directly proportional to the electrode surface and inversely proportional to the distance between the two electrodes [33]. Thus, the conductance of this electrolyte solution, can be expressed as:

$$G=\sigma\frac{A}{L} \quad (1.\ 23)$$

where A is the cross-sectional area, L is the segment of the solution along the electrical field, and σ is the specific conductivity of the electrolyte, quantitatively related to the concentration of the charges of the ionic species.

1.4.2 Faradic and capacitive currents in electrochemical process

The current observed at the working electrode in an electrochemical experiment is generally due to two types of processes occur at electrodes-electrolyte interface. The first current contribute is due to oxidation or reduction reactions, occurring with charges transfer across the electrode-solution interface. Since in these reactions the amount of chemical deposition caused by the flow of current is proportional to the amount of electricity passed, they are governed by Faraday's law and so known as faradic processes. The other current contribute is the capacitive current, also called non-faradic or double-layer current, caused by the charge/discharge of the electrode surface as a result of a potential variation (or by an adsorption process). Capacitive process does not involve any chemical reactions but it only causes accumulation or removal of electrical charges on the electrode and in the electrolyte solution near the electrode. Although charge does not cross the interface, there is always some external capacitive current flowing when the potential, electrode area, or solution composition change. When reactions at an electrode take place both faradic and non faradic processes always occur [34].

Let consider the capacitive current contribute. It is therefore possible to consider an electrode, namely ideal polarized electrode (IPE), at which no charge transfer can occur across the metal-solution interface, regardless of the external potential imposed. When potential is changed, since charge cannot cross the IPE interface, the behavior of the electrode-solution interface is analogous to that of a capacitor, ideally composed of two metal sheets separated by a dielectric material. Its behavior is governed by the equation:

$$\frac{q}{E} = C_d \qquad (1.\ 24)$$

where q is the charge stored on the capacitor, E is the potential across the capacitor and C_d is the capacitance. When a potential is applied across a capacitor, charge will accumulate on its metal plates. The charge on the capacitor consists of an excess of electrons on one plate and a deficiency of electrons on the other.

The electrode-electrolyte interface is an electrical double layer that behaves as a capacitor where accumulation of charges occurs [35]. The capacitance measured at this double layer is termed as double layer capacitance. Thus, this condition can be approximated by an electrical circuit with a resistor, R_s, representing the solution resistance and a capacitor, C_d, representing the double layer (Fig. 1.11). Since C_d is generally a function of potential, the proposed model in terms of circuit elements is strictly accurate only for experiments where the overall cell potential does not change very much. Where it does, approximate results can be obtained using an average C_d over the potential range [36].

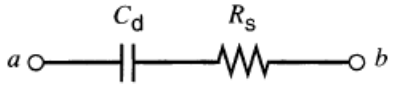

Fig. 1. 11 Double layer equivalent circuit.

The relation between the change in voltage and the current can thus be obtained by the derivative of the previous equation (1.24):

$$i = \frac{dq}{dt} = C_d \frac{dE}{dT} \qquad (1.\ 25)$$

According to the applied voltage or current it is possible to distinguish three typical cases: step of potential, current step and scan of potential.

In the case of step potential it is assumed that voltage is first varied instantly and then maintained constant. The function which describes the variation of the current versus time, is obtained from the solution of the previous equation by imposing the necessary boundary conditions:

$$i = \frac{E}{R_s} e^{-t/R_s C_d} \qquad (1.\ 26)$$

Hence, for a potential step input, there is an exponential decay of the current having a time constant, $\tau = R_s C d$ (Fig. 1.12).

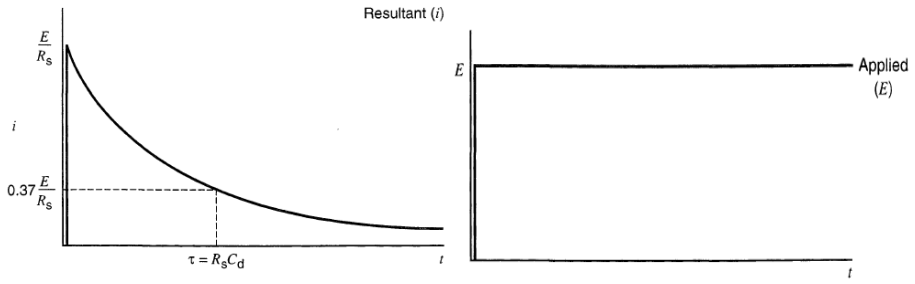

Fig. 1. 12 Current transient resulting from a potential step experiment [36].

When the *RsCd* circuit is charged by a constant current then, with the same equation, a linear solution is obtained:

$$E=i\left(R_s+\frac{t}{C_d}\right) \tag{1.25}$$

For a current step, after an instantaneous increment equal to iR_s, the potential increases linearly with time (Fig. 1.13).

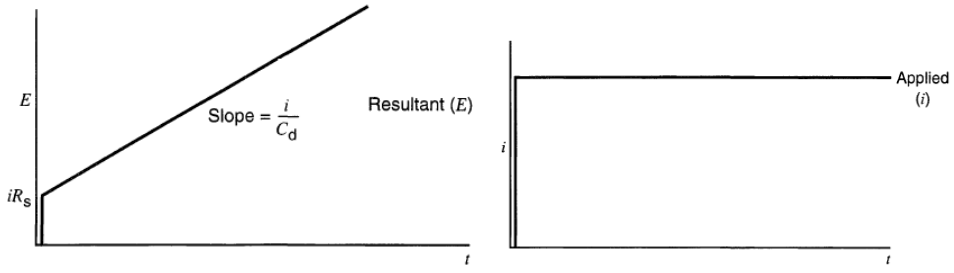

Fig. 1. 13 E-t behavior resulting from a current step experiment [36].

More interestingly, a voltage ramp or linear potential sweep is a potential that increases linearly with time $E = \nu t$ starting at some initial value, assumed to be zero, at a scan rate ν. In this case the solution of the equation is:

$$i=vC_d\left[1-e^{-t/R_sC_d}\right] \tag{1.26}$$

The current rises from zero as the scan starts and attains a stationary value, νCd. This steady-state current can then be used to estimate C_d.(Fig. 1.14).

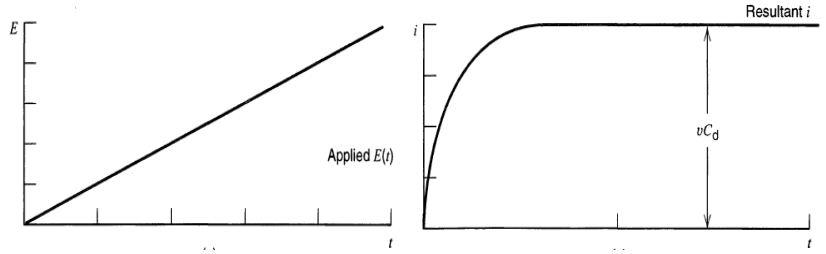

Fig. 1. 14 Current- time behavior resulting from a linear potential sweep applied to an RC circuit [36].

As regard the faradic process, it is possible to correlate the concentration of the analyte species of interest to the faradic current [37]. It is known that the kinetics of the electrode discharge process is mainly governed by two factors: the rate of electron transfer at the electrode surface and the transfer rate of the electro-active species to the electrode surface (mass transport). For this purpose it is necessary to assume the rate of electron transfer almost instantaneous and the kinetics governed by the mass transport only. The flow of material within an electrolytic solution represents a movement of ions or molecules from one location to another within the volume and can be expressed as:

$$v_{mt} = \frac{i}{nFA} = J \qquad (1.27)$$

where i is the faradic current, n the number of electrons in the reaction, F the Farady constant, A the electrode surface, while v_{mt} is the speed of mass transfer per unit area, which coincides with a flow material (J) passing through a unit surface area.

Generally, mass transport can occur in three different modes: convection, migration and diffusion. The mass transport, for a generic species, within a solution can be expressed by the equation of Nernst-Planck that, for a one-dimensional case along a generic x direction can be written as [36]:

$$J_0(x,t) = -D\,\partial C_0(x,t)\,\partial x - zFDC_0RT\,\partial \emptyset(x,t)\,\partial x + C_0 v(x,t) \qquad (1.28)$$

where J_0 (x) is the flow of electro-active species to the generic distance x from the surface, D the diffusion coefficient, ∂C (x) ∂x the gradient

concentration, $\partial\varphi(x)\,\partial x$ the gradient potential, z the charge of the electro-active species, C_0 concentration and v(x) the speed shift of a volume element along the x axis. The first term of the equation is due to diffusion phenomena; the second term takes into account the movement of charged species due to the potential difference between the electrode and the rest of the solution and represents the migration; the third term is the convection and takes account of the speed at which a generic volume of solution moves.

The solution of the Nernst-Planck equation is generally not easy when all three modes of transport are present. For this reason, it is assumed to make negligible the effects of one or more of these forms of transport. Convection is generally due to externally induced mechanical agitation of the solution. To eliminate the influence of convection and its related current, it is possible to keep homogeneous the temperature of the solution and to work in quiescent conditions, especially during the scan potential technique. Migration is the movement of ions due the potential applied to the electrodes. The cations migrating to the cathode (negative electrode) and the anions toward the anode (positive electrode) produce a shift of charges with consequent generation of an electric current. To eliminate the migration effects it is used excess of "support electrolyte". So, within the solution are dissolved other non-electroactive ions in quantities much higher than the analytic species. The addition of a supporting electrolyte in high concentrations causes the most of the current to be transported by such ionic species while the analyte species can arrive to the electrode almost exclusively by diffusion. This simplifies the mathematical treatment of electrochemical systems being able to neglect phenomena due to the migration and convection. Mass transport is reduced to the expression of Fick's law:

$$J_0(x,t) = -\frac{D\partial C_0(x,t)}{\partial x} \tag{1.29}$$

If the concentration of the analyte species varies in time:

$$\frac{\partial C_0(x,t)}{\partial x} = -\frac{D\partial^2 C_0(x,t)}{\partial x^2} \tag{1.30}$$

Then, under the assumption of diffusive process, by combining equation (1.27) with (1.30), the relationship that correlates the faradic current with the concentration gradient can be obtained:

$$i=nFAJ_0(x,t)=-nFAD\partial C_0(x,t)\partial x \qquad (1.31)$$

1.4.3 Electrochemical characterization

Chronoamperometry is an electrochemical technique in which the current from faradic processes occurring at the electrode, because of a potential step, is measured versus time. At t=0 the potential is instantaneously changed to a new value E and current time response is recorded. Its modification arises from the variation of the diffusion layer at the electrode. Nernst [36] stated that it exists a stationary thin layer of solution in contact with the electrode surface and it is there assumed that the transport of material takes place, only by means of diffusive phenomena. In the bulk solution, the analyte concentration is instead maintained at a C_0 value by convective transfer. The current-time dependence is well described by the Cottrell equation [36]:

$$i_F=nFAC_0\sqrt{\frac{D}{\pi t}} \qquad (1.32)$$

being i_F the faradic current, F the Faraday constant, n the number of transferred electrons per molecule, A the electrode area, C_0 the analyte concentration, D the diffusion coefficient and t the time. Basically, current depends on the rate at which the analyte diffuses to the electrode. Moreover for a fixed instant t, the faradic current will depend proportionally on the concentration of the analyte species. In order to ensure the reliability of results, chronoamperometric experiment has to be applied over a broad time interval. In fact, for short times the current mainly consists of a large non faradic component due to the double-layer capacitance charging and decays exponentially with time.

Depending on how the potential is modified in time, different analysis technique exist: Linear Scan Voltammetry (LSV), when potential varies

between a minimum and a maximum, or cyclic voltammetry (CV), when it is varied according to a triangular wave.

Let assume to apply a potential, linearly varying in time, with a scan speed sufficiently slow, between an initial value in which the species is stable and up to a value higher than that of discharge. The obtained i-E curve will have a sigmoidal shape (Fig. 1.15), in which it is possible to distinguish three characteristic features.

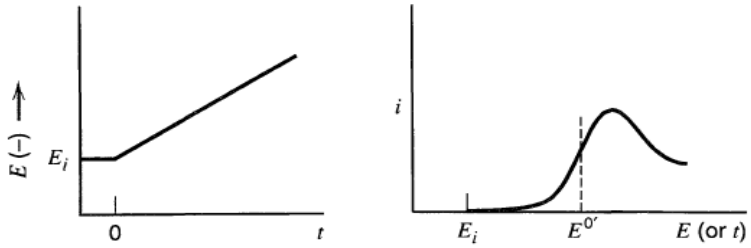

Fig. 1. 15 LSV experiment showing current behavior.

The first part is commonly characterized by a constant trend of the current. Initially, being the potential very far from the one of discharge of the electro-active species, no faradic current is observed. The second stretch is characterized by a rapid increase of the current when the potential imposed on the electrode reaches values close to that of the redox process ($E^{0'}$). Finally, the third portion of the curve, if the scanning of potential is sufficiently slow, will be characterized by a plateau of the current, otherwise by an asymmetric peak profile. This phenomenon can be explained by considering that for high scanning speed, ions discharge near the electrode takes place in a rapid way as to generate a big transfer of electrons in a short time, and then a maximum current. However, due to the rapid consumption of electroactive species, the faradic current decreases generating the classic asymmetrical peak. In this case the most useful parameter for the study of the electrochemical process is represented by the "peak current" i_p. For a reversible system governed by diffusion alone, it is expressed through the Randles-Sevcik equation [38]:

$$i_p=\left(2.69\times10^5\right) n^{3/2} A\, D^{3/2} C_0 v_s^{3/2} \qquad (1.33)$$

Then, at a fixed analyte concentration C_0, the peak current will vary with the square root of the scan speed v_s. Moreover, this parameter, allows to

obtain information on the nature of the process. In general, if the peak current and the velocity square root are proportional, the process can be associated to faradic phenomena, vice versa if there is a linear relationship between them, it will likely be a capacitive processes regarding the double layer charging.

Cyclic voltammetry is one of the most widely used analysis to get useful information. In this case, a triangular potential perturbation is used and the voltage is swept between two values at a fixed rate. The voltage is measured between the reference electrode and the working electrode, while the current is measured between the working electrode and the counter electrode. The obtained measurements are plotted as voltammogram, current versus voltage. Briefly, this is a reversal technique, which involves the sweeping of electrode potential between two limits, at a known sweep rate. At the beginning the working electrode is held at a potential where no electrode reactions occur. During measurement the potential is swept linearly at a rate ν between two limiting potentials. The same sweep rate is normally chosen for the forward and reverse sweep The scan rate is a critical factor since the duration of a scan must provide sufficient time to allow for a meaningful chemical reaction to occur. The corresponding current is recorded as a function of the varying potential. A theoretical cyclic voltammogram for a reversible system is shown in Fig. 1.15. For the cathodic scan (applied potential is decreasing) the current has a negative sign, for the anodic scan (applied potential is increasing) the current has a positive sign. The shape of the voltammogram for a given sample depends not only on the scan rate and the electrode surface, which is different after each adsorption step, but can also depend on the sample concentration.

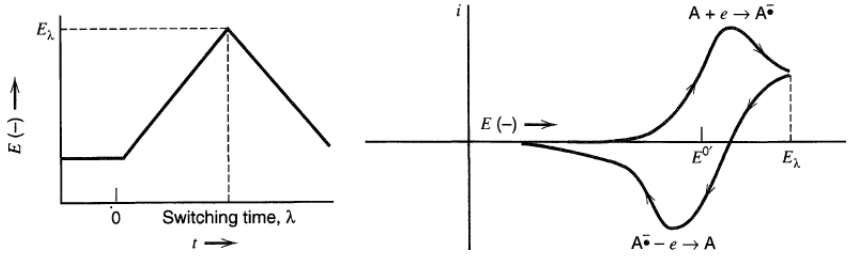

Fig. 1. 16 Cyclic potential sweep and related cyclic voltammogram [36].

2
Low-dimensional carbon-based materials in sensing applications

Carbon, especially in its low-dimensional form is nowadays among the most appealing material. Indeed its allotropes, graphene and nanotubes, are known to be endowed with unique physical and chemical properties which make them suitable for several applications. Because of their extraordinary versatility carbon nanomaterials are playing an important role in nanotechnology and microelectronics, envisaged as the main protagonist of the sensing devices of the future.

The aim of this chapter is to introduce low-dimensional carbon materials, graphene and carbon nanotubes. Firstly, their structures and properties will be pointed out, then synthesis methods and characterization techniques will be briefly discussed. Finally, synthesis and characterization of the sensible materials used for the realization of the devices will be presented.

2.1 Introduction to low-dimensional carbon

In the last years, carbon materials have been widely investigated and the possibility to utilize them in many different applications arises. In the age of nanotechnology, a new light has been casted on carbon, which has been investigated on a different aspect. The low dimensionality of carbon, as well as that of other materials, is indeed an intense object of study [39, 40]. As it is well known bulk materials and nanostructured ones are characterized by very different properties. Thus, a well-known element as carbon, can pay the way to new outstanding properties if regarded in its nanometric dimension.

During years, a number of allotropes was discovered and great attention was given to them. All these materials are made of carbon atoms only, but due to the different ways carbon atoms bond together, they are characterized by great differences in their properties.

Carbon exhibits each possible dimensionality, indeed, it can form structures that are 0-dimensional such as fullerenes, 1-dimensional like carbon nanotubes, 2-dimensional as graphene and finally 3-dimensional as graphite and diamond. Allotropes graphical scheme is shown in Fig. 2.1.

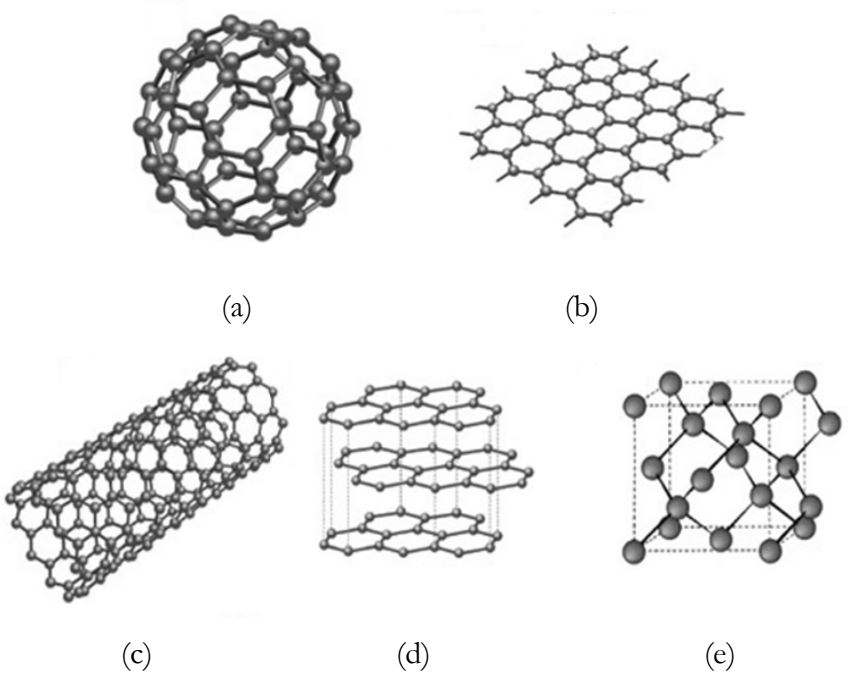

Fig. 2. 1 Allotropes of carbon: (a) fullerene, (b) graphene, (c) carbon nanotube, (d) graphite and (e) diamond.

To better understand the allotropes formation, the electronic structure should be taken into account. Carbon electronic configuration, namely $1s^2 2s^2 2p^2$, indicates that each carbon atom has six electrons that occupy the *1s*, *2s* and *2p* atomic orbitals. In detail, the *1s* orbital contains two electrons, strongly bonded, while the remaining four valence electrons partially filling the *2s* and *2p* orbitals, can participate in bonds formation. The two unpaired electrons of *2p* orbital should form only two bonds; anyway, in order to minimize the system energy, carbon is inclined to maximize the number of formed bonds rearranging the configuration of the valence electrons. Thus, one *2s* electron will be promoted into an empty *2p* orbital forming an excited state. This process, called hybridization (Fig. 2.2), results in the formation of a new hybrid molecular orbital, sp^n, with n assuming the value 1, 2 or 3 on account of the number of *2p* orbitals participating to the mixing.

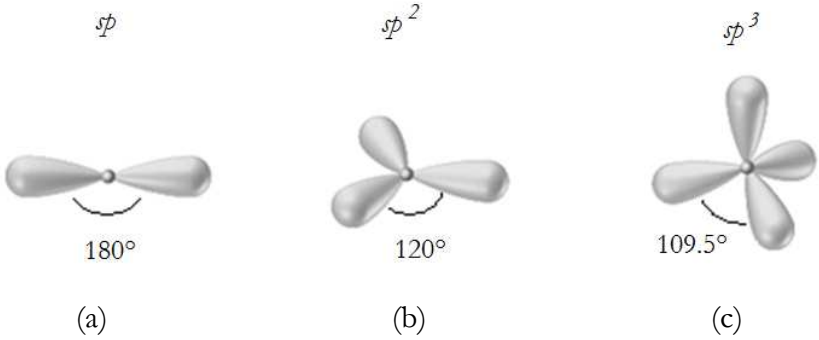

Fig. 2. 2 sp^n hybrids: (a) linear sp, (b) trigonal sp^2 and (c) tetragonal sp^3.

Four sp^3 hybrid orbitals, each filled with only one electron, are formed when one *2s* orbital and three *2p* orbitals are mixed together. Four carbon bonds displayed at an angle of 109.5° in a tetrahedral geometry can be established.

Diamond is the typical three-dimensional structure where all carbon atoms are sp^3 hybridized. The strong covalent bonds between atoms endow diamond with excellent properties. It is indeed characterized by high hardness and thermal conductivity, is transparent to visible light and it is an electrical insulator with a band gap of ~5.5 eV [41].

Another possible hybridization is the sp^2, where one *2s* orbital is mixed with two *2p* orbitals to form three hybrid orbitals. Again, these orbitals will arrange themselves in covalent bonds with angle of 120° in a trigonal planar geometry. The remaining p-type orbital, perpendicular to this plane will form π bonds between the carbon atoms. Graphite is a typical example of sp^2 hybridized carbon atoms characterized by strong σ covalent bonds between atoms in the plane, while the π bonds provide the weak interaction between adjacent layers in the graphitic structure. The single layer, one carbon atom thick is known as graphene. Graphite is an electrical and thermal conductor, and is regarded a good lubricant [42].

The last hybridization consists in mixing one *2s* orbital and one *2p* orbital leading to the formation of two *sp* hybrid orbitals, each filled with only one electron. In this case, covalent bonds are linear with an angle of 180° between the *sp* orbitals. The two remaining p-type orbitals, instead, are perpendicular to each other, forming two π bonds. This is the case of carbyne,

an unstable allotropic form, characterized by a triple bond between each carbon, giving rise to a polymerized carbon chain with very strong bonds.

Among the different allotropes carbon nanotubes and graphene have gained great attention. Owing to their excellent electrical, thermal, chemical and mechanical properties these low dimensional carbon materials have found applications in many different fields such as sensors, energy storage and conversion, drug delivery, field emission devices and nanoscale electronic components [43, 44, 45, 46, 47].

Low dimensional carbon materials have shown potential in gas sensing field as to develop self-contained integrated devices with enhanced sensitivity and selectivity of the chemicals and faster response time. In particular, the very high surface to volume ratio can explain their superior properties if compared to bulk materials, when especially used in the sensing field. Indeed, both graphene and carbon nanotubes are well recognized surface reacting materials as they are composed of entirely surface atoms where adsorbed gas molecules can dramatically alter their electrical properties, even at room temperature.

2.2 Graphene

Graphene, even if theoretically studied for decades, is a young material, firstly isolated in 2004 [48]. It has been known since the 1970s when Eizenberg and Blakely reported single layer graphite growth on various transition-metal substrates [49]. The term graphene was proposed by Boehm et al. in 1986 to describe a single atomic sheet of graphite [50], but at that time it was ruled out the existence of two-dimensional crystals [51], since thermodynamically unstable. In 2004, Novoselov and Geim succeeded in isolating a single flake of graphene by mechanical exfoliation from bulk graphite [52]. Following this discovery, great attention has been devoted to graphene and lots of studies have shown its unique properties, not found in bulk graphite neither in other materials [52, 48, 53].

Nowadays, graphene, considered the "mother" of most carbon allotropic forms (Fig. 2.3), continues to be one of the most theoretically

studied material. Furthermore, thanks to its outstanding properties it has been envisaged as the innovative material, capable to revolutionize the microelectronics field [54, 47].

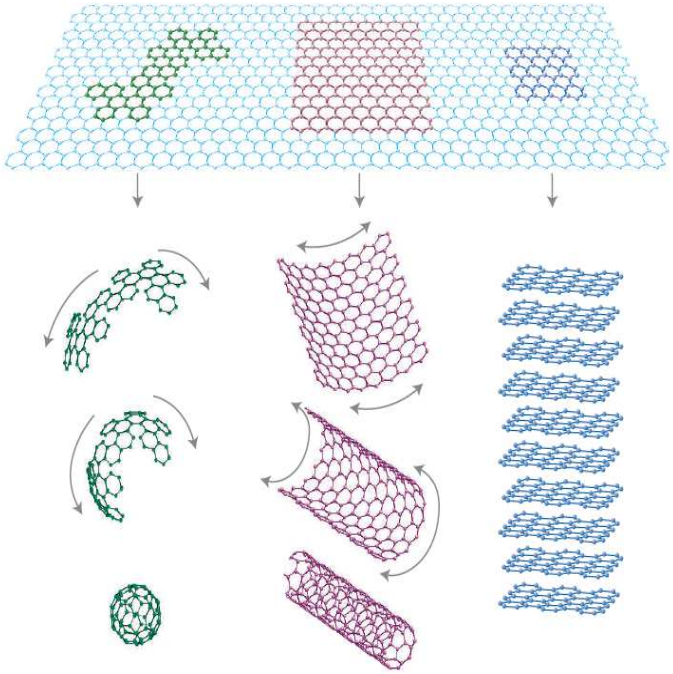

Fig. 2. 3 2D Graphene "mother" of all other carbon dimensionalities. It can be wrapped up into 0D buckyballs, rolled into 1D nanotubes or stacked into 3D graphite [48].

2.2.1 Graphene crystal structure

Graphene is a carbon allotrope in which atoms are arranged forming a honeycomb lattice due to their sp^2 hybridization, with an inter-atomic length of a_{cc}=1.42 Å. The unique electronic properties of graphene are due to this honeycomb lattice arrangement, which can be seen as two non-equivalent interpenetrating hexagonal lattices with a two-atom basis (A and B), as depicted in Fig.2.4.

Both sublattices are Bravais lattices characterized by two base vectors *a* and *b*, with an angle of 120° between them. The lattice vectors forming the basis of the unit cell (Fig. 2.5) are [55]:

$$a_1=\frac{a}{2}\left(3,\sqrt{3}\right) \qquad a_2=\frac{a}{2}\left(3,-\sqrt{3}\right) \tag{2. 1}$$

being the graphene lattice constant $a=|a_1|=|a_2|=a_{cc}\sqrt{3}=0.142\sqrt{3}=0.246$ nm.

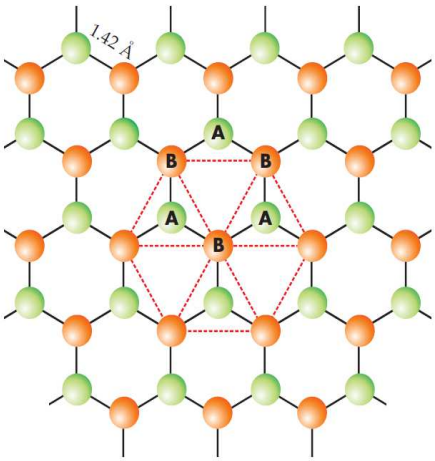

Fig. 2. 4 The honeycomb lattice of graphene showing the two sublattices marked A and B [56].

Any linear combination of the vectors a_1 and a_2 generates all the points in the lattice. The reciprocal lattice vectors can be written as:

$$b_1=\frac{2\pi}{3a}\left(1,\sqrt{3}\right) \qquad b_2=\frac{2\pi}{3a}\left(1,-\sqrt{3}\right) \tag{2. 2}$$

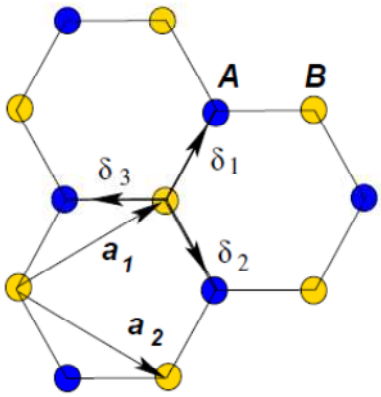

Fig. 2. 5 Lattice structure of graphene showing the two sublattices marked A and B; a_1 and a_2 the lattice unit vectors; δ_i i=1, 2, 3 the nearest neighbor vectors [55].

Considering the reciprocal space of the honeycomb lattice, it is easy to see that the first Brillouin zone is an hexagon [56]. In-plane carbon atoms are bonded to other nearby carbon atoms in *s* configuration and are not available for the conduction process, as well as the electronic bands of the *1s* state, which is completely filled. But, each atom in the unit cell is characterized also by a *p* bond and thus can donate one electron to the lattice, almost completely

delocalized, free to move and actively participate to conduction. This *p* state gives origin to two energy bands, the valence and conduction bands. These bands come in contact, without overlapping, at six points in the reciprocal lattice, which are commonly referred to as the *K* points, coincident with the boundary of the first Brillouin zone. Others important high symmetry points within the first Brillouin zone of graphene are the Γ point at the zone center and the M points in the middle of the hexagonal sides (Fig. 2.6) *K* and *K'* represent a set of nonequivalent points in the reciprocal space which may not be connected one to another by a reciprocal lattice vector.

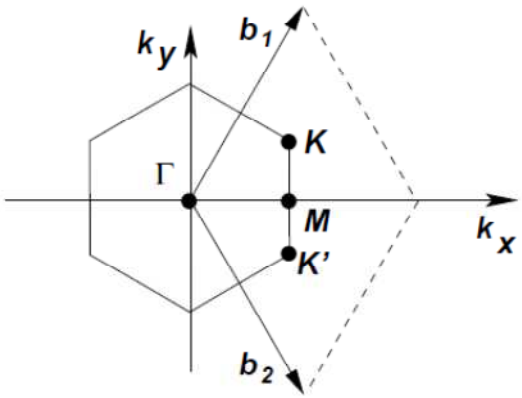

Fig. 2. 6 The first Brillouin zone of graphene marking some of the high symmetry points Γ, M, K and K' [55].

The *K* and *K'* points are the primary points of interest when studying the electronic properties of graphene. This crossing point is called the Dirac point and its energy position is exactly at the Fermi level. A representation of the graphene energy bands is shown in Fig. 2.7. Fermi energy lies exactly at the *K* points for undoped graphene and the Fermi surface of graphene consists thus of only six points. In the vicinity of these points the relationship of the energy versus momentum becomes linear, which has significant consequences for the electronic transport and optical properties of graphene. The linear dispersion region is well-described by the Dirac equation for massless Dirac fermions, particles with relativistic speed and no mass [53]. Thus, the electron transport is governed by Dirac's equation generally expressed as follows:

$$E(k)=\hbar k v_f \qquad (2.3)$$

with $\hbar$ reduced Planck constant, k the wave vector of the electron and v_f=~10 m/s is the Fermi velocity (responsible of the ballistic transport). This is completely different from other crystalline solids where the dispersion relationship *E(k)* is generally a complex curve that can be well approximated, near the bottom of the conduction band, by a parabola:

$$E(k) = \frac{\hbar^2 k^2}{2\, m_{eff}} \tag{2. 4}$$

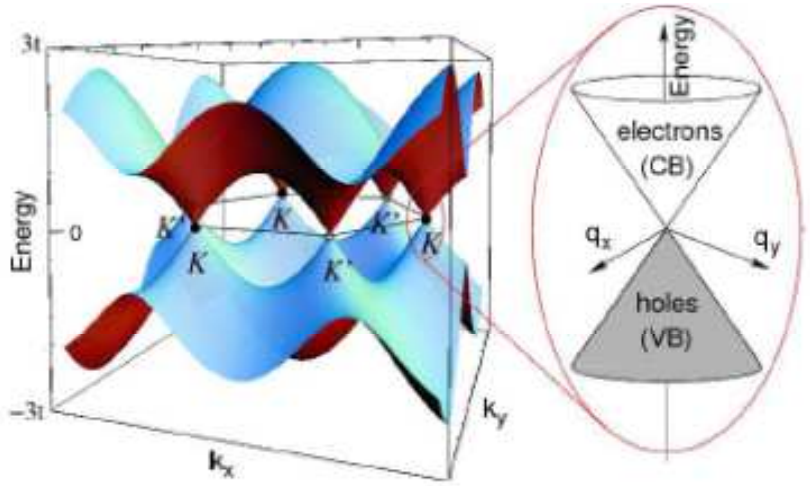

Fig. 2. 7 Band structure of graphene. In the vicinity of the Dirac points at the two nonequivalent corners *K* and *K′* of the hexagonal Brillouin zone, the dispersion relation is linear and hence locally equivalent to a Dirac cone [57].

2.2.2 Properties of graphene

Since graphene discover, its electronic properties have attracted the interest of researchers, who looked at graphene as the substitute of silicon in the fabrication of electronic devices.

The electronic transport and optical properties of graphene are greatly influenced by the Dirac physics of the charge carriers.

In suspended, exfoliated graphene, where interactions with the substrate are eliminated, a mobility value (μ) of about 200000 $cm^2\ V^{-1}\ s^{-1}$ has been observed [54]. This, combined with near-ballistic transport at room

temperature, makes graphene a potential material for nanoelectronics especially in high-frequency applications [58].

An anomalous quantum Hall effect has been reported for graphene. It was observed that, in two-dimensional electron systems subjected to low temperatures and strong magnetic fields, the Hall conductivity σ is shifted of ½ (in units of ge^2/h) with respect to the classical quantum Hall effect [59].

Another effect is the so called Klein tunneling, the peculiar scattering properties of the charge carriers, which for certain incidence angles on electrostatic potential barriers can have a transmission probability of 1 [60].

Graphene shows remarkable optical properties. For instance, despite being only a single atom thick, it can be optically visualized. For freestanding single layer graphene (SLG) transmittance (T) can be derived by applying the Fresnel equations in the thin-film limit for a material with a fixed universal optical conductance [47]:

$$T = (1 + 0.5\,\pi\,\alpha)^{-2} \approx 1 - \pi\,\alpha \approx 97.7\% \qquad (2.\,5)$$

where α is the fine-structure constant [61]. Graphene only reflects <0.1% of the incident light in the visible region, rising to ~2% for ten layers. Thus, it can be assumed the optical absorption of graphene layers to be proportional to the number of layers, each absorbing $A \approx 1 - T \approx \pi\,\alpha \approx 2.3\%$ over the visible spectrum (Fig. 2.8).

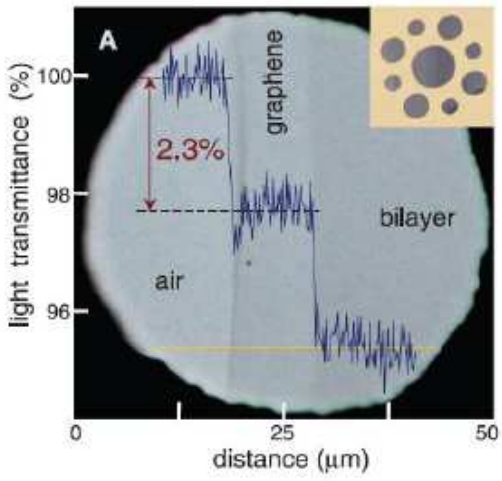

Fig. 2. 8 Scan profile showing the intensity of transmitted white light through air, single layer and bilayer graphene respectively [61].

Its transparency makes graphene ideal for its use in optoelectronic devices such as displays, touchscreen and solar cells, where materials with low sheet resistance R_s and high transparency are needed. Thus, it could replace the current transparent conducting materials, as indium tin oxide (ITO), a doped n-type semiconductor composed of ~90% In_2O_3 and ~10% SnO_2 [62, 47]. ITO is commercially available with T≈80% and R_s as low as 10 Ω/ on glass and ~60−300 Ω/ on polyethylene terephthalate. However, ITO suffers severe limitations: an ever-increasing cost due to indium scarcity, processing requirements, difficulties in patterning and a sensitivity to both acidic and basic environments. Moreover, it is brittle and can easily crack when used in applications involving bending, such as touch screens and flexible displays [47]. For these reasons new transparent conducting materials with improved performance are needed. Nanotubes and graphene show great promise. In particular, graphene films have a higher transmittance over a wider wavelength range than single-walled carbon nanotube (SWNT) films, thin metallic films (ZnO/Ag/ZnO e TiO_2/Ag/TiO_2) and ITO (Fig. 2a) [47].

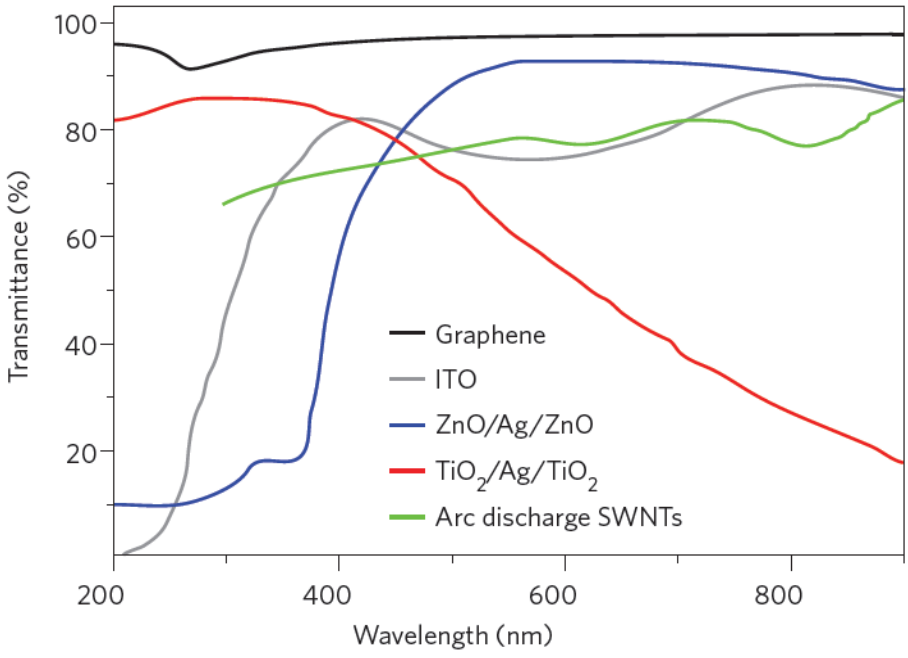

(a)

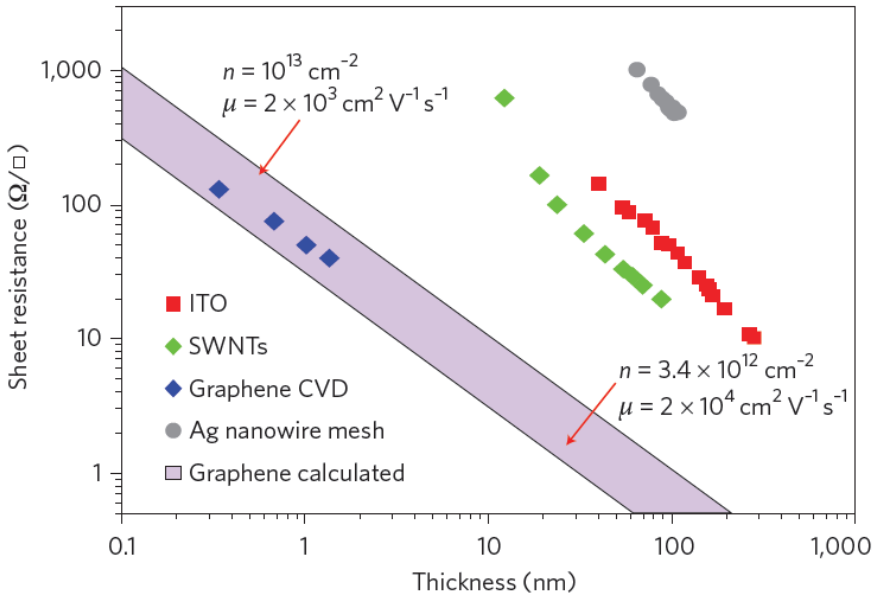

(b)

Fig. 2. 9 (a) Transmittance for different transparent conductors and (b) thickness dependence of the sheet resistance [47].

It has been calculated that for an ideal intrinsic SLG with $T \approx 97.7\%$ resistance sheet value is about 6 kΩ/sq. Thus, an ideal intrinsic SLG would beat the best ITO only in terms of T, not R_s. However, real thin films are never intrinsic. The range of T and R_s that can be realistically achieved for graphene layers of varying thickness can be estimated by taking n= 10^{12}-10^{13} cm^{-2} and μ = 1000 - 20000 $cm^2\ V^{-1}\ s^{-1}$. As shown in Fig. 2.9 b, graphene can achieve the same R_s as ITO, ZnO/Ag/ZnO, TiO_2/Ag/TiO_2 and SWNTs with a similar or even higher transmittance [47].

Besides the aforementioned fascinating electronic features also graphene outstanding mechanical properties have attracted much interest. Indeed, several numerical methods and experimental techniques have proved graphene intrinsic mechanical properties, characterized by high strength, hardness and elasticity [63]. For instance, the value of the Young's modulus equal to 1.0 teraPascal (TPa) was measured for monolayer graphene by Atomic Force Microscopy (AFM), assessing graphene as the strongest material ever measured [63].

Thermal conductivity of graphene at room temperature is among the highest of any known material, about 2000-4000 $Wm^{-1}K^{-1}$ for freely suspended samples. Due to the high thermal conductivity, graphene has been reported as an excellent candidate for thermal management [64].

Finally, graphene has also showed great properties for gas sensing applications. The high theoretical specific surface area (2630 m^2/g) together with the excellent electronic properties, have been exploited in graphene based gas sensors. In fact, being a strictly two-dimensional material its whole volume is exposed to surface adsorbates (Fig. 2.10).

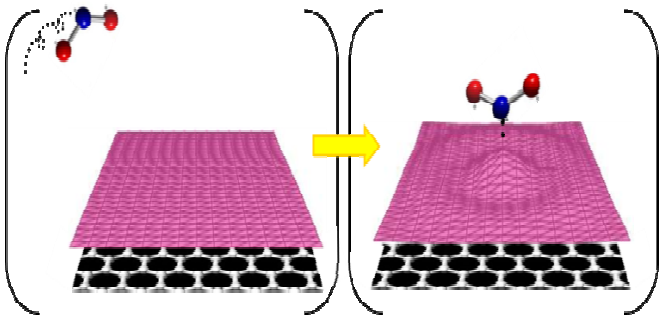

Fig. 2. 10 Schematic interaction between graphene and gas molecules.

Indeed, all the atoms of a single-layer graphene sheet are surface atoms capable of adsorbing gas molecules, providing the largest sensing area per unit volume. The interaction between graphene sheets and adsorbates perturb the electronic system of graphene and due to its high-quality crystal lattice along with its two-dimensional structure, even small amount of extra electrons can cause a noticeable change in its electrical conductivity. Since pristine graphene shows p-type behavior at ambient conditions because of unintentional doping caused by residual species or oxygen molecules in air [65], its interaction with gaseous adsorbates changes upon gas types. The adsorption of electron-withdrawing gas molecules such as NO_2 enhances the doping level of graphene and increases its conductance. Electron-donating molecules such as NH_3 decreases instead its conductance [66]. Due to this outstanding property, Schedin et al. [43] were able to detect individual gas molecules as they got adsorbed onto graphene surface.

2.3 Carbon nanotubes

Carbon nanotubes have been envisaged as the key to potentially revolutionized technology. Due to their fascinating properties, they have focused a lot of attention from the nanomaterial scientific community since their discovery by Sumio Iijima in 1991 [67]. The featuring sizes and structures endow nanotubes with important properties, such as strength, elastic deformability, high stability, high surface area and selectivity. All these remarkable properties make carbon nanotubes ideal for a range of applications, including electronics, material science and biology. What is more, the unique electronic character of nanotubes, together with small dimensions and high surface areas, offer special advantages in using it as advanced miniaturized chemical sensors in a variety of fields.

2.3.1 Carbon nanotubes structure

Carbon nanotubes (CNT) are tubular nanostructures that can be described as made up from a graphene sheet, one atom thick. It is possible to distinguish among single walled (SWNT) and multi walled carbon (MWNT) nanotubes according to the number of graphene sheets. In particular, as the names suggests, a SWNT is made of just one rolled up sheet of graphene, while a MWNT is made of several concentric graphene cylinders wrapped around each other and interacting with van der Waals forces (Fig. 2.11).

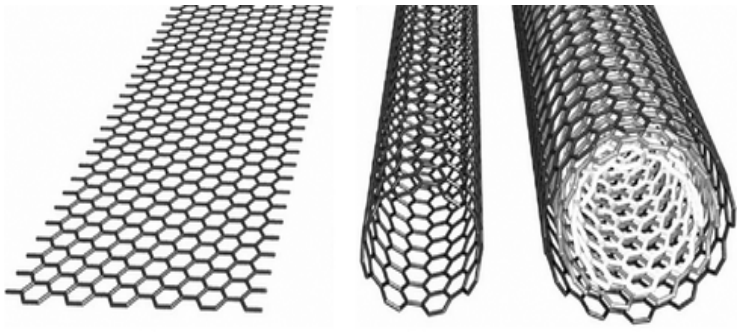

Fig. 2. 11 Graphene sheet, single walled and multi walled carbon nanotubes.

Carbon nanotubes are rolled up along a specific crystallographic direction, identified by the couple of chiral indexes (m,n) of the graphene sheet hexagonal honeycomb lattice. In particular, it is defined a chiral vector

(C_h) which connects two crystallographic equivalent sites on a 2D graphene sheet (Fig. 2.12). It is therefore expressed as a linear combination of the basis vectors a_1 and a_2:

$$C_h = na_1 + ma_2 \quad (2.\ 6)$$

Chiral vector uniquely defines a nanotube since it determines its characteristics, such as the electronic band structure. The direction of this vector is described by the chiral angle θ, formed by the base vector a_1 and the chiral vector itself [68].

$$\theta = \tan^{-1}\left(\frac{\sqrt{3}m}{2n+m}\right) \quad (2.\ 7)$$

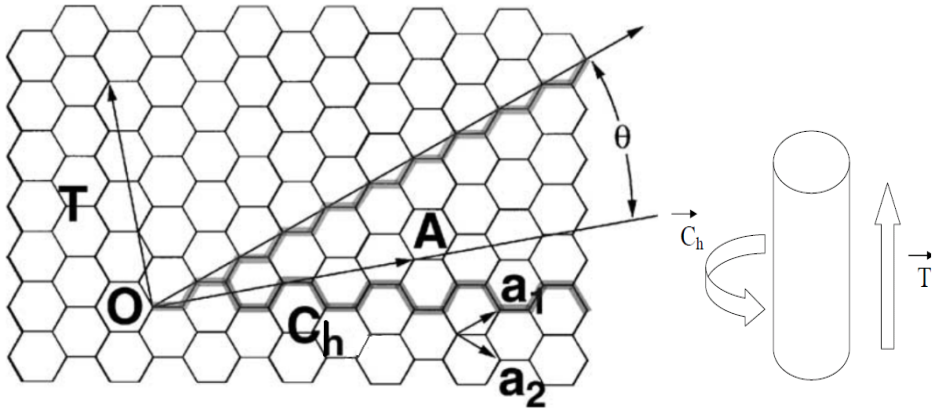

Fig. 2. 12 2D graphene sheet along with the vectors that specify the chirality of nanotubes.

According to the chiral angle and vector values it is possible to distinguish two different types of nanotubes called armchair and zigzag. Generally, when m=0 it is also θ=0°, the nanotubes are zigzag; whereas when n =m thus θ=30°, the nanotubes are armchair. All the other intermediate combination states are called chiral (Fig. 2.13).

The smallest graphene lattice vector T perpendicular to C_h defines the translational period t along the tube axis. It can be also express in terms of the basis vectors a_1 and a_2 as:

$$T = t_1a_1 + t_2a_2 \quad (2.\ 8)$$

where the coefficients t_1 and t_2 are related to (n, m) by

$$t_1 = \frac{2m+n}{d_R} \qquad t_2 = -\frac{2n+m}{d_R} \tag{2. 9}$$

where d_R is the greatest common divisor of (2n + m, 2m + n).

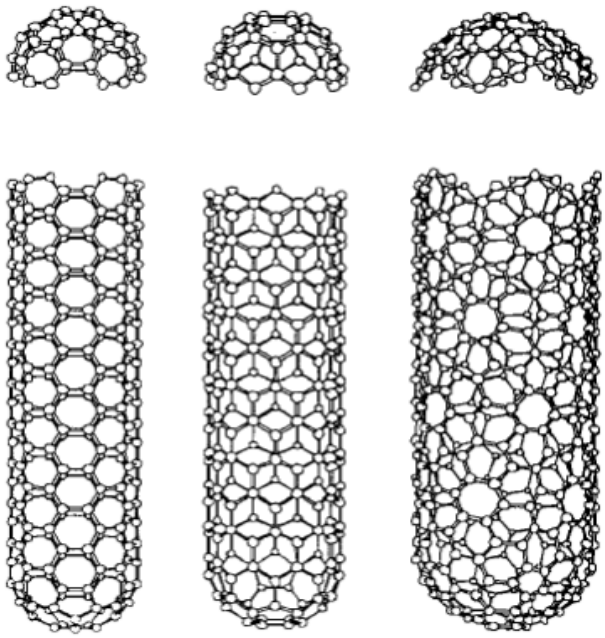

(a) (b) (c)

Fig. 2. 13 Different carbon nanotube configurations: (a) armchair, (b) zig-zag and (c) chiral [68].

Depending on n and m values, carbon nanotubes electronic properties can vary. Featuring parameters of the nanotubes, such as diameter and number of carbon atoms, can be calculated being known the two chiral indexes. It is calculated as:

$$d = \frac{\sqrt{3}\, a_{cc}\sqrt{n^2+m^2+nm}}{\pi} \tag{2. 10}$$

where a_{CC} is the nearest-neighbor C–C distance, assumed 0.142 nm.

The number of carbon atoms in the primitive cell also depends on the integers n and m:

$$N = \frac{4(n^2+nm+m^2)}{d_R} \tag{2. 11}$$

The electronic structure of nanotubes, as well as their physical structure, can be approximated from the rolled-graphene-sheet model. The

lattice vector T and the chiral vector C_h both determine the unit cell of the carbon nanotube in real space. Analogously, the corresponding vectors in reciprocal space are the reciprocal lattice vectors K_1 along the nanotube axis and K_2 perpendicular to the tube axis and therefore parallel in the circumferential direction, which gives the discrete k values in the direction of the chiral vector C_h.

The vectors K_1 and K_2 are obtained from the relation Ri Kj = $2\pi\delta ij$, where Ri and Kj are, respectively, the lattice vectors in real and reciprocal space. Therefore K_1 and K_2 satisfy the relations:

$$C_h K_1=2\pi,\ T K_1 = 0,\ C_h K_2 = 0,\ T K_2 = 2\pi \qquad (2.\ 12)$$

Thus it follows that K_1 and K_2 can be written as:

$$K_1=\frac{1}{N}(-t_2b_1+t_1b_2)\quad K_2=\frac{1}{N}(mb_1-nb_2) \qquad (2.\ 13)$$

where b_1 and b_2 are the reciprocal lattice vectors of a 2D graphene sheet. When the sheet is rolled into a closed cylinder, a periodic boundary condition is imposed along the direction of the chiral vector. Carbon nanotubes diameter is usually in the range of nanometers and their length along the axis is of the order of microns. This results in quasi-one-dimensional electronic states that are quantized along the circumferential direction while remaining unconstrained in the axial direction. Because of the translational symmetry of T, k_2 can therefore assume any value, while k_1 will give discrete k values in the direction of C_h. The quantization of vector k gives rise to discrete numbers of parallel equidistant lines, representing the allowed k modes in the reciprocal space. The distance between two neighboring lines is $K_1=2/d$ that is to say inversely proportional to the nanotube diameter d and with the orientation of the lines given by the chiral angle (Fig. 2.14) [69].

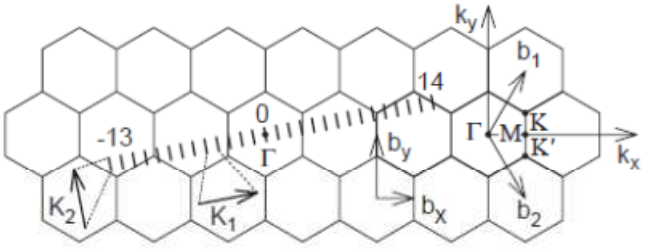

Fig. 2. 14 Parallel equidistant lines represent the allowed k modes in the reciprocal space. The distance between two neighboring lines is $K_1=2/d$ [69].

Thus, the states of the nanotubes are represented in reciprocal space by the intersection of this family of lines and the 2-dimensional graphene Brillouin zone. As a consequence, it is possible to distinguish two different cases for the electronic structure of nanotubes. In fact, the tube will exhibit metallic conduction if a Fermi point is an allowed state of the nanotube, then if the valence and conduction bands will form a transition point. Otherwise, there will be an energy gap between the bands, and the tube will be semiconducting. The energy spacing is directly related to carbon nanotube diameter *D*. In semiconducting tubes, the band gap is given by $E\text{gap}=2\gamma_0 a_{cc}/D$, where γ_0 is a parameter representing the nearest-neighbor overlap integral in a tight-binding scenario [70, 71].

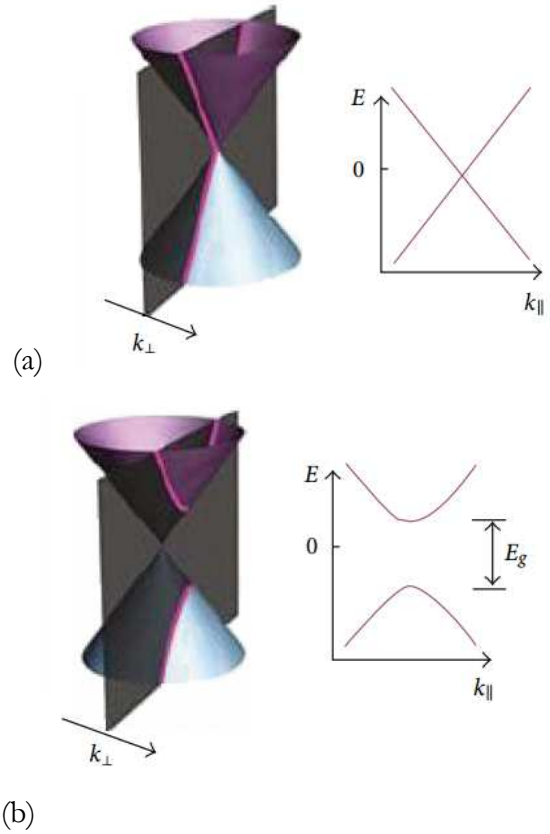

Fig. 2. 15 Sketch of the energy bands in (a) a metallic and (b) a semiconducting single walled carbon nanotube [71].

The type of any nanotube, either metallic or semiconductor, can be obtained by the chiral index (n, m). When the quantity (n - m) is an integer multiple of 3 the tube will be metallic. As a consequence of this condition,

statistically, among all the possible nanotubes 1/3 of all should be metallic and the remaining 2/3 will be semiconducting [69].

The band structure can be further refined by taking into account the curvature of the nanotubes, the cylindrical shape of nanotubes, thus the bending of the sheet has an effect on the electronic structure. This effect is significant in the case of small diameter nanotubes. The carbon lattice curvature gives rise to a small angle between adjacent p orbitals. This results in a shift of the Fermi points able to induce an additional band-gap between valence and conduction bands on the order of few meV in nominally metallic tubes [72]. Anyway, if compared with typical semiconductors band-gaps, this meV effect will be negligible for almost all the practical applications.

2.3.2 Carbon nanotubes properties

Interesting CNT properties can be derived by their structure. Beyond the aforementioned possibility to be more or less conductive, CNT can exhibit superconductivity below 20 K due to the strong in-plane C–C bonds. Moreover, they are known for their high thermal conductivity and excellent mechanical properties. In particular, the elastic modulus is much higher than steel and the Young modulus is in the teraPascal range [73]. Light weight, larger flexibility, high mechanical strength and superior electrical properties make CNTs an interesting material for gas sensing applications. In particular the physical structure endowed them with elevated surface area where gas molecules are likely to be adsorbed. This phenomenon determines a change in CNT electrical properties. Thanks to the ballistic electron transport along the tube axis the altered electrical signal can be transduced to the external contact. In such a way, CNT permit the detection of toxic and harmful gases (such as hydrogen) together with long term performance, conferred by their chemical stability.

Through years, great attention has been devoted to the gas sensing mechanism and many efforts have been done to explain it [74, 75]. The charge transfer between the semiconducting CNT and electron accepting or electron donating gas molecules is well recognized. Even if a lot of attempts have been done to perform excellent CNT gas sensors, many parameters such

as selectivity, low operating temperature, fast reaction and recovery time need to be further improved.

2.4 Synthesis techniques of low dimensional carbon materials

Even if nanostructured carbon materials can be synthesized by numerous synthesis techniques, just few of these are effectively used for the synthesis of graphene and carbon nanotubes. In fact, despite all the interest aroused around these materials, a synthesis method suitable for commercial applications is still lacking. Synthesis methods consist of either top down approaches or bottom up ones. Generally, the top-down method consists of size reduction of larger structures, while the bottom-up approach is the use of atomic precursors as building blocks materials for the construction of new nanostructures.

2.4.1 Graphene synthesis

Mechanical cleavage, thermal decomposition of silicon carbide, liquid phase exfoliation of graphite and chemical vapor deposition are the most commonly used synthesis methods of graphene. Anyway, it should be pointed out that no one of the aforementioned synthesis techniques can be envisaged as the best one in absolute. Since each of these methods is suitable to obtain graphene with different characteristics, the choice of a specific technique should be done only according to the type of application which graphene is addressed to.

2.4.2 Mechanical exfoliation

Mechanical exfoliation can be regarded as the mother of all techniques for graphene production, since it was the first technique through which graphene was successfully synthesized by Geim and Novoselov [52]. It basically consists in the exfoliation of a High Oriented Pyrolitic Graphite block through the so called "scotch-tape technique". The interlayer distance in graphite is 3.34 Å and the layers are stacked together by weak van der

Waals forces. Due to the weak interaction among layers, an adhesive tape can be used to peel off the graphite flakes, as depicted in Fig. 2.16 a. The first piece of tape is repeatedly cleaved by other sticky pieces till to obtain an almost invisible powder on the starting tape. Finally, at the end of the exfoliation process, the tape is transferred onto another substrate that usually is silicon dioxide on Si wafer (SiO_2/Si). In Fig. 2.16 b an optical image of a mechanical exfoliated mutilayer graphene flake is show

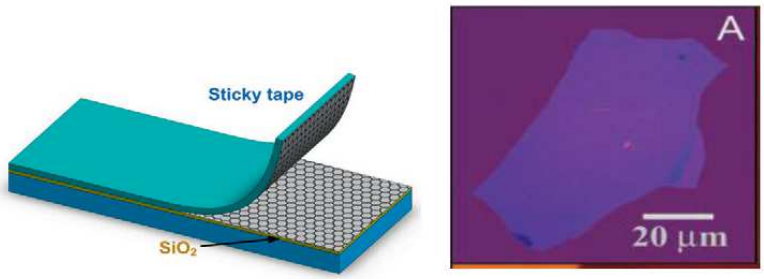

(a) (b)

Fig. 2. 16 (a) Scotch tape mechanical exfoliation [76], (b) image of a mechanical exfoliated mutilayer graphene flake [52].

The costless and advantageous of the technique brought many research groups to use it to produce high quality graphene layers. Anyway in order to be used for the fabrication of nanoelectronic devices, this process needs improvements for both the large-scale production and transfer method.

2.4.3 Epitaxial growth

Graphene can be synthesized by the thermal decomposition of silicon carbide [76, 77] (Fig. 2.17). This growth technique is usually referred to as "epitaxial growth" even though there is a very large lattice mismatch between SiC (3.073 Å) and graphene (2.46 Å) and the carbon rearranges itself in a hexagonal structure as Si evaporates from the SiC substrate, rather than being deposited on the SiC surface, as would happen in a traditional epitaxial growth process.

The procedure for the silicon carbide thermal decomposition is theoretically simply. Both surfaces (Si(0001)- and C(000-1)-terminated) are annealed at high temperature under ultra-high vacuum (UHV). The annealing of the substrates results in the sublimation of the silicon atoms while the

carbon-enriched surface undergoes reorganization and, for high enough temperatures, graphitization [76]. The typical range of annealing temperatures goes from 1500°C to 2000°C and the usual heating and cooling rates are 2-3°C/sec [78]. The thermal decomposition, however, is not a self-limiting process and areas of different film thicknesses may exist on the same SiC crystal. Graphene obtained on SiC single crystals has good properties, but this material may be limited to devices on SiC only, since transfer to other substrates such as SiO_2/Si might be difficult, with all the drawbacks involved in the transfer process. Moreover, it is an expensive technique because of the SiC wafers cost.

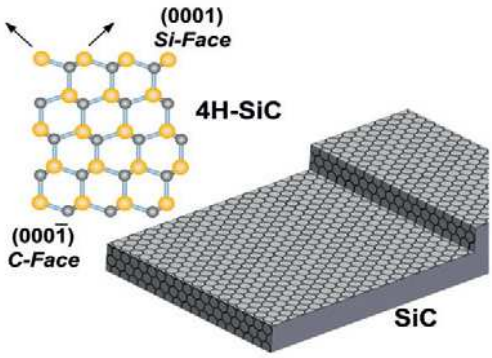

Fig. 2. 17 Growth on SiC. Gold and grey spheres represent Si and C atoms, respectively [76].

2.4.4 Liquid-phase exfoliation

Graphite can be exfoliated in liquid environments exploiting ultrasounds to extract individual layers, (Fig. 2.18). The liquid-phase exfoliation (LPE) process generally involves the dispersion of graphite in special solvents able to minimize the interfacial tension between the liquid and graphene flakes. Indeed, if the interfacial tension is high, the flakes tend to adhere to each other and the work of cohesion between them is high, hindering their dispersion in liquid. Liquids with surface tension $\gamma \sim 40$ mN/m, are the best solvents for the dispersion of graphene and graphitic flakes, since they minimize the interfacial tension between solvent and graphene [76]. The solvents that mainly match this requirement are N-methyl-pyrrolidone (NMP) and Dimethylformamide (DMF) even if toxic and harmful to the environment.

In order to favor the splitting of graphite into individual platelets, the solution should be sonicated for a long time. Finally the surnatant phase of the suspension, the thinner exfoliated flakes, must be separated from the unexfoliated ones. Centrifugation process is generally used to this purpose [79].

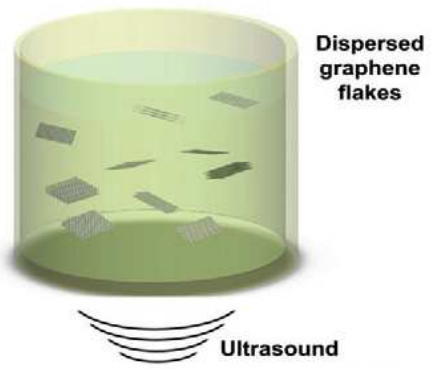

Fig. 2. 18 Liquid phase exfoliation technique [76].

Since this technique is regarded as one of the most promising for mass production, high concentration of exfoliated graphene is desirable. It is important to note that the yield of the process is strongly affected by each parameter involved in the procedure.

2.4.5 Chemical Vapor Deposition

Chemical Vapor Deposition (CVD) is a widely used process to grow thin films from many different carbon precursors both in vapor and liquid phase, such as methane and ethanol [80, 81, 82, 83].

The precursor is dissociated at high temperature using transition metal substrates such as Ni and Cu. Because of cost, grain size, etchability, and their wide use and acceptance by the semiconductor industry, Ni and Cu have received the most attention as graphene substrates [84]. Indeed, graphene and few-layer graphene have been grown on polycrystalline Ni [85] while large area graphene has been grown on Cu substrates [83]. Two different CVD mechanism growth have been proposed on account of the different substrates [84].

Graphene on Ni is due to a C precipitation process. The solubility of carbon in Ni is high, thus carbon diffuses into the metal first before

segregating and precipitating to the surface. A fast cooling rate is needed to suppress the formation of multiple layers (Fig. 2.19 a). Indeed, nonuniform layers are obtained with a variation in thickness from a monolayer to many layers over the metal surface.

On the other hand, when Cu substrates are used a surface adsorption mechanism is involved. Cu is one of the most used catalyst due to the low solubility of carbon in it even at a very high temperature. During growth C atoms nucleate on the substrate surface and then nuclei grow to form domains. Large-area graphene films with uniform thickness, due to the low solubility of C in Cu, are obtained. In this case graphene growth is surface mediated and self-limiting (Fig. 2.19 b).

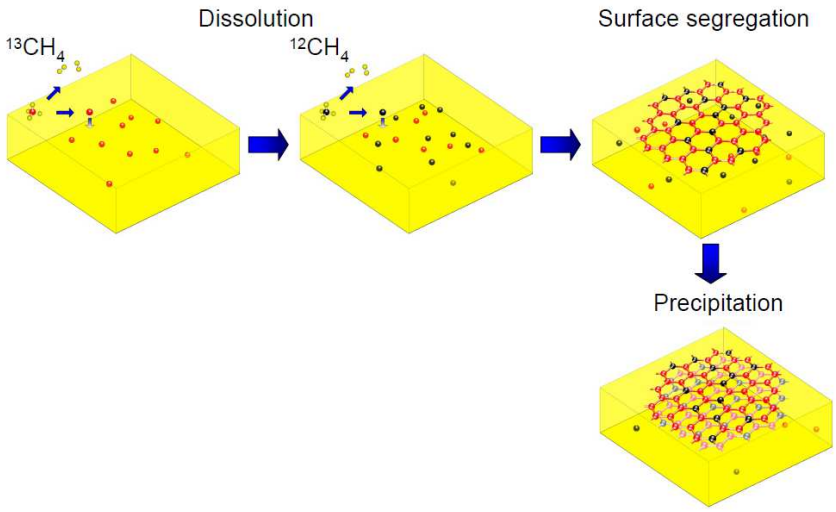

(a)

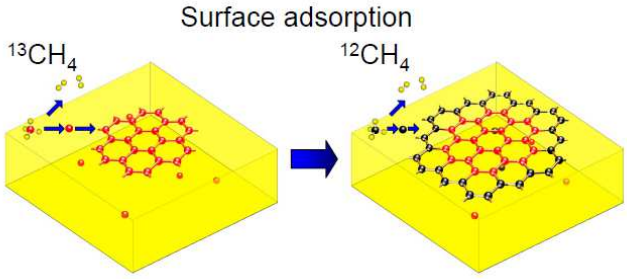

(b)

Fig. 2. 19 Schematic representation of graphene mechanism growth (a) precipitation over Ni substrate and (b) adsorption over Cu substrate. The growth mechanisms have been studied by the use of two different carbon isotopes ^{12}C ^{13}C [84].

Basically, the CVD process relies on carbon saturation of a transition metal during the exposure to a hydrocarbon source at high temperature. The catalyst substrate is put into a chamber where, under a continuous flow of carrier gases, the sample is gradually heated till the growth temperature reaches approximately 1000 °C according to the substrate type. Due to the high temperature, the carbon atoms decompose from hydrocarbons and nucleate on the catalyst substrate. The rapid cooling of the substrate in inert atmosphere down to room temperature, is critical in suppressing formation of multiple layers (Fig. 2.20 a) [86].

It is fundamental to control the synthetic graphene by its parameters, for examples catalysts, temperature, gas composition, gas flow rate, deposition time as well as heating and cooling rate. Time dependence of experimental parameters is reported in Fig. 2.20 b.

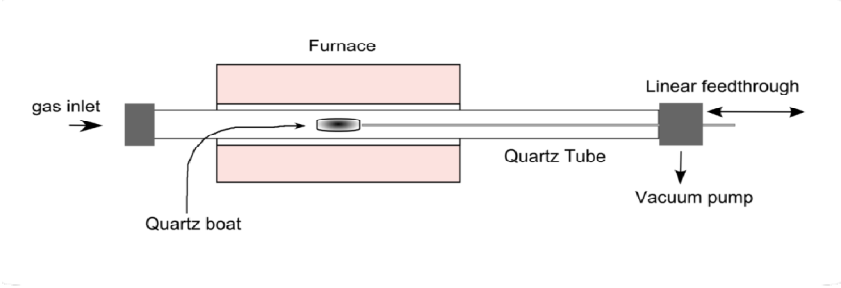

(a)

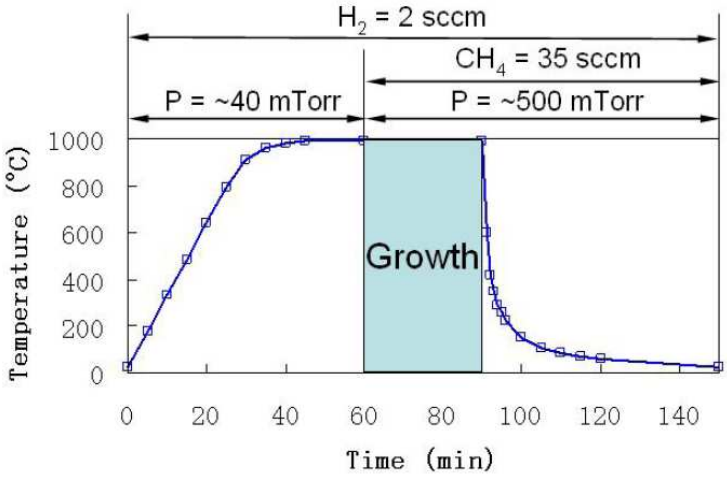

(b)

Fig. 2. 20 Sketch of CVD system. (b) Time dependence of experimental parameters: temperature, pressure and composition/flow rate for graphene growth by methane (CH_4) in hydrogen (H_2) flow [83].

Compared to other graphene synthesis processes, as previously reported, CVD growth on metal substrates has the distinct advantage of being able to provide very large-area graphene films of good crystalline quality and more easily transferrable to other substrates.

2.4.6 Transfer methods

The transfer of CVD graphene is a crucial process which can affect the quality of the transferred films and compromise their application in devices. Indeed, the removal and transfer process from the growth substrate to a more useful one is a critical step since it can provoke damages or cracks, resulting in discontinuous graphene films.

Several transfer processes have been developed and can be mainly classified as wet, when graphene is in contact with a liquid, or dry, when one face of graphene is protected from contacting any liquid, while the other is typically in contact with a polymer, eventually removed by solvents.

The standard established transfer procedure for CVD graphene grown on copper foil is based on a protective layer of Poly-methyl methacrylate (PMMA), typically used in the silicon industry.

Basically, a thin layer of PMMA is spin-coated on the graphene/copper substrate, then chemical etching of the copper substrate is performed. Graphene film is transferred to a clean bath of deionized water for rinsing and finally transferred to the substrate of interest (e.g., SiO_2/Si wafer). In order to remove PMMA, wash-off in acetone and thermal treatment is always performed. A sketch of the process is reported in Fig. 2.21.

Even if it has been recognized as the better transfer technique, this process is still far from ideal. In fact, despite PMMA removal, some residues were observed to remain adsorbed on graphene inducing defects and affecting its electronic properties [87].

Recently, a very efficient transfer method has been reported [88], based on the use of Cyclododecane ($C_{12}H_{24}$), a non-toxic and eco-friendly organic compound. Cyclododecane can be spin coated on graphene, and after assisting the wet etching of the copper catalyst, it completely sublimates at ambient conditions providing a clean means of transferring atomic-thick

films, without introducing unwanted contaminants and thus not requiring any further restoring process [88]. Thus, it can be considered an eco-friendly process since it does not require the use of solvents for its removal and it can be in principle recovered after the process. The transfer method results simple, effective and capable of maintaining intact the intrinsic features of graphene films, in terms of both properties and defects. The well-established method is currently used in place of the standard reported ones [82].

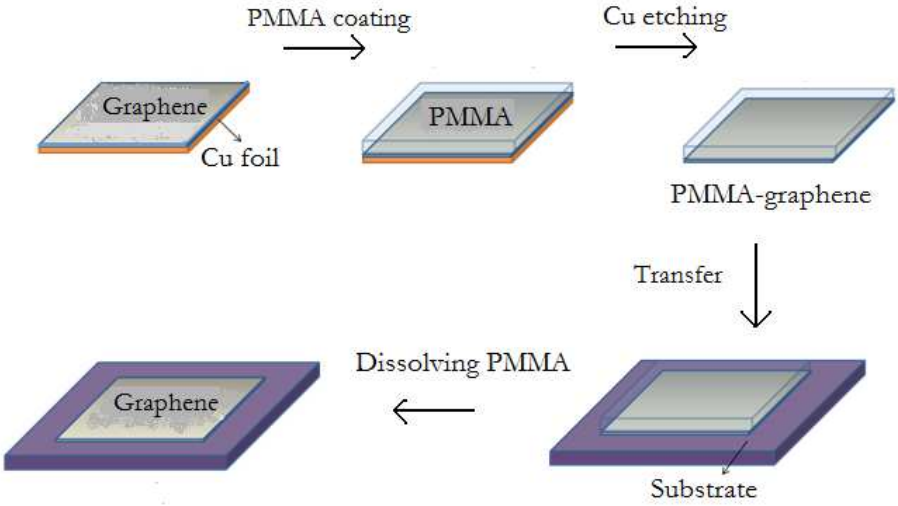

Fig. 2. 21 Sketch of the PMMA transfer method for CVD graphene.

2.4.7 Carbon nanotube synthesis

As regards carbon nanotubes synthesis, the three main techniques able to produce high quality CNT are: electric arc discharge, laser ablation and chemical vapor deposition.

Laser ablation and arc-discharge are modified physical vapor deposition techniques and involve the condensation of hot gaseous carbon atoms generated from the evaporation of solid carbon. Arc discharge belongs to the methods that use higher temperatures (above 1700 °C) for CNT synthesis which usually causes the growth of CNT with fewer structural defects in comparison with other techniques.

Laser ablation is one of the best methods to grow CNT with high-quality and high-purity. In this method the principles and mechanisms are similar to the arc discharge with the difference that the energy is provided by a laser hitting a graphite pellet containing catalyst materials.

In arc-discharge and laser ablation methods, although high quality materials can be produced, the high temperatures employed for evaporating carbon atoms from solid carbon sources (over 3000 K) make them difficult to scale up in a cost efficient way, besides being accompanied by other forms of carbon difficult and expensive to eliminate.

In that sense, much attention is given to the chemical vapor deposition (CVD) of hydrocarbons over metal catalysts. CVD has been extensively used in the past to produce different forms of carbon filaments and fibers and is being applied for the production of both single and multi-walled carbon nanotubes in the gram scale and at low cost [89].

It is based on the same technique used for graphene growth. Obviously, the operating conditions are slight different, especially in terms of growth time, longer in this case, of catalysts, also in powder form, and cooling time, not so restricted as in graphene case.

Anyway, as well as for graphene, the growth mechanism of the CVD process needs to be optimized. The main reason lies in the fact that many different variables of the synthesis process (like metal catalyst, catalyst support, flow rates, hydrocarbon source and concentration, temperature and time, among others) can have great influence on the final product.

2.5 Characterization techniques of low dimensional carbon materials

Several techniques are usually employed for carbon-based materials characterization. Among these, the most commonly used is Raman spectroscopy. It is the principal tool used to investigate the vibrational dynamics of carbon materials and to provide structural characterization. It is recognized to be unambiguously able to provide the fingerprint of the carbon materials as well as that of all the other Raman active materials.

Other supporting characterizations, that will be discussed in the following, are the electron microscopy techniques such as Scanning Electron Microscopy (SEM) and Transmission Electron Microscopy (TEM), based on the use of electron beams to examine samples, and X-ray diffraction (XRD).

SEM and TEM, working in scanning or transmission conditions, can be considered complementary techniques. In such a way, different information on sample morphology can be extrapolated. Moreover different magnification ranges are also covered. XRD is instead able to provide phase identification of crystalline solids.

2.5.1 Raman spectroscopy

The Raman phenomenon was detected in 1928 by the Indian physicists Raman and Krishnan [90]. The basics of the Raman scattering can be explained using classical and quantum mechanical theories. Both formulations are based on the idea that the origin of scattered radiation is considered to be the oscillating electric dipole moments induced in a molecule by the electromagnetic fields of the incident light waves [91].

In the classical approach, the incoming electromagnetic radiation can be described by a sinusoidal plane electromagnetic wave. The oscillating electric field (Eq. 2.14) induces in a molecule a dipole moment (Eq. 2.15):

$$E = E_0 \cos 2\pi\, \nu_0 t \tag{2. 14}$$

$$p = \alpha E = \alpha\, E_0 \cos 2\pi\, \nu_0 t \tag{2. 15}$$

where ν_0 is the oscillation frequency of the electric field and α is the polarizability of the molecule. The polarizability of a vibrating molecule is not a constant since it depends upon the molecular conformation which changes with the displacements of the nuclei during the vibrations. Let $q(t) = q_o \cos(2\pi\nu_{vibr} t)$ be the variation of the nuclear distance during a vibration at frequency ν_{vibr} , q_0 being the maximum variation.

Although the variation law of α(t) is not known, it can be approximated at the first order as:

$$\alpha = \alpha_0 + \left(\frac{\partial \alpha}{\partial q}\right)_0 q + \cdots \tag{2. 16}$$

where α_0 is the polarizability of the molecule in the equilibrium geometry and the second term represents the polarizability change due to the molecular vibration.

The classical theory of electromagnetism states that an electric dipole oscillating at frequency ν emits e.m. radiation at the same frequency and with an intensity given by:

$$I = \frac{16\pi^4 \nu^4}{3c^2} |p|^2 \tag{2. 17}$$

thus, for $\nu = \nu_0$

$$I = \frac{16\pi^4 \nu_o^4}{3c^2} \alpha^2 E_o^2 \cos^2(2\pi\nu_o t) \tag{2. 18}$$

By considering the change of α due to a molecular vibration, it is possible to obtain the expression of the oscillating dipole (Eq. 2.19) and the emitted intensity (Eq. 2.20):

$$\begin{aligned} p(t) = {} & \alpha_o E_o \cos(2\pi\nu_o t) + \\ & + \left(\frac{\partial\alpha}{\partial q}\right)_o \frac{q_o E_o}{2} \cos[2\pi(\nu_o + \nu_{vib})t + \varphi] + \\ & + \left(\frac{\partial\alpha}{\partial q}\right)_o \frac{q_o E_o}{2} \cos[2\pi(\nu_o - \nu_{vib})t - \varphi] \end{aligned} \tag{2. 19}$$

$$\begin{aligned} I = {} & \frac{16\pi^4}{3c^2} E_o^2 \left\{ \nu_o^4 \alpha_o^2 \cos^2(2\pi\nu_o t) + \right. \\ & + (\nu_o + \nu_{vib})^4 \cdot \left[\left(\frac{\partial\alpha}{\partial q}\right)_o \frac{q_o}{2} \right]^2 \cdot \cos^2[2\pi(\nu_o + \nu_{vib})t + \varphi] + \\ & \left. + (\nu_o - \nu_{vib})^4 \cdot \left[\left(\frac{\partial\alpha}{\partial q}\right)_o \frac{q_o}{2} \right]^2 \cdot \cos^2[2\pi(\nu_o - \nu_{vib})t - \varphi] \right\} + \\ & + cross - terms \end{aligned} \tag{2. 20}$$

An oscillating dipole moment emits therefore with the frequency of the incident field (Rayleigh scattering) and in phase with it. In addition, the molecule radiates with two frequencies that are modulated by the frequency of the excited normal vibration and phase shifted (Raman scattering). The Raman scattered light has a lower frequency than the incident light (Stokes-

Raman scattering) or a higher frequency (anti-Stokes Raman scattering) and are in both case incoherent because of the phase factor [91].

In the spectrum of the scattered radiation, the new frequencies are termed Raman lines, or bands, and are said to constitute a Raman spectrum, as depicted in Fig. 2.22, where the typical recorded Raman spectrum of carbon tetrachloride (CCl_4) is reported.

The patterns of bands observed in the spectra are entirely consistent with the classical theory. The spectra also show that Rayleigh scattering is much more intense than Raman scattering, and that Stokes Raman scattering is more intense than anti-Stokes Raman scattering with the ratio of the intensity of anti-Stokes to Stokes Raman scattering dependent on ν_{vib} .

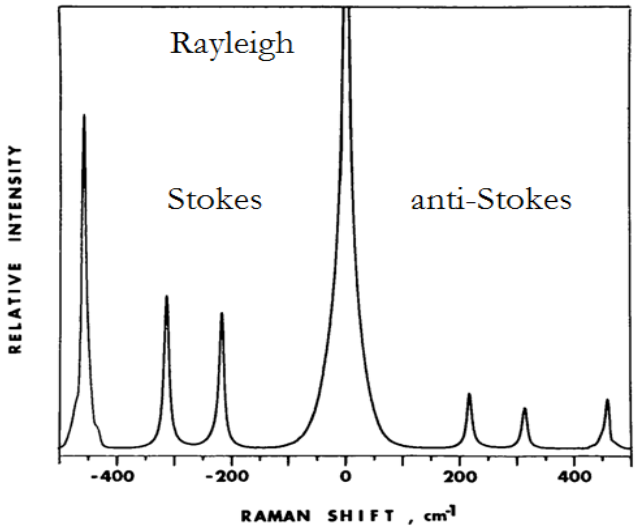

Fig. 2. 22 Raman spectrum of carbon tetrachloride showing Rayleigh, Stokes and anti-Stokes Raman bands.

One of the failures of the classical theory is that the ratio of the Stokes and anti-Stokes intensities should theoretically be <1:

$$\frac{I_{Stokes}}{I_{anti-Stokes}} = \left(\frac{\nu_0 - \nu_{vib}}{\nu_0 + \nu_{vib}} \right)^4 \qquad (2.\ 21)$$

Actually, as experimentally shown it is not correct since Stokes Raman scattering is more intense than the anti-Stokes Raman scattering. The quantum theory of the Raman scattering overcomes this problem.

The inelastic scattering (Raman scattering) of monochromatic light generated from a laser source, usually in the visible range, is considered.

When the photons of laser light interacts with the molecules of a sample, different types of energy exchange can happen. If the collisions are perfectly elastic, the scattered light will have the same frequency of the incident radiation, the so-called Rayleigh scattering. If the collision is inelastic, molecules will gain or lose amounts of energy, thus frequencies below or above that of the incident laser beam will be detected. Radiation scattered at higher frequency is referred to as 'anti-Stokes' radiation, while at lower frequency is known as 'Stokes' [92]. If the scattered photon has less energy than the incident photon, then the molecule is excited to a higher-energy level (Fig. 2.23). This corresponds to the Stokes process and typically corresponds to the excitation of the molecule from the vibrational ground state to the first excited state. If, on the contrary, the scattered photon has more energy than the incident photon, then the molecule has relaxed from an excited vibrational state to its ground state. This corresponds to the anti-Stokes process. In order for an anti-Stokes process to take place, the system must be in an excited vibrational state in the first place. In typical conditions, this may only occur through thermal excitation and this implies that the anti-Stokes signal depends at equilibrium on temperature.

In the quantum mechanical model the intensity depends on the occupation of the initial state. This is determined by the Boltzmann distribution. Thus the intensity ratio is dependent on temperature T as:

$$\frac{I_{anti-Stokes}}{I_{Stokes}} = \frac{(\nu_o + \nu_{vib})^4}{(\nu_o - \nu_{vib})^4}\frac{N'}{N} = \frac{(\nu_o + \nu_{vib})^4}{(\nu_o - \nu_{vib})^4}\exp\left[-\frac{\Delta E}{kT}\right] \qquad (2.\ 22)$$

where N and N' are the number of molecules in the ground and excited states.

Usually Raman measurements are performed considering only Stokes lines. In fact, since the anti-Stokes lines are due to the scattering from molecules in excited states, the intensity of the anti-Stokes lines is considerably lower than Stokes lines due to scattering from molecules in the ground state, simply because of the lower population of the excited states with respect to ground state, according to the Boltzmann statistics.

The vibrational frequency depends on the binding strength and is a characteristics of the molecule. Thus the shift in frequency of the scattered light from a given material is unique and gives information about the vibrational modes of the molecules, resulting in an unambiguous identification of the sample.

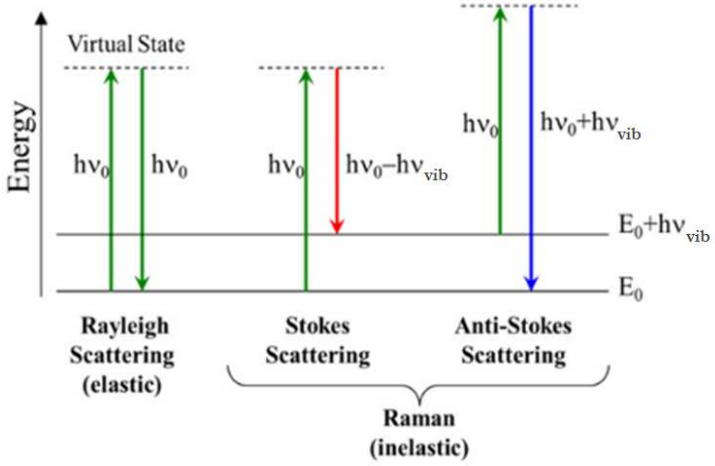

Fig. 2. 23 Schematic representation of quantum energy transitions for Rayleigh and Raman scattering.

Typical experiment consists in a sample being illuminated with a laser beam. Back-scattered radiation is collected with an objective lens and sent through a monochromator. The wavelength corresponding to the Rayleigh scattering is filtered out, while the remaining light is dispersed onto a diffraction grating. The intensity of the shifted light versus frequency results in a Raman spectrum of the sample. Generally, Raman band positions will lie at the frequencies corresponding to the energy levels of the vibrations of different functional groups. Rayleigh band lies at 0 cm^{-1}.

The interpretation of the Raman spectra of carbonaceous materials has been widely discussed in the literature with studies covering a wide range of carbon structures [93, 94, 95]. As for the interpretation of the Raman spectra, an understanding of the phonon dispersion is essential. Therefore, by considering the interaction of the lattice vibrations with the electromagnetic radiation, we can gain insight into the Raman spectra of the crystals [96, 97]. Considering a diatomic linear lattice as shown in Fig. 2.24, the mass of the atoms are taken as M_1 and M_2 , respectively. The lattice spacing is 2a.

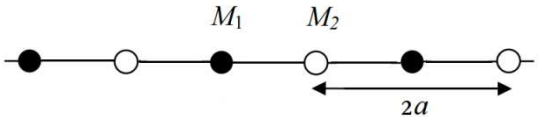

Fig. 2. 24 Diatomic linear lattice with M_1 and M_2 atoms mass and lattice spacing 2a.

If it is assumed nearest neighbor interaction only, by imposing the periodic boundary conditions, the solutions of motion equations are:

$$\Omega^2 = C\left[\left(\frac{1}{M_1}+\frac{1}{M_2}\right) \pm \sqrt{\left(\frac{1}{M_1}+\frac{1}{M_2}\right)^2 - \frac{4\sin^2 Ka}{M_1 M_2}}\right] \quad (2.\ 23)$$

with C the force constant between adjacent atoms. The equation gives the relationship between Ω and k, called the dispersion relation $\Omega = \Omega(k)$. For each wave vector k two Ω values are obtained (Fig. 2.25). The solution corresponding to the plus sign is called the optical branch. It can be shown that for transverse displacements of the particles at k= 0, the two atoms vibrate against each other with a fixed center of mass. This shows that the two atoms of masses M_1 and M_2 move in the opposite directions. If these atoms carried charges of opposite sign, this type of vibration could be excited by an optical field and hence the name optical branch. The solution corresponding to the minus sign is called the acoustical branch and has the characteristic of being linearly proportional to k for small k values [96]. In general, electromagnetic waves propagating within the crystal will interact only with lattice vibrations of the same wavelength and frequency.

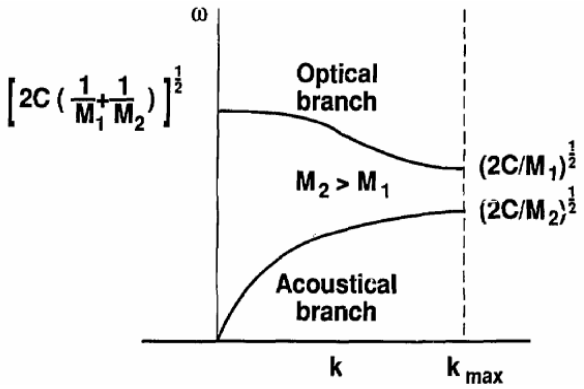

Fig. 2. 25 Dispersion curve in biatomic crystal. Optical and acoustical branches are shown.

The above discussion can be extended to the case of more than two atoms per unit cell. For p atoms in the primitive cell there will be 3p equations of motion. Three equations will correspond to the acoustical modes. The remaining 3(p - 1) modes will each have a nonzero frequency in the long wavelength limit and are the optical modes [96].

Since the unit cell of monolayer graphene contains two carbon atoms, A and B, there are six phonon dispersion bands, in which three are acoustic branches (A) and the other three are optic (O) phonon branches [95] (Fig. 2.26). Specifically, for one acoustic branch (A) and one optic (O) phonon branch, the atomic vibrations are perpendicular to the graphene plane, and they correspond to the out-of plane (o) phonon modes. For two acoustic and two optic phonon branches, the vibrations are in-plane (i) [95]. Generally, the phonon modes are classified as longitudinal (L) or transverse (T) according to vibrations parallel with the A-B carbon-carbon directions or perpendicular to it. Therefore, as shown in Fig. 2.26, along the high symmetry ΓM and ΓK directions, the six phonon dispersion curves are assigned to LO, iTO, oTO, LA, iTA, and oTA phonon modes [95].

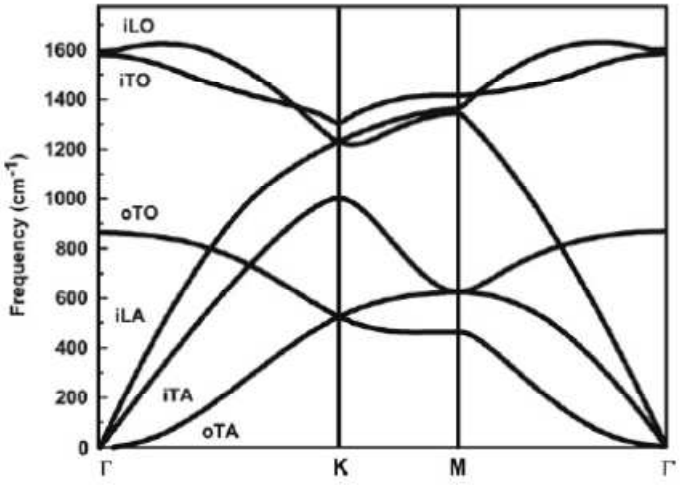

Fig. 2. 26 phonon dispersion relation of graphene showing the iLO, iTO, oTO, iLA, iTA and oTA phonon branches [95].

In the inelastic scattering of light in a crystal, an incident photon of wave vector k_i and frequency ω_i is widespread in the direction determined by the wave vector k_s. The frequency of the scattered photon changes to a new value ω_s, as a phonon lattice (wave vector q_j and frequency Ω_j) is created or

destroyed. The conservation conditions for Raman scattering are the energy (Eq. 2.24) and momentum conservation (Eq. 2.25):

$$\hbar\omega_i = \hbar\omega_s \pm \hbar\Omega_j \tag{2. 24}$$

$$\hbar k_i = \hbar k_s \pm \hbar q_j \tag{2. 25}$$

The number of emitted phonons before relaxation of the lattice can be one, two, and so on, respectively, one-phonon, two-phonon and multi-phonon Raman processes. The order of a scattering event is defined as its number in the sequence of the total scattering events, including elastic scattering by an imperfection (such as a defect or edge) of the crystal. The lowest order process is the first-order Raman scattering process which gives Raman spectra involving one-phonon emission [69].

The most prominent features in the Raman spectra of graphene are the G peak appearing at 1582 cm^{-1} and the 2D peak at about 2700 cm^{-1}. In the case of disordered samples, or at the sample edges, the disorder-induced D-peak is also detected around 1350 cm^{-1}.

The activation mechanism of the peaks is schematically shown in Fig. 2.27.

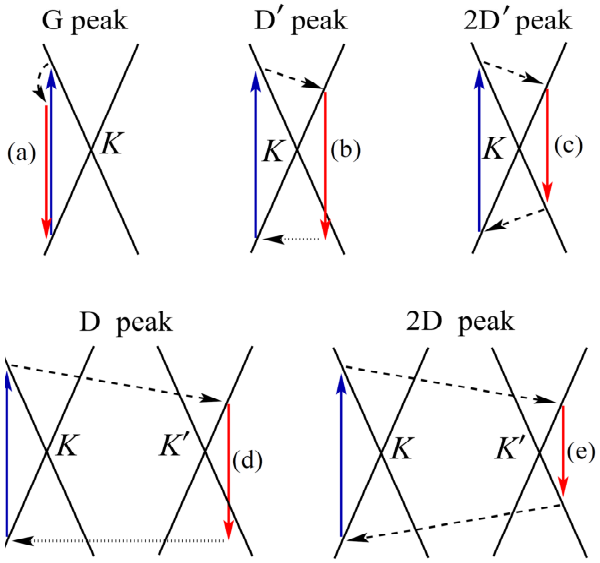

Fig. 2. 27 Role of the electron dispersion (Dirac cones, shown by solid black lines) in Raman scattering: (a) intravalley one-phonon G peak, (b) defect-assisted intravalley one-phonon D peak, (c) intravalley two-phonon 2D peak, (d) defect assisted intervalley one-phonon D' peak, (e) intervalley two-phonon 2D' peak. Vertical solid arrows represent interband transitions accompanied by photon absorption (upward arrows) or emission (downward arrows) [98].

In detail, the G peak is associated with the doubly degenerate (iTO and LO) phonon mode (E_{2g} symmetry, due to the bond stretching of all pairs of sp^2 atoms in both rings and chains, Fig. 2.28) at the Brillouin zone center. In fact, the G-band is the only band coming from a normal first order Raman scattering process in graphene [95, 99].

D peak is due to the A_{1g} breathing mode of six-atom rings (Fig. 2.28) and is not Raman active for pristine graphene, but can be activated when symmetry is broken by structural disorder, as edges or defects. It originates from a second order process involving one iTO phonons and one defect around *K* [95]. The two scattering processes consist of one elastic scattering event by defects of the crystal and one inelastic scattering event by emitting or absorbing a phonon.

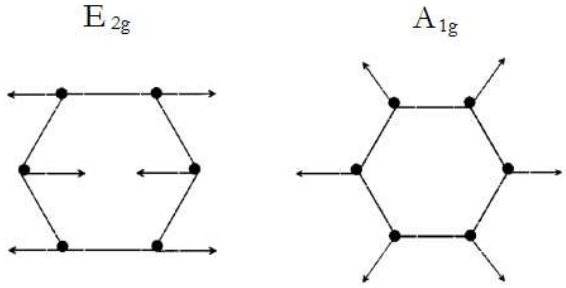

Fig. 2. 28 Carbon motions in the G modes namely E_{2g} and D modes namely A_{1g} [93].

The 2D peak, approximately twice of the D band frequency, originates from a second-order process too, involving two iTO phonons near the *K* point [95]. The two involved phonons give rise to inelastic scattering events. This double resonance mechanism is an inter-valley process that connects points in circles around nonequivalent *K* and *K'* points in the first Brillouin zone of graphene.

A weaker feature can be also detected, namely D', centered roughly at 1620 cm^{-1}. The double resonance process responsible for the D' band is an intra-valley process, since it connects two points belonging to the same circle around the *K* or *K'* point. Finally, 2D' peak is the second order of D' peak.

The typical graphene Raman spectrum is shown in Fig. 2.29.

The D to G relative intensity (I_D/I_G) commonly monitors the density of lattice defects in nanocarbons. Information about the number of graphene

layers (nGL) can be deduced from shape and relative intensity of the 2D-peak (Fig. 2.30) [95]. In graphene produced by micro-mechanical cleavage of bulk graphite, a single Lorentzian component well reproduces the 2D peak of single-layer (1L) graphene, whereas four Lorentzian components are needed in case of bi-layer (2L) graphene. Raman spectrum of multi-layer graphene (nGL > 5) is hardly distinguishable from that of bulk graphite [95].

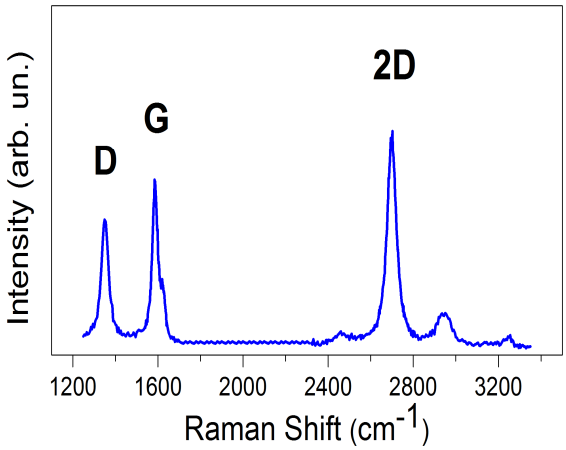

Fig. 2. 29 Typical Raman spectrum of graphene showing the main Raman features, the D, G and 2D bands.

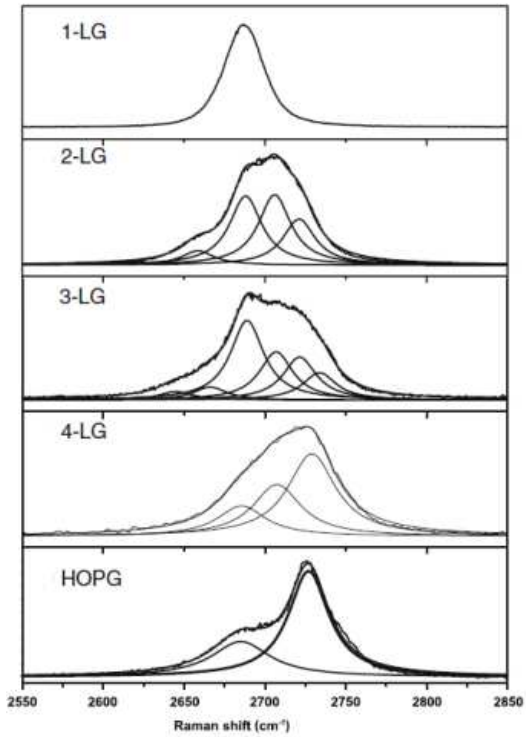

Fig. 2. 30 Evolution of 2D Raman band with the number of graphene layers: 1-LG, 2-LG, 3-LG, 4-LG and HOPG [95].

In CVD graphene, the shape difference of the 2D-peak for one or more than one layer could be not as clear as in exfoliated graphene, due to the lower electronic coupling between layers with not-ordered stacking. A narrow Lorentzian line (~30–40 cm^{-1}) can be used to fit the 2D-peak of both 1L and 2L CVD graphene, while for nGL ≥ 3 the width of 2D (Lorentzian) peak increase up to ~70 cm^{-1}. The 2D to G intensity ratio (I_{2D}/I_G) is used as a qualitative parameter to evidence the presence of very few graphene layers, being in this case I_{2D}/I_G >1.

Typical carbon nanotubes spectra resemble, for a lot of aspects, those of graphite. For example, G-band frequency and line shape are comparable to those of the E_{2g} phonon of graphite. The line width is, however, not a reliable criterion to distinguish CNT from graphite, since the line width may be affected by a number of factors such as tube diameter. In carbon nanotubes spectra D-band is around 1350 cm^{-1}; a group of peaks in the 1550–1600 cm^{-1} range constitutes the G-band and the peak around 2600 cm^{-1} is the 2D mode [69], as shown in Fig. 2.31.

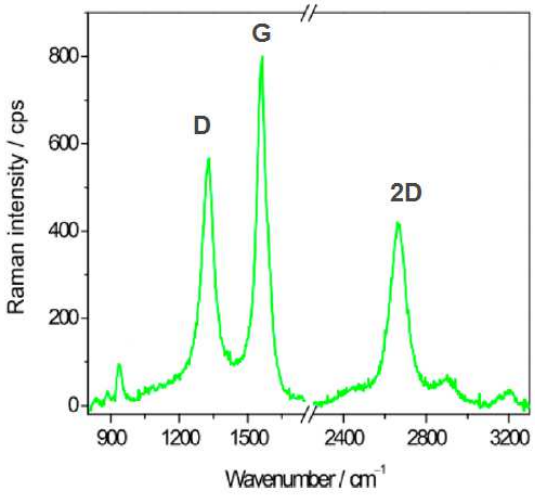

Fig. 2. 31 Typical Raman spectrum of MWNT. D, G and 2D band are shown [100].

In addition, it is known that some differences arise whether carbon nanotubes are single- or multi-walled nanotubes. Mainly, a low-frequency peak (<200 cm^{-1}), assigned to the A_{1g} symmetry radial breathing mode (RBM), depending only on the tube diameter, is the typical signature of a single walled. The D-band is known to be decomposed into two bands whose

separation depends upon the incident laser energy and G-band is clearly split into two bands in SWNT . Undoubtedly, the D/G intensity ratio (I_D/I_G) represents the most commonly used graphitization index. Thus, it monitors the amount of structural defects. The 2D/G intensity ratio (I_{2D}/I_G) is regarded as a long-range order indicator. As a result, the 2D/D intensity ratio (I_{2D}/I_D) is quite sensitive to the overall crystalline quality of the graphitic network and enhances with increasing mean inter-defect distance and/or long-range ordering (i.e. with increasing G/D and/or 2D/G ratios, respectively) [101].

2.5.2 Transmission Electron Microscopy

The transmission electron microscopy is a very powerful technique based on the interaction of a sample with a high energy beam of electrons, transmitted through it. This interaction can be used to observe features such as the crystal structures, dislocations and grain boundaries as well as chemical compositions of samples. High Resolution TEM (HRTEM) and Energy Dispersive X-ray spectroscopy (EDX) are particular TEM analysis used for this purpose. TEM microscopy operates on the same basic principles as the light microscope unless it makes use of electrons. Since the wavelength of electrons is much smaller than that of light, it can reveal the finest details as small as individual atom. The beam of electrons, generated from an electron gun, is accelerated through a high voltage up to 200 kV, necessary to penetrate the specimen. It is then focused into a thin coherent beam by the use of appropriate lens over the sample and transmitted depending upon sample thickness and its transparency to the e-beam. The transmitted beam is focused by the objective lens into an image on a charge coupled device (CCD) camera. The image then passed down through a number of lenses and is finally enlarged to the desired magnification.

Darker areas of the image represent those areas of the sample in which transmission of fewer electrons occurs and on the contrary lighter areas of the image represent the areas of the sample where electrons are mainly transmitted through. Typical TEM images of both graphene and carbon nanotubes are shown in Fig. 2.32.

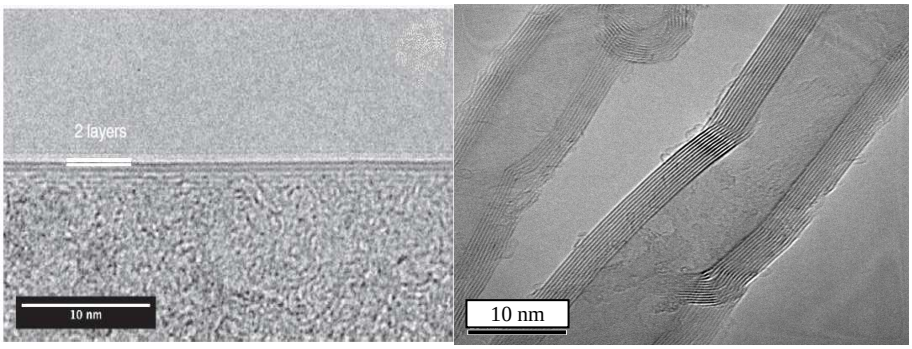

(a) (b)

Fig. 2. 32 TEM micrographs of (a) graphene [80] and (b) carbon nanotubes [102].

2.5.3 Scanning Electron Microscopy

A scanning electron microscope consists of an electron optical column, where a beam of electrons is generated by a suitable source, typically a tungsten filament, and accelerated through a high voltage between 20 and 60 kV. The electron beam is focused into a fine spot on the sample surface through appropriate lenses. This beam is scanned in a rectangular raster over the specimen and the intensities of various signals created by interactions between the beam electrons and the specimen are measured and mapped as variations in brightness on the image display. These signals include secondary electrons and backscattered electrons, mainly used to produce SEM images since vary with the morphology and topography of the sample surface, and X-rays radiations that can be used for elemental analysis.

The analysis can reveal information about sample including external morphology, chemical composition, and crystalline structure. Typical SEM images of both graphene and carbon nanotubes are shown in Fig. 2.33.

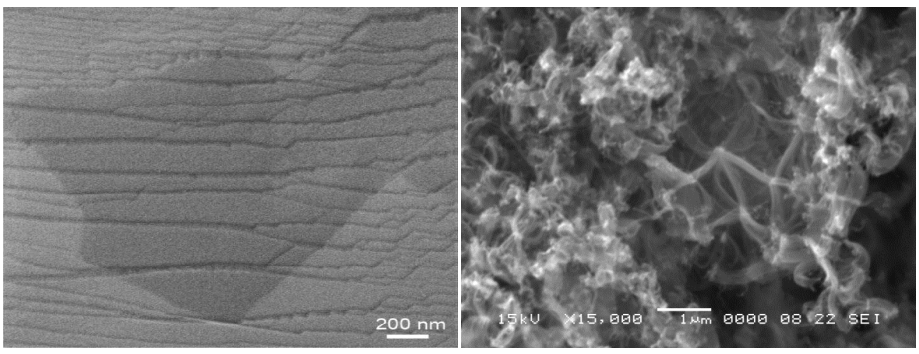

(a) (b)

Fig. 2. 33 SEM micrographs of (a) graphene [103] and (b) carbon nanotubes [100].

Both SEM and TEM are generally coupled with Energy-dispersive X-ray spectroscopy (EDX), an analytical technique used for the elemental analysis or chemical characterization of a sample. It relies on the investigation of the interaction of X-rays with the sample. Its characterization capabilities are due in large part to the fundamental principle that each element has a unique atomic structure allowing unique set of peaks on its X-ray spectrum. To stimulate the emission of characteristic X-rays from a specimen, a beam of X-rays is focused into the sample. The incident beam may excite an electron in an inner shell, ejecting it from the shell while creating an electron hole. An electron from an outer higher-energy shell then fills the hole, and the difference in energy between the higher energy shell and the lower energy shell may be released in the form of characteristic X emission. The number and energy of the X-rays emitted from a specimen can be measured by an energy-dispersive spectrometer. Thus the elemental composition of the sample is possible since the X-rays energy depends on the energy difference between the two shells and on the atomic structure of the element from which they are emitted.

2.5.4 X-Ray Diffraction

X-ray diffraction is an analytical technique mainly used for phase identification of crystalline solids. It is based on the interaction of X-radiation with matter, explained by Bragg's Law:

$$2d\sin\theta = n\lambda \qquad (2.\ 26)$$

where d is the distance between crystal planes layers, θ is the incident angle, n is an integer (the diffraction order) and λ is the incident wavelength (Fig. 2.34). When the path difference is equal to any integer value of the wavelength, a constructive interference will occur.

X-ray sources are the commonly used tubes, in which a tungsten filament, made incandescent by the passage of a current, is brought to a negative potential of 30-60 kV and emits electrons, which are directed, for effect of the electric field, to a target of pure metal (Cu, Cr, Fe, Co, etc.) acting as an anode. Copper is the most common target material, with

$\lambda_{K\alpha}$(Cu)=1.5418 Å. Characteristic X-ray spectra are produced and directed onto the sample.

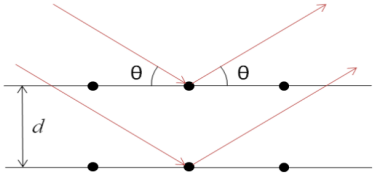

Fig. 2. 34 Geometry for interference of a wave scattered from two planes separated by d spacing.

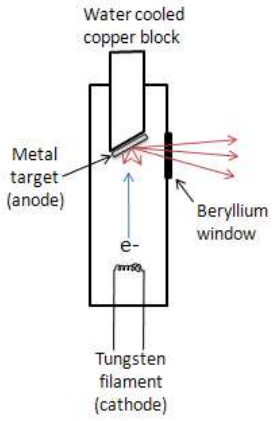

Fig. 2. 35 Sketch of a typical XRD tube.

Diffracted X-rays are then detected, processed and counted. By scanning the sample through a range of 2θ angles, all possible diffraction directions of the lattice can be obtained. The result is displayed in a diffractogram where the intensity of diffraction is reported versus the 2θ angle. Peaks can be unequivocally attribute allowing material identification, as in Fig. 2.36 where an XRD pattern of graphite powder is reported as an example.

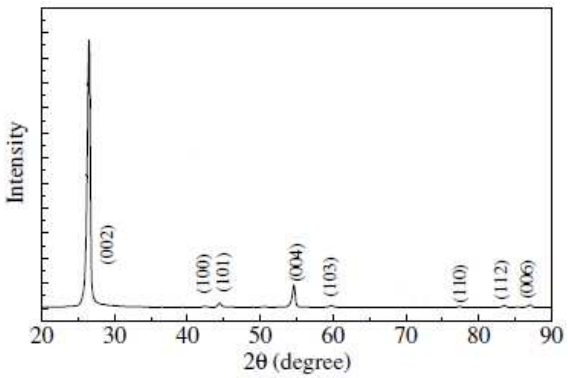

Fig. 2. 36 XRD pattern of graphite powder.

2.6 Synthesis and characterization of graphene

Graphene synthesis was realized in collaboration with ENEA-Casaccia Research center. Chemical vapor deposition using different hydrocarbon sources was utilized as the growth technique. In particular, both gaseous and liquid precursors, methane (CH_4) and ethanol (C_2H_5OH) were used. As previously described, the CVD system basically consists of a hot-wall tube furnace where the samples can be rapidly inserted and extracted from the hot zone. Carbon precursor is flown inside the quartz tube with Ar as carrier gas, at a pressure of few Pa. The growth is performed at high temperature, and a hydrogen flow is also added as it has been found necessary to obtain thin and highly-crystalline graphene films [81, 82, 80]. After the CVD process, the films are transferred onto Si/SiO_2 (300nm) by using cyclododecane as support material during the copper etching, as previously discussed [88].

Different synthesis condition in terms of flows, pressures, temperatures, time and cooling were experimented on account of the desired graphene properties. For instance, the growth on different Cu substrates, electro-polished and unpolished, was investigated by varying a comprehensive range of process parameters, such as reaction time (600, 60 and 20 s) and temperature (1000 and 1070 °C), aiming at producing graphene films with optimal characteristics in view of their use in optoelectronic and photovoltaic applications. In particular, the best film properties in terms of sheet resistance versus optical transmittance were obtained at 1070°C for 600 s, for both kinds of surfaces. On unpolished copper, a sheet resistance of ~500 Ω/sq with an optical transmittance around 92-94% at 550 nm was obtained. On electro-polished copper instead, the films were always predominantly monolayer and showed a sheet resistance ≥ 1000 Ω/sq with a transmittance of 97.4%.

Moreover, as shown by Raman spectra (Fig. 2.37 a), when electro-polished copper foils were used as substrates, the resulting graphene was a monolayer with small grains, probably in the nanometer range. In fact, since the beginning of the growth, a highly defective monolayer graphene film seemed to form ($I_G/I_{2D}<1$). The I_G/I_{2D} ratio progressively decreased with

time while the bands narrowed, demonstrating the formation of a single layer. By contrast, on unpolished foils, the growth of a few-layer film was obtained (Fig. 2.37 b). It could be noticed that since the earliest stages of the growth process, the graphene film was multilayer ($I_G/I_{2D}>1$), but, as the time passed, the D band decreased and the G and 2D bands started progressively narrowing. Longer growth processes allowed the lattice defects to heal, making the film increasingly more crystalline.

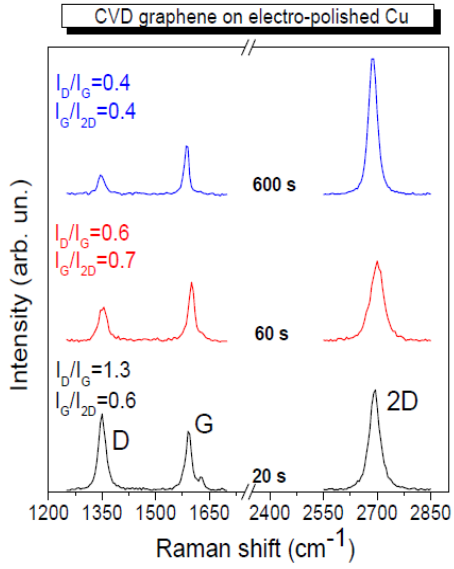

(a)

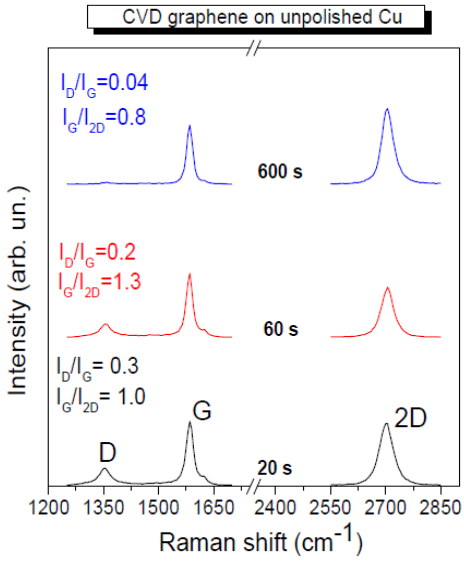

(b)

Fig. 2. 37 Raman spectra of graphene grown on (a) electro-polished and (b) unpolished Cu foil for 600, 60 and 20 s. Raman intensity ratio I_D/I_G and I_G/I_{2D} are reported [81].

The possibility to tailor graphene optical and electrical properties was further deepened by considering pyridine-CVD. Pyridine(C_5H_5N) is a liquid precursor similar to ethanol. The main difference between the two is that ethanol is generally used to make pristine graphene while pyridine can be used to form nitrogen-doped graphene. In fact, it is expected to lead to doped graphene by the insertion of nitrogen atoms in the growing carbon lattice, possibly improving the properties of graphene as a transparent conductive film. Again, different CVD parameters were considered and the resulting graphene was compared to the pristine one, grown by ethanol-CVD.

The optical transmittance and electrical conductivity of the films were measured to evaluate their performance as transparent conductive electrodes. Graphene films grown by pyridine reached an electrical conductivity of $14.3 \cdot 10^5$ S/m, higher than that reported in pristine graphene ($10.4 \cdot 10^5$ S/m). A more detailed discussion can be found elsewhere [81, 82].

2.6.1 LPE graphene

Graphene used as sensing material in the realized device was synthesized by Liquid Phase Exfoliation. This method, as previously mentioned, basically consists in the separation of the graphite planes by the sonication of graphite powder dispersed in a solvent. The mostly used solvents are not only expensive, but require also special care in handling due to their toxicity, as N-methyl-pyrrolidone (NMP) or Dimethylformamide (DMF). It has been therefore envisaged the possibility to use environmentally friendly solvents. Recently, the Enea Portici Research Center has successfully realized a green mixture of iso-propanol (IPA) and ultrapure water in volumetric ratios 1:5 with a surface tension value suitable to achieve the target value of ~40 mN/m, characteristic of graphene [104]. The applied method not only resulted environmentally friendly and able to exfoliate graphite, but it was moreover demonstrated the reproducibility in yield of few layered graphene, whose flakes quality was comparable with those obtained using NMP.

In order to synthesize graphene the procedure was reproduced [105]. In detail, a suspension was prepared by dispersing commercially available

graphite flakes (Natural Graphite) in the concentration of 2.5 mg/ml and sonicated in an ultrasonic bath for about 48 h with power set at about 40 W. Thereafter as to separate the unexfoliated graphite from the thinner flakes, a centrifugation process for 45 min at 1000 rpm was carried out [104].

LPE graphene was characterized by means of complementary techniques in order to obtain morphological, structural and electronic information. Dynamic light scattering (DLS) was used to determine the size distribution profile of graphene flakes after the sonication process, result~~ed~~ resulting in a few hundred nanometers. Furthermore, the technique was also very useful to check the same size distribution profile even after weeks or months, in order to establish whether flakes in the solution were still separated or not. The main characterization was realized through micro-Raman spectroscopy. Raman analysis could be performed after depositing few microliters of the feed solution onto Si wafers coated with SiO_2 thin film (250 nm). Spectra have been recorded at room temperature using a HORIBA Scientific LabRAM HR Evolution Raman spectrometer with an integrated Olympus BX41 microscope (Fig. 2.38). Laser excitation wavelength of 532 nm (2.33 eV) was focused on the sample surface using a X100 objective with a spot size of approximately 1 μm in diameter. Low laser power (below 1 mW) was used to minimize sample heating and possible damages. Because of possible surface inhomogeneity, spectra were recorded on different locations of the sample.

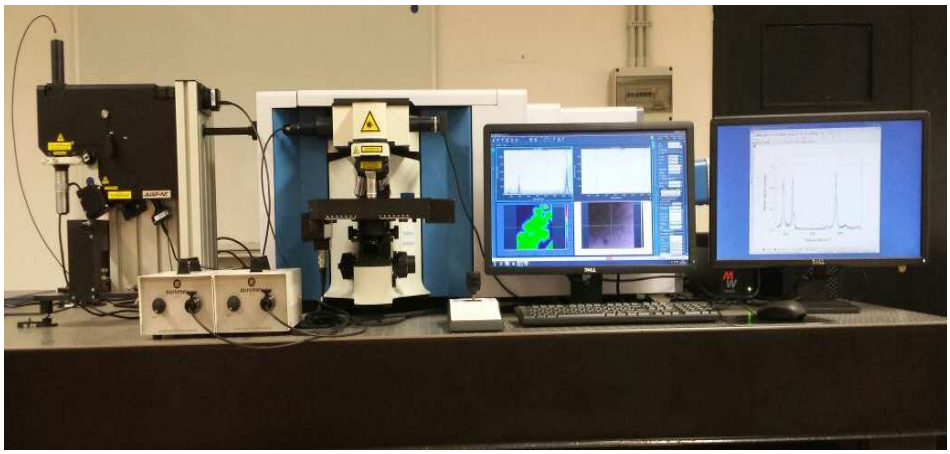

Fig. 2. 38 HORIBA Scientific LabRAM HR Evolution Raman spectrometer (Optical Spectroscopy Laboratory - Mediterranea University of Reggio Calabria).

Typical Raman spectrum for LPE graphene is shown in Fig. 2.39. For comparison purposes the graphite spectrum (black line) is shown too. Each peak, as previously discussed, has been opportunely assigned.

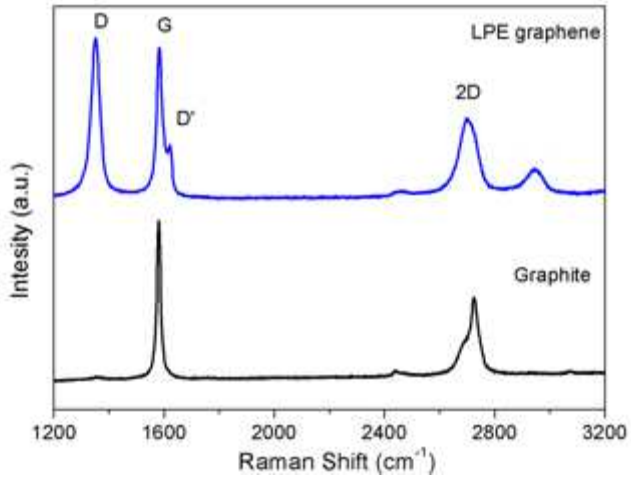

Fig. 2. 39 Raman spectrum of the synthesized LPE graphene (blue line) compared with that of graphite.

By the comparison of the two profiles, in terms of the rise of D (~1350 cm^{-1}) and D' (~1620 cm^{-1}) peaks, as well as the change of the 2D band (~2700 cm^{-1}) shape proved the successful exfoliation of graphite.

As regard the D and D' peaks, it is well known that these bands are activated by defects [106]. Some authors proved that intensity ratio between D and D' peak can be used to discriminate between sp^3-defects, vacancy-like defects and boundaries. They found that the $I_D/I_{D'}$ ratio is maximum (~13) for defects associated with sp^3 hybridization, it decreases for vacancy-like defects (~7) and reaches a minimum for boundary-like defects (~3.5). In the displayed Raman spectra the values of $I_D/I_{D'}$ are calculated up to 2.5, approximately compared to the boundary defects value [106]. Usually, the intensity ratio between D and G peak can be exploited to infer information on defects. For instance, acquired Raman spectra showed I_D/I_G ranging from 0.5 up to 1, similar to the values reported in the literature, where the defect peaks are assigned to flake edges rather than other kind of defects [107]. Moreover, according to I_D/I_G ratio and sonication process time, it has been previously reported that defects are likely associated with the edges while the

bodies of the flakes are relatively defect free, proving the efficiency of the liquid phase exfoliation technique [108].

The 2D band features are examined in Fig. 2.40 where graphite and exfoliated material are both shown.

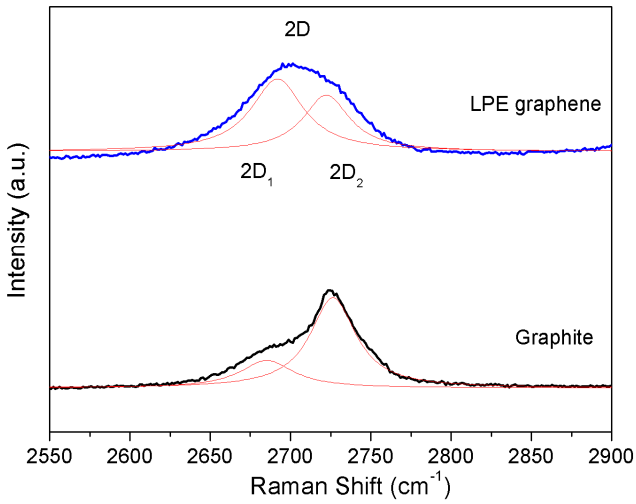

Fig. 2. 40 Lorentzian components of the 2D band of both LPE graphene and graphite.

The 2D peak in bulk graphite consists of two Lorentzian components $2D_1$ and $2D_2$, roughly 1/4 and 1/2 the height of the G peak, respectively [94]. As the number of graphene layers increases, the relative intensity of the $2D_1$ peak significant decreases so that the Raman spectrum becomes hardly distinguishable from that of bulk graphite. On the contrary, as the number of graphene layers decreases, $2D_1$ peak intensity increases until it becomes, in general, the only component in single layer graphene. In this case, 2D band can be fitted with a single, sharp Lorentzian [94]. In the experimental case the evolution from graphite to few graphene layer is shown (Fig. 2.40).

Transmission Electron Microscopy was further used in order to extract morphological information regarding the exfoliated material. TEM images have been recorded by a FEI TECNAI G12 Spirit-Twin operating at 120 kV. In order to prepare the sample, a drop of the graphene suspension was dried on the 400 mesh holey-carbon coated copper grid.

TEM analysis proved the high degree of graphite exfoliation showing the presence of both single-layer and few-layer flakes, sometimes arranged in a nearly continuous film (Fig. 2.41). Moreover, the mean size of the flakes

resulted in the range of few hundred nanometers. The huge amount of edges in the films finally confirms the boundary-like nature of defects, as previously stated.

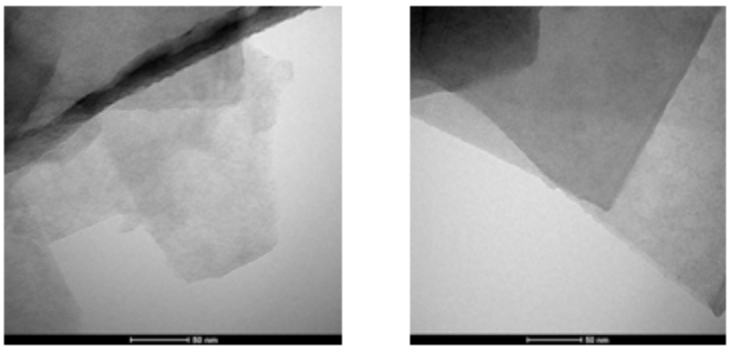

Fig. 2. 41 TEM micrographs of LPE graphene.

In summary, graphene was successfully exfoliated and showed a good structure for gas sensing applications. Indeed, defected graphene has been demonstrated to be more reactive towards molecules. It has been reported that gaseous analyte shows much stronger adsorption on the doped or defective graphene than that on the pristine graphene [109] Therefore, the micrometric dimensions of the flakes and, in turn, the presence of edges are very reactive and may represent anchor points for gas molecules to be detected.

2.7 Synthesis and characterization of CNT-based sensing materials

Carbon nanotubes are receiving a great deal of interest in the sensing field. Indeed, the high surface-to-volume ratio, high conductivity and mechanical stability make CNT very attractive for this kind of application. They can effectively be used as advanced miniaturized chemical sensors [74] since their electrical resistivitiy was found to change sensitively on exposure to gaseous ambient. Therefore, by monitoring the change in the conductance of nanotubes, the presence of potential gaseous analytes can be precisely detected. Moreover, CNT have also shown their potentiality towards liquid analytes, as in the electrochemical field. For instance, single- and multi-walled

carbon nanotubes together with other different nanocarbons, namely carbon black and dahlia-like carbon nanohorns, were investigated and tested as electrochemical devices, showing their potentiality in this sensing field [110]

In addition, CNT can be synthesized in order to tailor their final properties and can be even functionalized to increase the interaction with analytes, thus changing their selectivity.

2.7.1 Synthesis and characterization of CNT

An attempt to grow carbon nanotubes on the gram scale with peculiar properties was carried out at the University of Messina (DIIECI). CNT were synthesized by chemical vapor deposition of methane (CH_4) over a set of cobalt−molybdenum−magnesium catalysts.

Basically, the effect of new bi-metallic and tri-metallic Co, Mg and Mo catalysts was studied in order to clarify the role played by the cobalt phase in the growth of carbon nanotubes by the catalytic chemical vapor deposition of CH_4. An optimization of synthesis conditions for CNT large scale production was also performed.

Bi-metallic cobalt-molybdenum (Co-Mo), cobalt-magnesium (Co-Mg) and magnesium-molybdenum (Mg-Mo) catalysts were synthesized by the sol–gel method. Basically, metal nitrate precursors $Mg(NO_3)_2 \cdot 6H_2O$ and/or $Co(NO_3)_2 \cdot 6H_2O$ were mixed in a citric acid solution (3 g of citric acid in 10 mL of H_2O) and stirred until complete dilution was achieved. The solution was dried at 393 K into a foamy paste and then, in the case of catalysts containing molybdenum, was mixed with molybdenum powder. All the catalysts were calcined in static air at 1023 K for 5 h (Fig. 2.42 a,b,c).

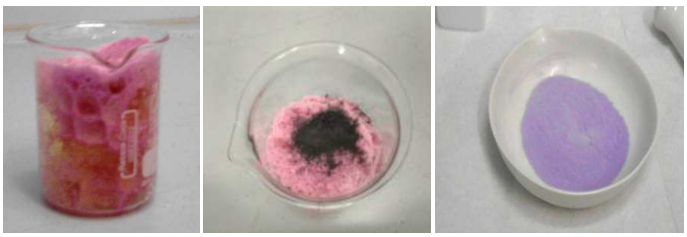

(a) (b) (c)

Fig. 2. 42 Detail of catalyst preparation: (a) foamy paste Co-Mg based, (b) mixture of the foamy paste with molybdenum powder, (c) calcined catalyst.

CNT were grown in a quartz tube placed in a horizontal furnace (Fig. 2.43). The catalyst mass (50 mg) was uniformly spread as a thin layer in a quartz boat and pre-heated up to the synthesis temperature (1173 K) under helium flow. Helium was then replaced by the mixture of CH_4 and H_2. The reaction was stopped after 30 min and the reactor was allowed to cool under helium flow. Afterwards, the solid was collected from the quartz boat and characterized by several complementary techniques.

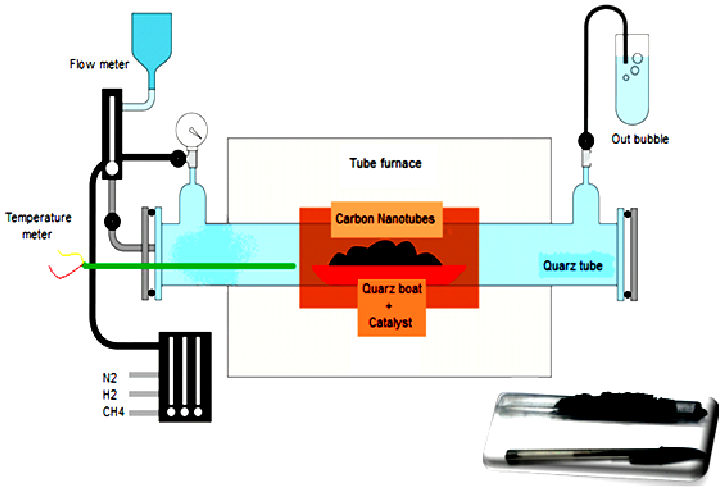

Fig. 2. 43 Sketch of the CVD synthesis system. Detail of the synthesized carbon nanotubes inside the quartz boat.

The synthesized samples, featured by a sponge-like morphology, consist in three dimensional networks of dense bundles of straight CNT, which interconnect exfoliated catalyst affording macroporosity in the spaces between them and entanglements of curly tubes. Results of the systematic investigation by multi-wavelength visible micro-Raman spectroscopy carried out in order to investigate the tensional states arising from the interconnections among CNT bundles allow evidencing the existence of a correlation between the evolution of Raman spectral profiles and the different extent of strain suffered by CNT with changing network morphology. Indeed, the D- and 2D-bands generally centered at 1326−1331 cm^{-1} and 2666−2670 cm^{-1}, respectively, appeared remarkably downshifted with respect to the expected positions (1346 and 2692 cm^{-1}). As shown in Fig. 2.44 a, the same occurs if different energy in the visible range are considered. The observed

downshifts was argued to be the effect of the tensile strain originating from the formation of interconnected CNT bundles (Fig. 2.44 b).

(a)

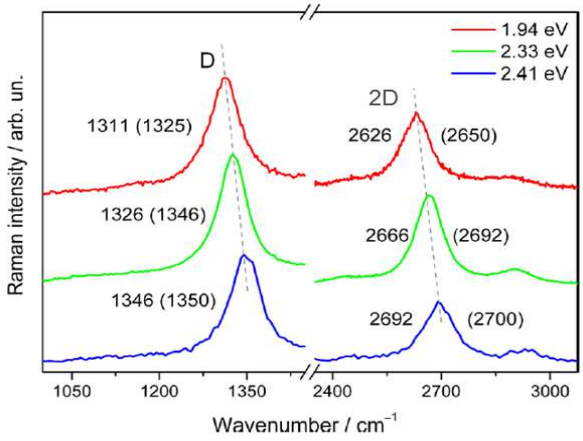

(b)

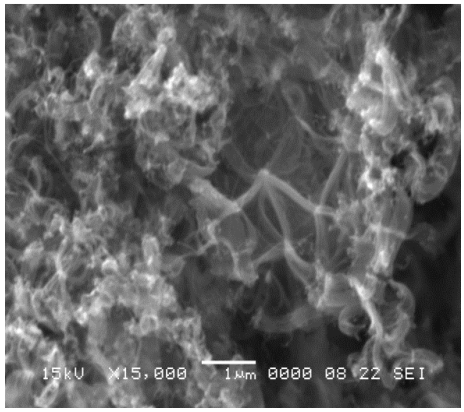

Fig. 2. 44 (a) D- and 2D-band region of the spectra excited at different energy. The measured wavenumber positions (in cm^{-1}) are reported together with the expected ones (in brackets). (b) SEM image of CNT sponge-like morphology [100].

The interest in these nanostructures is related to their huge potential in all applications that could benefit from macroporosity of the network and high reactivity, with which the strained CNTs are well-known to be endowed.

The detailed results of this work can be find elsewhere [102, 100].

2.7.2 Synthesis and characterization of ternary TiO_2/CNT/Pt composites

Metal oxide semiconductor gas sensor and electrochemical sensor were both realized by using an innovative ternary compound based on carbon nanotubes, titanium dioxide (TiO_2) and platinum (Pt) nanoparticles. Their

combination result in a new performing material able to detect both gaseous and liquid analyte [111].

Titanium dioxide is a material widely used in most research and applicative fields due to its low cost, chemical inertness, non-toxicity, biocompatibility and eco-friendly nature. For example, TiO_2 is increasingly utilized in catalysis, photo-catalysis, energy storage, solar energy conversion, electro-chemistry and sensing [112, 113, 114]. However, the wide band gap (3.2 eV and 3.0 eV for anatase and rutile, respectively) and low electric conductivity ($\approx 10^{-12}$ S cm^{-1}) of titania hinder its extensive use. Many efforts have been made to solve this problem combining TiO_2 with conductive carbonaceous additives, such as activated carbon or CNT, in simple mixtures or as nanocomposite materials. Indeed, if the organic component is a good electrical conductor, the resulting composites can form a perfect integrated structure with a developed electron conductive network and shortened current transport paths, improving the poor electrical properties and charge transfer of pure metal oxides [19]. As for sensing applications, CNT appear as an ideal support due to their intrinsic electrical properties.

Micro-emulsion (ME) and electro-spinning (ES), were both experimented in samples preparation. However, despite the easy of the implemented ES technique [115], the obtained samples showed poor characteristic in the sensing field in favor of better features in the optical field. Therefore, for the synthesis of this kind of samples, ME was just considered. This method is one of the most promising approaches to easily and rapidly prepare nanometer-sized particles and, more generally, materials with high specific superficial area. Granting an optimal dispersion of the active phase into the colloidal solution, it may represent a step forward with respect to the classical sol-gel (SG) technique. TiO_2/CNT/Pt nanohybrids prepared by ME method, with their three-dimensional network texture, can be then an ideal platform for both chemical and electrochemical sensors.

In order to prepare TiO_2/CNT nanohybrids, commercial CNT (Helix Materials; nominal outer diameter: 10–30 nm; nominal length: 0.5–40 μm; purity: >95%) were firstly functionalized. In brief, as-received CNT (0.5 g) were dispersed in concentrated HNO_3 (65%) and refluxed at 110°C for 18 h

under magnetic stirring (Fig. 2.45). They were then rinsed with distilled water until the pH of the solution was neutral, and finally dried at 80°C in vacuum oven.

Fig. 2. 45 Carbon nanotubes functionalization system.

Two TiO_2/CNT nanohybrids with the same nominal composition were prepared. The two samples only differed for the order in which CNT were added to the solution during their preparation. In one case (sample ME-1), functionalized nanotubes (fCNT) were added to microemulsion AB leading to solution-ABC. In the other case (sample ME-2), fCNT were mixed with solution-B to give solution-BC, and only after this solution-A was added finally leading to solution-BCA (Fig. 2.46). Both solutions ABC and BCA were magnetically stirred for 2 h. After filtration, the precipitates were washed with distilled water and finally dried at 60°C in oven for a day.

In order to obtain the crystalline form of the oxide, the three powder samples so prepared were calcined in air at 250°C for 2 h, and subsequently annealed in N_2 at 500°C for 2 h. A portion of each of them was set aside for the analyses; the remaining parts were further processed for the platinum addition. Platinum (2 wt%) was loaded onto the samples by wetness impregnation (WI) technique. The precursor (platinum acetylacetonate) was dissolved in acetone and then added, drop by drop, to the powders. In order to promote the metal activation, Pt-loaded samples were annealed in 5% H_2/N_2 atmosphere at 200°C for 2 h. An additional CNT/Pt reference sample was further prepared following the same procedure. Codes and nominal composition of the synthesized samples are shown in Table 2.1.

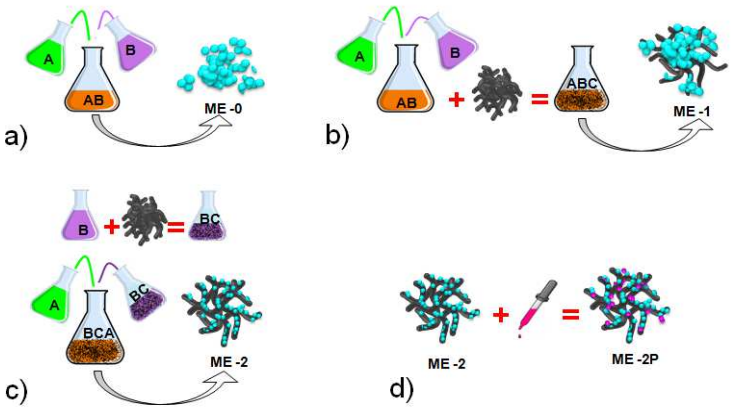

Fig. 2. 46 Scheme of the experimental procedure utilized for the synthesis by micro-emulsion method of (a) TiO_2/CNT nanohybrids (b) ME-1 and (c) ME-2. (d) Subsequent wet impregnation step.

Table. 2. 1 Codes and nominal composition of the synthesized samples.

Code	Preparation method	Sample typology	Nominal composition (wt%)		
			TiO_2	CNTs	Pt
ME-0	ME	TiO_2	100.0		
ME-1		TiO_2-fCNTs	35.0	65.0	
ME-2		fCNTs-TiO_2	35.0	65.0	
ME-0P	WI	TiO_2/Pt	98.0		2.0
ME-1P		TiO_2-fCNTs/Pt	34.3	63.7	2.0
ME-2P		fCNTs-TiO_2/Pt	34.3	63.7	2.0

All the samples prepared were analyzed by means of a combination of complementary techniques, at the University of Messina. Their microstructure and crystalline phase of the oxide were investigated by micro-Raman spectroscopy (MRS). Raman scattering (excitation energy 2.33 eV) was measured in air at room temperature using a Horiba XploRA spectrometer equipped with a confocal microscope and Peltier cooled CCD. The 100X microscope objective lens was used. The use of a low laser power density prevented excessive heating of the samples and annealing effects. Spectra from several random positions on each specimen were collected on account of the possible spatial non-homogeneity of the samples.

In the lower-frequency region of the spectra (Fig. 2.47 a) the features arising from titania vibration modes, both anatase and rutile, were detected

[116]. The comparison with reference library spectra reveals that, in the absence of CNT (sample ME-0), crystalline anatase-TiO_2 is obtained. In the presence of CNT, instead, anatase (sample ME-1) or rutile (sample ME-2) can be formed depending on the details of the preparation procedure, while the subsequent addition of platinum (samples ME-0P, ME-1P and ME-2P) has no effect on the crystalline phase of the oxide (Fig 2.47 b).

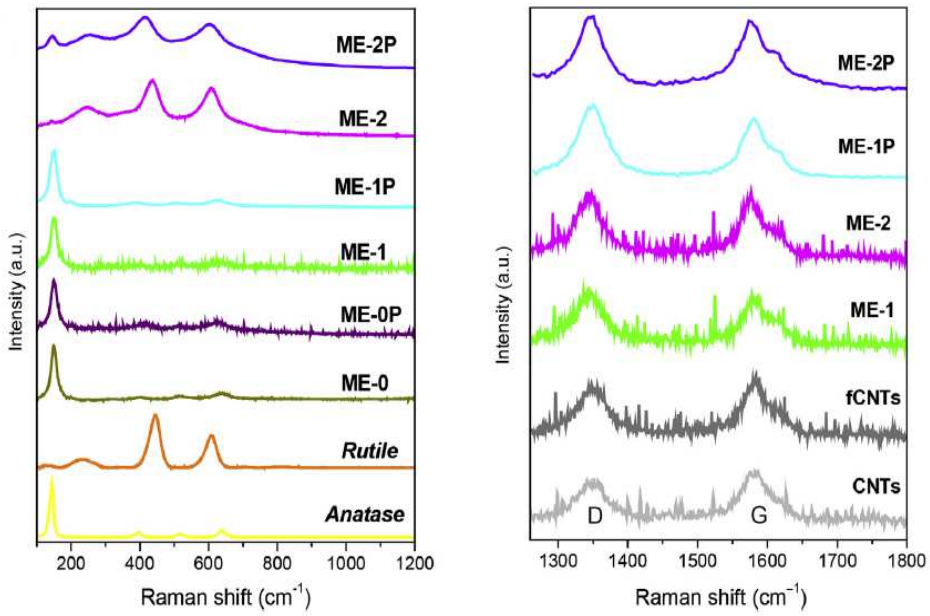

Fig. 2. 47 Micro-Raman spectra of the investigated materials. (a) TiO_2 mode, (b) Csp^2 region.

Texture and morphology of nanohybrids were investigated using a Philips XL-30-FEI scanning electron microscope (operating voltage: 20 kV) equipped with an energy-dispersive x-ray spectrometer (EDX). Samples were placed over an aluminum stub covered by a silver print layer to increase the conductivity. SEM analysis reveals that samples ME-1P (Fig. 2.48 a) and ME-2P (Fig. 2.48 b) exhibit different morphologies, confirming that the order in which CNT are added to the solution is a critical step.

In sample ME-1P both large agglomerates and isolated grains of titania are observed on the CNT mat, while sample ME-2P looks spatially more homogeneous, CNT being decorated by smaller sized TiO_2 particles.

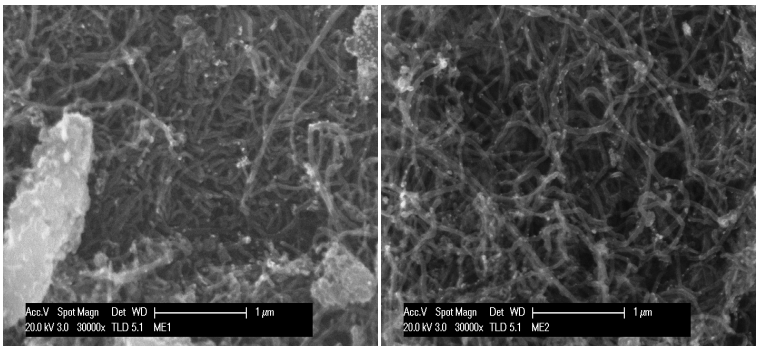

(a) (b)

Fig. 2.48 SEM micrographs of TiO_2/CNTs/Pt nanohybrids. Images refer to samples ME-1P (a) and ME-2P(b).

Finally, shape and size distribution were evaluated by transmission electron microscopy. Analyses were carried out with a JEOL JEM 2010 electron microscope (LaB6 electron gun) operating at 200 kV, equipped by a Gatan 794 Multi-Scan cooled charge-coupled detector (CCD) camera for digital imaging. Samples were dispersed in isopropanol and sonicated; then a drop of each suspension was dried on the 400 mesh holey-carbon coated copper grid.

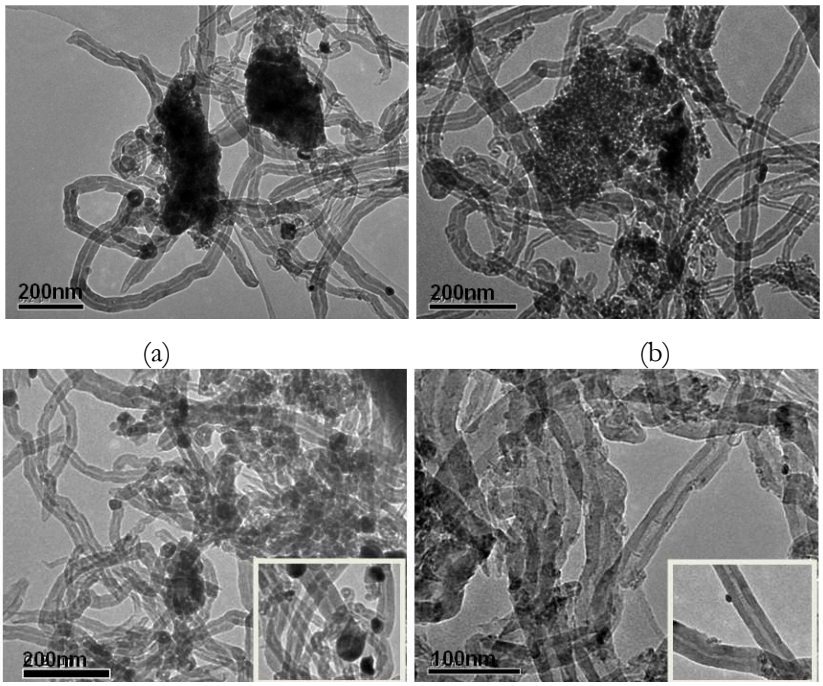

(a) (b)

(c) (d)

Fig. 2.49 TEM micrographs of TiO_2/CNT/Pt nanohybrids. Images refer to samples ME-1P (a,c) and ME-2P (b,d). Inset in (c) and (d) refer to Pt particles on samples ME-1P and ME-2P, respectively.

TEM analysis further shows that Pt particles in sample ME-1P (Fig. 2.49 a-c) have bigger average size than in sample ME-2P (Fig. 2.49 b-d).

In order to explain the different microstructures and morphologies observed in the two samples, we should consider that functional groups introduced by the acid treatment on the surface of CNT are believed to act as anchoring sites for the titania particles [23]. Information on the occurrence of interfacial interaction between TiO_2 and CNT, mediated by the number of functional groups and their nature and, more generally, on the microstructure of the samples, can be inferred by quantitatively analyzing the higher-wavenumber region of MRS spectra, dominated by the bands associated to the Csp^2 vibration modes.

Functionalization brings about an increase of the structural disorder in the graphitic lattice I_D/I_G increases from 1.17 in as-received CNT up to 1.25 in the chemically oxidized ones. An higher degree of structural disorder is also provide by attachment of the oxide particles, at the native defect sites or at the functional groups introduced on the CNT walls. Indeed, in sample ME-1P I_D/I_G is found to rise up to 1.46; oppositely, in sample ME-2P it decreases down to 0.95. Inoue et al. interpreted the I_D/I_G lowering observed in TiO_2-fCNT composites prepared by SG technique as an evidence of the interaction between carbon nanotubes and nanostructured TiO_2 [117]. They attributed the decrease to the suppression of the signal coming from the outer walls of CNT, chemically modified by the attached oxide molecules, with the inner unmodified tube walls only contributing to Raman intensity. Indeed, as known [93], only sp^2-type lattice defects contribute to the D-band intensity. Thus, the changes in I_D/I_G presently observed would indicate that in the case of sample ME-1P the formation of TiO_2/CNT nanohybrids involves an increase of the sp^2-defect density such as bond-angle and bond-length distortions. Instead, in the case of sample ME-2P the density of sp^2 lattice defects decreases, most probably in favor of that of the non-sp^2 (possibly sp^3) ones, and stronger oxide/nanotube interaction occurs. After chemical oxidation, the D- and G-bands slightly shift toward higher wavenumbers, from 1346.2 cm^{-1} and 1580.1 cm^{-1} in CNT to 1350.3 cm^{-1} to 1584.3 cm^{-1} in fCNT, respectively, as an effect of the electron transfer from graphitic lattice

to oxygenated moieties [118]. The electron-donor character of TiO_2 over the carbon nanotubes causes the G-band to shift toward lower frequencies in TiO_2/CNTs nanohybrids. In sample ME-2P the downshift is larger than in sample ME-1P, 1575.4 cm^{-1} against 1578.6 cm^{-1}. This might indicate that electron transfer from the oxide to the graphitic lattice occurs to greater extent, confirming that interaction at the interface between oxide and nanotubes is stronger.

It can be reasonably envisaged that when CNT are added to the micro-emulsion utilized for the preparation of reference sample ME-0, the aggregation between oxide nanoparticles (NPs) is favored over the interaction with CNT. This leads to the formation of larger titania agglomerates, non-homogeneous in size and spatial distribution, weakly interacting with the graphitic phase. Also the crystalline phase (anatase) is the same as in the absence of CNT. On the contrary, the addition of CNT before the onset of precipitation (sample ME-2) prevents the agglomeration of titania particles and favors their homogeneous dispersion over the graphitic mat. Smaller-sized rutile particles are formed with good surface contact and interfacial interaction, as demonstrated by the changes in Raman spectral profile (I_D/I_G decrease and larger G band downshift). In addition as suggested by Hu et al. [119], the decrease of pH provoked by the addition of CNT to the microemulsion may be responsible for the formation of the different oxide phase, rutile rather than anatase.

3
Chemical sensing devices

Low dimensional carbon-based sensing devices will be presented in this chapter. First, the experimental activity, carried out at the Enea Portici Research Center and related to the design, fabrication and characterization of a Graphene/Silicon Schottky diode acting as an ammonia gas sensor, will be investigated in detail.
Then, carbon nanotubes based sensors, MOS and electrochemical devices, will be considered. Their performance towards hydrogen and hydrogen peroxide will be discussed.

3.1 Graphene/Silicon Schottky junction gas sensor

Graphene-silicon Schottky diodes acting as gas sensors were fabricated and tested at the Enea Portici Research Center [105, 120]. The synthesis of the devices was entirely performed in clean room. The need for a clean process arises because dust particles in the air can settle on semiconductor wafers during devices fabrication causing defects, which result in circuit failure.

The work consisted in several steps, namely the preparation of the silicon substrate, the realization of both the Ti/Pd/Ag cathode and Cr/Au anode, the transfer of graphene sensible material and finally the gas sensing test. The main steps followed for the preparation of the junction are reported in Fig. 3.1(a-d).

The substrate used for the realization of the device was an n-type commercially available silicon wafer (phosphorus atoms concentration ≈5 $x10^{15}$ cm^{-3}) with <111> orientation of the crystallographic surface, 100 mm diameter and 525 microns thickness.

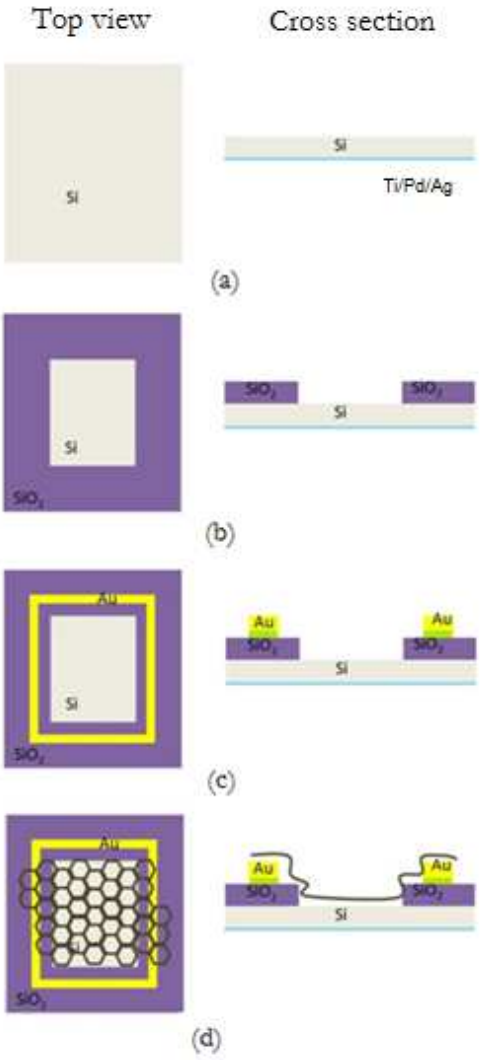

Fig. 3. 1 Main steps of device realization: (a) Ti/Pd/Ag back contact on the silicon substrate; (b) SiO_2 layer with exposed silicon window; (c) Cr/Au top contact; (d) LPE graphene layer.

After the cleaning of the surface, the back ohmic contact was realized with a titanium/palladium/silver alloy. As reported in literature, titanium provides a low rate of recombination at the surface, palladium protects titanium from oxidation while the last layer of silver provides a low contact resistance and chemical resistance [121], the latter particularly suitable for gas sensors.

Thin metal films deposition over semiconductor substrates is a basic process in the realization of electronic devices. It is commonly used to realize rectifying or ohmic contacts, to form thermal and chemical barrier coatings or to modify surface properties (as for reflectivity in optic applications). The

deposition process can be mainly classified into chemical vapor deposition (CVD) and physical vapor deposition (PVD). In CVD, the film growth takes place at high temperatures involving chemical reactions that usually lead to undesired products with the formation of possible impurities in the film. The PVD process is instead characterized by lower deposition temperatures without any kind of impurities even if deposition rates are slower. Among the available techniques, the electron beam physical vapour deposition was used. Metals deposition was realized by the Roth and Rau MS-600 e-beam evaporator (Fig. 3.2).

Fig. 3. 2 Roth and Rau MS-600 e-beam evaporator (Enea Portici Research Center).

Basically, an electron beam is generated from a filament and accelerated to a high kinetic energy by the combination of both magnetic and electric fields, within a vacuum environment (less than 10^{-7} mbar). The e-beam is directed towards the source materials, contained in particular crucibles characterized by both thermal and chemical compatibility with the process temperature and the evaporation materials, respectively. The thermal energy that is produced heats up the material causing it to sublimate. As soon as temperature and vacuum level are sufficiently high, the resulting vapor creates a coating on the substrate surfaces positioned above the evaporating materials. A schematic illustration of the e-beam evaporator is shown in Fig. 3.3.

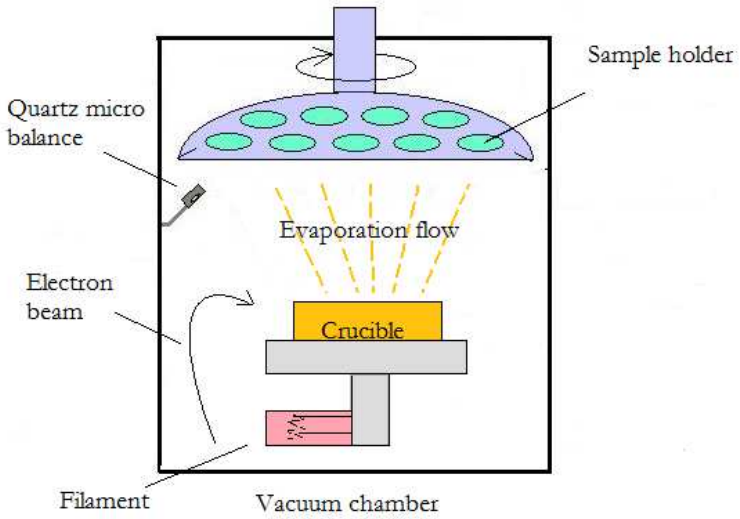

(a)

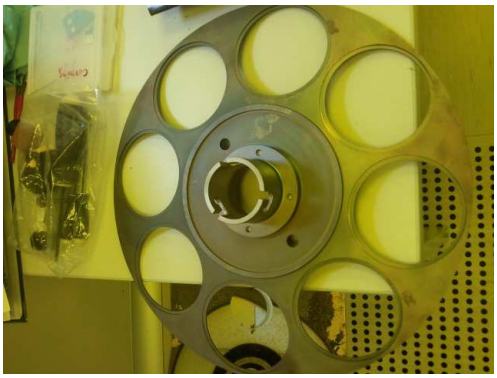

(b)

Fig. 3. 3 (a) Schematic representation of the e-beam evaporator; (b) Evaporator substrate holder.

The three metals were loaded inside the e-beam evaporator. The possibility to load a number of crucibles with different metals allowed to preserve the vacuum conditions and to make the process faster, since materials evaporation could be carried out in sequence. The deposition parameters, growth rate and film thickness, were set for each metal and systematically checked during the deposition since their variation can negatively affect the final characteristics of the thin film. The film thickness was precisely monitored using a quartz micro balance which, upon the change in frequency of a quartz crystal resonator, measures the mass variation per unit area caused by the film deposition on the surface of the acoustic

resonator. The relation between the film thickness and material physical parameters is expressed as [122]:

$$l_f = -\frac{N_q \rho_q \Delta\nu}{\rho_f {\upsilon_q}^2} \tag{3. 1}$$

where l_f and ρ_f are the evaporated film thickness and density, respectively; $N_q = l_q \upsilon_q$ is the frequency constant; l_q, υ_q and ρ_q are the quartz crystal thickness, resonant frequency and density, respectively; $\Delta\nu = \upsilon_c - \upsilon_q$ with υ_c the system frequency after the evaporation process.

Thickness values of 35 nm, 35 nm and 1000 nm were established for Ti, Pd and Ag, respectively. After the evaporation and condensation processes, a further heat treatment was carried out for 20 minutes at 350°C.

Then, the wafer was opportunely cut into smaller pieces of 1.5-2 cm of side and further processing in order to create the insulating layer. Silicon dioxide (SiO_2) was evaporated on the top of the structure. This deposition was masked to leave an area of exposed Si of 4x4 mm^2 as cathode of the junction. To this purpose a layer of PDMS (Polydimethylsiloxane) was used as a mask tanks to its remarkable resistance to temperature, chemical attack and oxidation. PDMS was mixed with a liquid curing agent in the ratio 10:1. The mixture was maintained under vacuum and heated up to 100°C for 1 hour. Then, it was uniformly spread on a substrate and cut to obtain the mask of appropriate size (4 mm side). The square mask was then placed in the centre of the silicon substrate pieces. Then, a 250 nm SiO_2 thick layer was deposited at a low evaporation rate. After the evaporation process (the same as previously described for metals evaporation), the mask was removed leaving exposed the underlying Si substrate (Fig. 3.4 a-c).

Successively, a second mask was applied to the substrates in order to create a metallic ring (Fig. 3.4 d-f). A wider PDMS mask of 6x6mm^2 was used to cover the center of the structure again, whereas an hollow squared mask was used for the external region. Thereafter, 30 nm of chromium and 120 nm of gold were evaporated in sequence as previously explained. Chromium was used as interface layer, because of the lack of grip between Au and SiO_2.

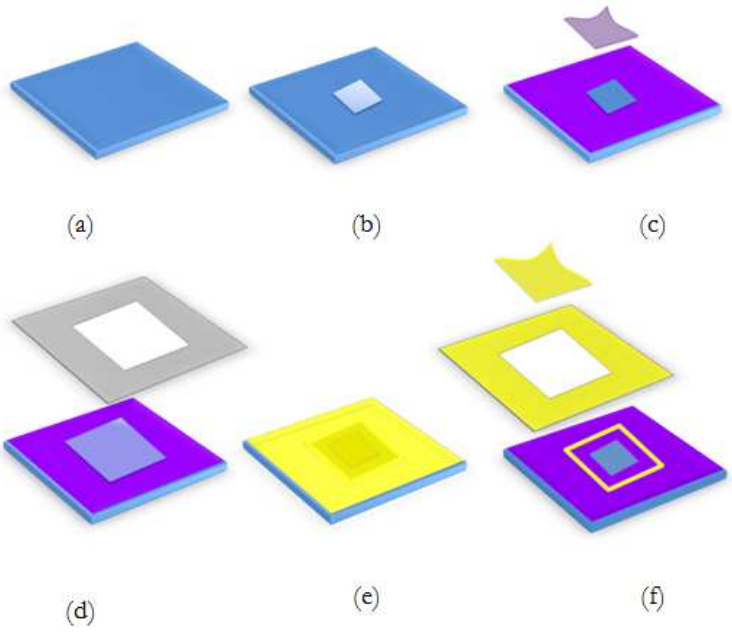

Fig. 3. 4 Schematic illustration of (a) silicon wafer, (b) PDMS mask 4 mm of side on the silicon substrate, (c) SiO_2 layer surrounding the silicon window, (d) hollow squared and 6 mm of side PDMS masks on the substrate, (e) Cr-Au evaporated contact, (f) final device.

Finally, the last step carried out to complete the devices was graphene transfer. In order to realize the interface junction between silicon and graphene, few microlitres of the realized graphene feed solution were drop-casted on the base structures and let dry at room temperature (Fig. 3.5). Graphene covered simultaneously the top Au ring contact, determining an ohmic contact, and the silicon window, forming instead a rectifying contact.

(a) (b)

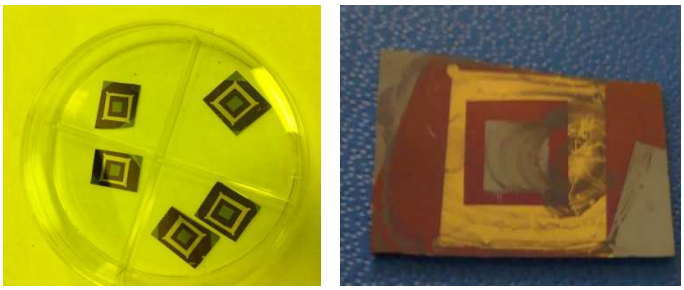

(c) (d)

Fig. 3. 5 Pictures of the different processing steps of devices: (a) samples placed on the evaporator dome, (b-c) intermediate stage of devices production, (d) example of a complete device.

3.1.1 Electrical characterization

After the characterization of the sensible material, already discussed in Chapter 2, electrical characterization of the device was performed too. As shown in the cross section of Fig. 3.6, the heterojunction was realized at the interface between graphene and silicon. Since the diode is not ideal, the considered equivalent circuit has a series resistance that takes into account all the circuit losses.

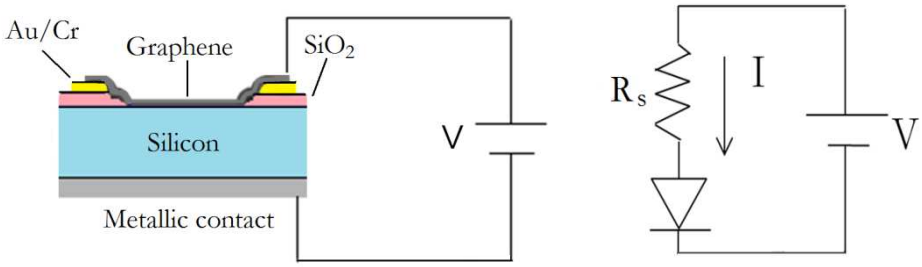

Fig. 3. 6 Device cross section and equivalent circuit.

The electrical characterization of graphene/Silicon Schottky diodes allows to evaluate the characteristic parameters such as series resistance R_s, ideality factor η and Schottky barrier height (SBH) ϕ_B and how graphene influences these parameters. Therefore, volt-amperometric (I-V) measurements were carried out to study the Schottky diode. Curves were registered with a Keithley 4200 SCS at room temperature between -4 V and 4 V with a step of 0.1 V. The results are shown in Fig. 3.7 and Fig. 3.8, in linear and semi-logarithmic scale, respectively.

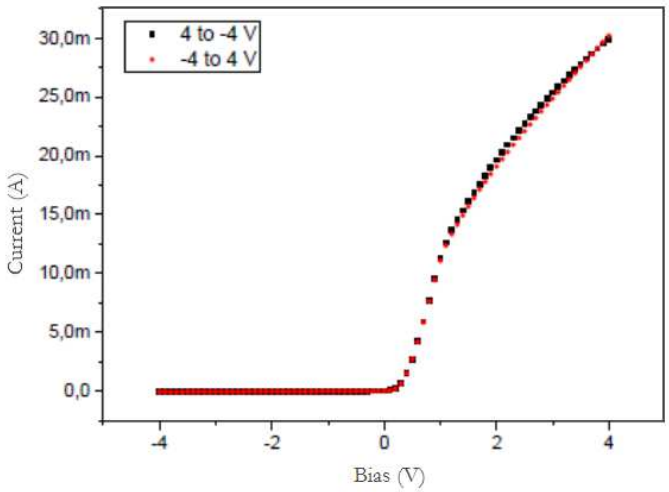

Fig. 3. 7 Current-voltage characteristic in linear scale.

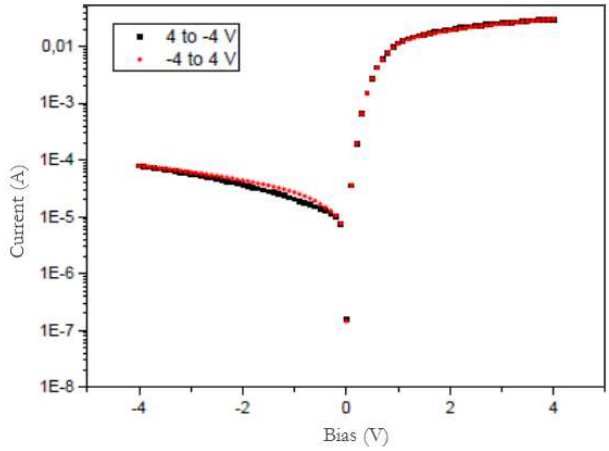

Fig. 3. 8 Current-voltage characteristic in semi-logarithmic scale.

It is clearly shown that graphene/Si interface forms a rectifying junction with a current ratio between direct and reverse polarization of about 200 at ±0.5 V. Moreover, it stands out that the rectifying behavior is maintained for about 2.5 decades, until the effect of the series resistance arises, deflecting the curve, for an applied voltage of about 0.8 V. Series resistance effect is also visible on the linear scale, where for the same voltage value the curve changes from an exponential to almost a straight line.

It is well known that I-V characteristic can be easily use to extract junction parameters. In fact, by fitting the theoretical I–V equation, series resistance and the other Schottky parameters, ideality factor and barrier height, can be calculated.

By considering the linear behavior in the semi-logarithmic scale and using the method of Cheung [14], it is possible to refer to the following equation:

$$\frac{dV}{d\ lnI} = R_S I + \frac{kT}{q}\eta \qquad (3.\ 2)$$

where I and V are the experimentally obtained data, k the Boltzmann constant, T the temperature and q the electron charge. The derivative was numerically calculated and the result is plotted versus the current. Finally the linear regression is carried out. The results are shown in Fig. 3.9, the data used were taken in a range from 0.2 V, able to satisfy the thermionic approximation criterion, and 0.7 V, limit value after which non ideality factors influence its form.

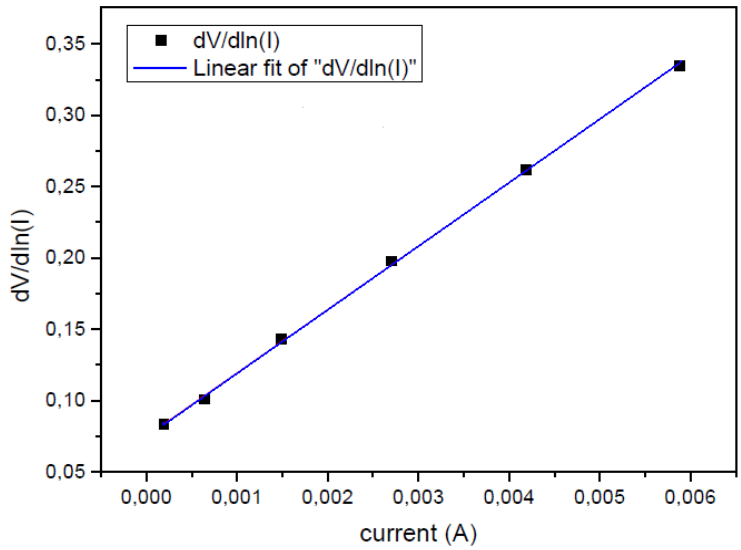

Fig. 3. 9 Linear regression of dV/d ln(I) plotted towards current I, used to extract the graphene/Si Schottky junction parameters.

The plot of Cheung shows an excellent linearity in this range with a correlation coefficient (R^2) of 0.99941; the extracted coefficients are the slope b=44.43±0.48 and the intercept a=0.075± 0.00155, from which R_s and ϕ_B values are obtained:

$$R_S = b = 44.43\ \Omega \qquad (3.\ 3)$$

$$\eta = \frac{qa}{kT} = \frac{0.075}{0.026} = 2.88 \qquad (3.\ 4)$$

being kT/q=0.026 V for T=300K.

For a Schottky diode, the ideality factor provides a good indication on the validity of the thermionic model: a factor close to 1 indicates an almost ideal device, where contributions due to charge recombination are negligible with respect to the thermionic one. As far as graphene/semiconductors diodes, values of n even larger than 5 at 300 K have been observed [123] and discussed in the frame of the thermionic model so that the value of n= 2.9 observed in the realized device, although suggesting an increasing relevant role of recombination effects, fully confirms, at the same time, the validity of the model used.

Even if the Fermi level of graphene, and thus the SBH, is dependent on the voltage, in forward bias the variation is very small (in this case 0.6 V) so the effects of voltage dependence are relatively small.

For the the SBH calculation equation 3.5 and 3.6 are used:

$$H(I)=V-\frac{kT}{q}\eta \ln\left(\frac{I}{AA^{*}T^{2}}\right) \tag{3. 5}$$

$$H(I)=R_S I+\eta\phi_B \tag{3. 6}$$

where, V and I are the experimental data, T=300 K is the temperature, A*=112 A/(cm^2 K^2) is the effective Richardson constant and A=0.16 cm^2 is the graphene/Si junction area. For calculations it is assumed that all the transferred graphene covered the silicon window and actually form the junction.

From the experimental I-V data, H function can be calculated and plotted versus I (Fig. 3.10).

The linear regression is carried out with the same range of values as before, showing again a great linearity value (R^2=0.9981). The extracted parameters are the slope a=43.8±0.85 and the intercept 1.89±0.002, that give an additional R_s and $\phi_B$values:

$$R_S=b=43.8\ \Omega \tag{3. 7}$$

$$\phi_B=\frac{a}{\eta}=\frac{1.89}{2.88}=0.65\ \text{V} \tag{3. 8}$$

where for ϕ_B calculation the value extracts from the plot of Cheung was used. It can be also noticed that R_s value is congruent with that obtained from the plot of Cheung, showing the goodness of the measures.

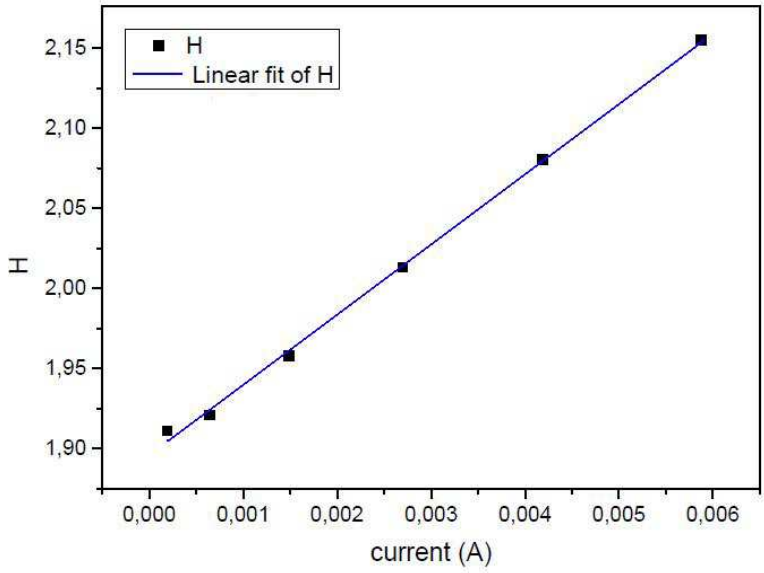

Fig. 3. 10 Linear regression of H function plotted towards current I used to extract the graphene/Schottky junction parameters.

The obtained results were in good agreement with those calculated in literature. In particular, the reported Schottky barrier heights vary from 0.4 to 0.8 eV [123, 124]. This large range of values is not contrasting since it is well known that the different production techniques (CVD, LPE etc) and transfer methods can induce doping in graphene. This results in a variation of the Fermi level and consequently of the SBH value too [8]. For instance, Chen et al. [123] studied graphene-silicon diodes with both n- and p-type silicon; SBH obtained from the I-V characteristic are 0.41 eV and 0.45 eV for n-Si and p-Si respectively, using junction areas in the order of tens of μm^2. Even Tongay et al. [124] characterized a graphene-semiconductor junction based on various semiconductor types and using conventional I-V measurement obtained a value of SBH equal to 0.86 eV for a silicon substrate.

Furthermore, the determination of SBH allows to extrapolate the graphene work function as:

$$\phi_G = \chi + \phi_B \qquad (3.\ 9)$$

Thus, by considering the just calculated ϕ_B value, 0.65 eV, and be known that the silicon electron affinity is χ=4.05 V: ϕ_G=4.70 V. This value is slightly larger than the accepted value for pristine graphene, when its Fermi level is located at the Dirac point, approximately equal to ϕ_G=4.6V [124]. It is worth noting that graphene work function depends on the bias, reflecting a SBH that varies in turn with the diode biasing [125, 126]. More specifically, this value corresponds to a lowering of the Fermi level E_F of around 0.1 eV reflecting a weak hole doping of the graphene in the forward bias region of the diode.

3.1.2 Gas sensing test

Graphene/Si Schottky diode was tested towards gaseous ammonia (NH_3) sensing. As known, NH_3 and nitrogen dioxide (NO_2) embody the typical model of reducing and oxidant gases, respectively, so that they are frequently used to study and eventually predict the behavior of similar species. Moreover, as already pointed out, ammonia is among the widespread gas whose detection is of manifold interest.

The Gas Sensor Characterization System (Kenosistec) used for the measurements consists of a stainless steel chamber of 40 cl volume made up of a fixed part and a mobile flange in which devices can be mounted and properly contacted with gold tips (Fig. 3.11). The fixed part of the chamber is connected with a gas system where a gas carrier, usually air or nitrogen, and various gas analytes are fluxed. A suitable electronic system (a DC generator and a Keithley 6485 picoamperometer) for measurements and a program for data acquisition, complete the experimental set-up.

Thanks to the dedicated software program, the experimental conditions, voltage, humidity, gas concentration and time can be set. A typical experimental test involves some fundamental steps.

Briefly, once the device is positioned inside the chamber and opportunely contacted (Fig. 3.12), a carrier gas flow is fluxed in order to stabilize the system and register a baseline.

Fig. 3. 11 Stainless steel chamber used for gas sensing test (Enea Portici Research Center).

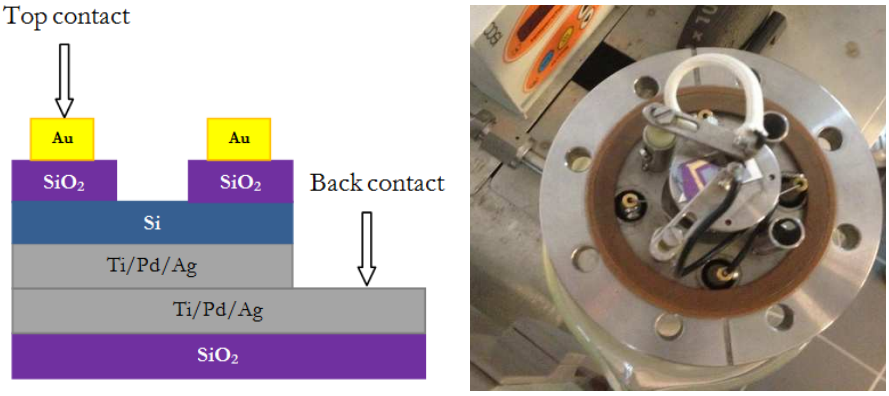

(a) (b)

Fig. 3. 12 (a) Schematic view of the graphene/silicon Schottky device contacted with the tips on the mobile flange of the stainless steel chamber (b).

Thereafter, under established humidity conditions, the device is exposed to a gas analyte for a preset time interval. Finally, the carrier gas is fluxed again into the chamber for a recovery process.

In the performed experiments, the response of the analyte to the gas target (ammonia NH_3) was obtained by reverse bias of the diode at -3V. Under this condition R_s effect was considered negligible.

Test results of repeated cycles, carried out in real environmental conditions, i.e. at room temperature of 295 K and in presence of Relative Humidity (RH) set at 50%, are reported for different NH_3 concentrations. In Fig. 3.13 the response of the device to a cyclic test of 200 minutes is shown.

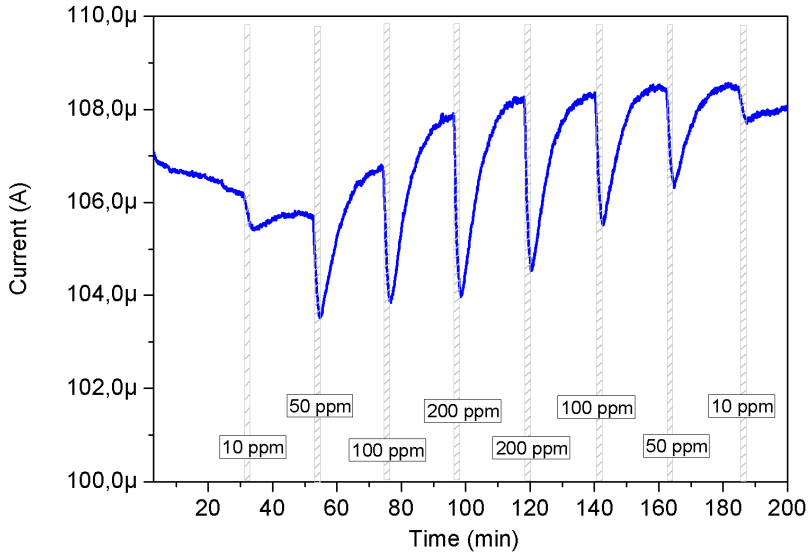

Fig. 3. 13 Current signal after several cycles upon 2 min of exposure (grey rectangles) to different NH_3 concentrations 10, 50, 100 and 200 ppm.

First, wet air is fluxed as carrier gas for 30 minutes in order to promote the stabilization of the system. Then, the analyte gas, NH_3, is fluxed into the test chamber for 2 minutes (grey rectangles in the graph) and alternated with the carrier gas, that is fluxed for 20 minutes between two consecutive measures for recovery purposes. Different analyte concentrations, namely 10, 50, 100 and 200 ppm were tested. Both the increasing and decreasing concentrations effect is evaluated.

Soon after switching on the gas injection, the device suddenly responds with a decrease of the current from the initial value I_0 till to a minimum I_{min}. Turning off the NH_3, the device spontaneously recovers to the initial value I_0. Current variations show a good repeatability between two repeated cycles at the same concentration, as evidenced in Fig. 3.14.

Low concentrations were further investigated. In Fig. 3.15 the results of repeated measurements at different NH_3 concentrations of 10, 20, 30 and 40 ppm are reported. After a baseline in wet air, the gas is fluxed into the test chamber and as soon as it is injected, the device suddenly responds with a decrease of the current. Ammonia flow is kept constant for a longer time than before, 10 minutes, until a stable condition is achieved. Finally, after turning off the NH_3, roughly in 10 minutes the device spontaneously recovers to the initial value.

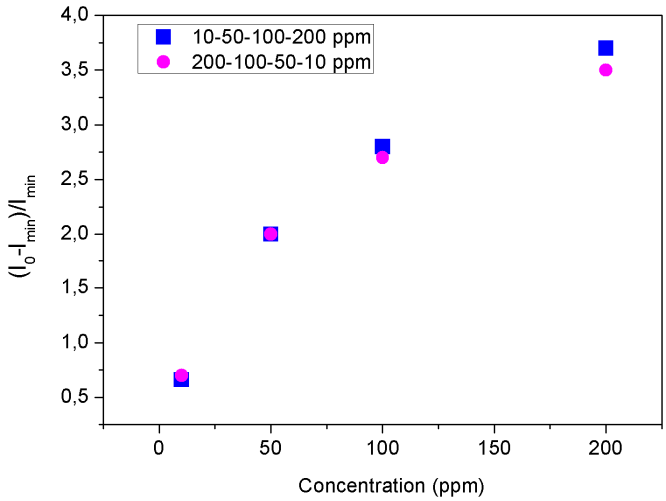

Fig. 3. 14 Current variation due to ammonia sensing for the increasing (10-50-100-200 ppm) and decreasing (200-100-50-10 ppm) concentration cycles.

Ammonia alters the device current even at small concentrations as low as 10 ppm. Furthermore, the sensor shows a spontaneous restoration that is reached in about 10 min after switching off the inlet of the gas, without the need to resort to recovering techniques, such as thermal annealing or exposure to UV radiation [43]. This, in turn, suggests that the device can be reliably used to detect very small ammonia concentrations in real environments.

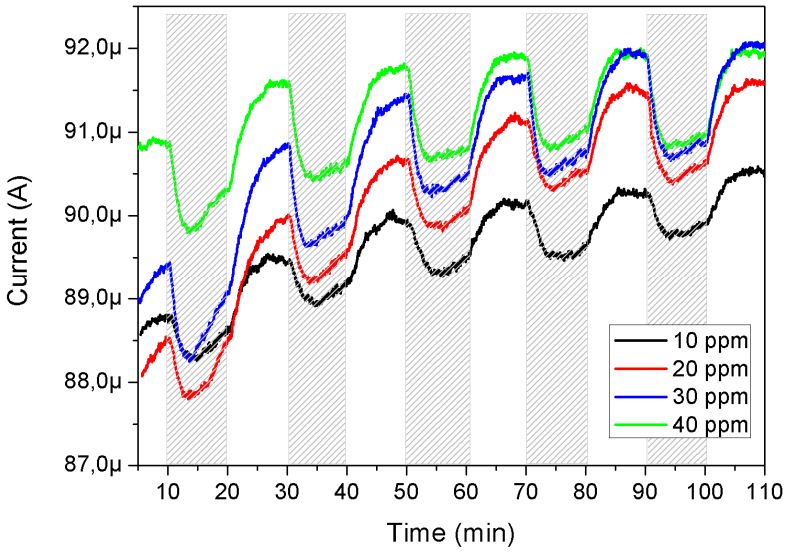

Fig. 3. 15 Device response at low NH_3 concentrations (10, 20,30 and 40 ppm). The diode is reverse biased at -3 V, T=295 K and RH=50%.

A clear correlation between the response intensity (i.e. conductance relative change), and the analyte concentration can be extrapolated. It is known that exposure causes a charge transfer between graphene and NH_3, inducing a change in the number of carriers, which in turn depends on the analyte concentration. When analyte interacts with the graphene-based heterojunction, there is a modulation of the Schottky barrier height, increasing or decreasing according to the analyte type [8]. In particular, being ammonia an electron donor type, the barrier height decreases as schematically depicted in Fig.3.16.

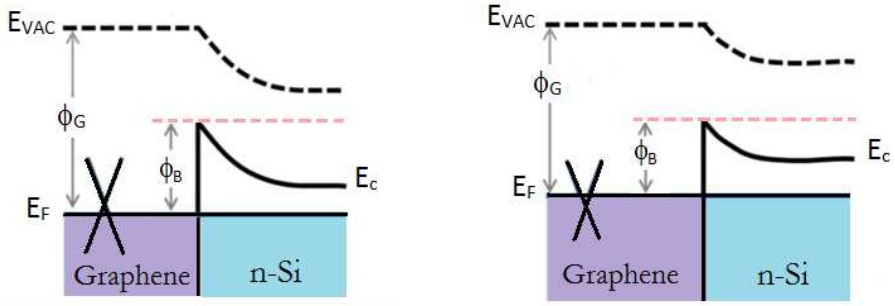

Fig. 3. 16 Schematic band diagram of the graphene/n-Si interface with (a) pristine condition and (b) electron donor case (ammonia). E_{VAC}, E_C, ϕ_G, and ϕ_B indicate the vacuum energy, conduction band, graphene work function, and Schottky barrier height, respectively.

It is therefore possible to derive a relation between the variation of the Fermi level in graphene and the analyte concentration (Fig. 3.17).

Preliminarily, the barrier height value is estimated at -3V. As previously mentioned, the Fermi level in the graphene/Si junction, and thus the SBH, is dependent on the voltage, even if variations are very small in forward bias. Anyway, the exact value of the SBH at -3V was calculated using the I_s measured at that voltage value:

$$\phi_{B(-3V)} = \frac{kT}{q} \ln\left(\frac{I_s}{AA^{*}T^2}\right) = 0.58 \text{ V} \qquad (3.\ 10)$$

This SBH provides a value for the graphene work function equal to ϕ_G=4,63 V. It shows that when the diode is reversed biased at -3 V graphene can be considered pristine or lightly n-type doped.

When the diode is exposed to NH_3 concentration a minimum current value is measured:

$$I_{min}=AA^{*}\exp\left(-q\frac{\phi_{B(-3V)}-\Delta\phi_{NH_3}}{kT}\right) \qquad (3.\ 11)$$

where $\Delta\phi_{NH_3}$ is the variation of SBH due to ammonia exposure. Considering now the variation of SBH $\Delta q\phi_{NH_3}$ expressed in eV and combining the last two equations, it is possible to obtain the variation of the Fermi level:

$$\Delta E_F=\Delta q\phi_{NH_3}=kT\ln\left(\frac{I_{min}}{I_S}\right) \qquad (3.\ 12)$$

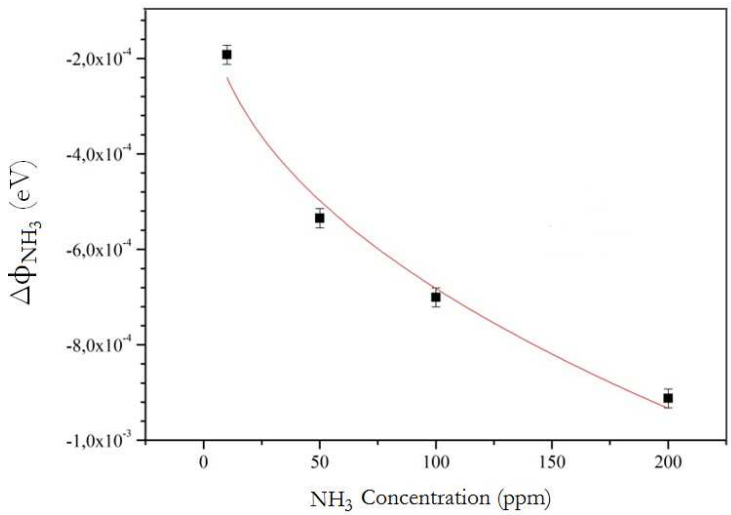

Fig. 3. 17 SBH variations versus NH_3 concentration in the range 10-200 ppm (T=295 K and RH=50%).

The SBH decrease was registered for each different ammonia concentration, showing that a major concentration results in a smallest SBH. In Table 3.1 the maximum and minimum current signals for a given NH_3 concentrations are reported together with the corresponding Fermi level variation.

Theoretical findings are in accordance with provided experimental trend. Furthermore the device response shows a good repeatability, comparing different measurements, with the same analyte concentration.

Table 3.1 Current signals and Fermi level shift versus NH_3 concentration at 295K and RH=50%.

NH_3 concentration (ppm)	I_0 (μA)	I_{min} (μA)	ΔE_F (eV)
10	106.2	105.4	-1.9E-4
50	105.7	103.5	-5.3E-4
100	106.7	103.8	-7.1E-4
200	107.8	104.0	-9.1E-4

Numerous twin devices were realized and tested in the same conditions. Measures have been periodically repeated after one weak and one month, showing comparable results in ammonia detection. For instance, the previously reported measure of Fig. 3.13 is here reported together with a second curve representing a measure carried out a month later (Fig. 3.18).

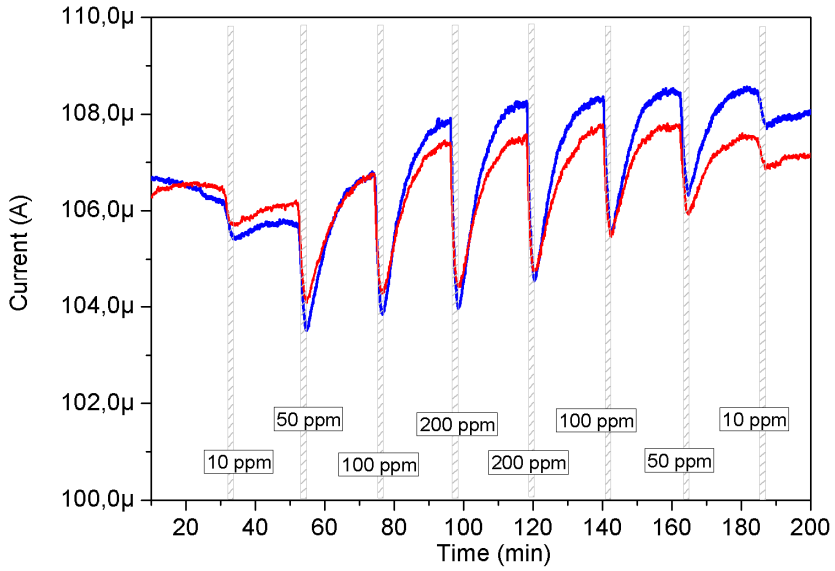

Fig. 3. 18 Current signal after several cycles upon 2 min of exposure (grey rectangles) to different NH_3 concentrations 10, 50, 100 and 200 ppm (blu curve) and current signal registered a month later under the same experimental conditions (red curve).

The selectivity of these devices was also proved by performing the same sensing tests towards other different analytes, as NO_2 and CO_2. Actually, no appreciable modifications in the sensor response could be detected.

Therefore, an innovative application of graphene-based Schottky diode have been successfully tested. It should be highlighted that a remarkable current variation of the device at very low ammonia concentration was obtained operating in real environmental conditions and at room temperature.

Indeed, even if similar devices have been reported in the literature, none of them was based on LPE graphene, as in this case, and no one was able to detect such low ammonia concentrations. In literature devices, graphene was prepared by chemical vapor deposition and showed the ability to detect NH_3 in the range of few percent in dry environment only [127, 128].

3.2 CNT/TiO_2/Pt metal oxide gas sensor

Several fabrication methods have been reported in the production of metal oxide semiconductor sensors and many factors, such as sensible material, gas target and cost, should be considered in order to choose the best technique. In this case, metal oxide gas sensor devices were fabricated by means of a simple technique. Briefly, an aqueous paste of the CNT/TiO_2/Pt nanohybrid composite previously described in Chapter 2, was prepared allowing for the subsequent deposition by painting of a thick film of the paste on a ceramic substrate. This consist of alumina, 6×3 mm^2 sized, supplied with comb-like Pt-electrodes in front and a Pt-heater on the back, as shown in Fig. 3.19 a. The complete device with the deposited sensible material is showed in Fig 3.19 b.

Fig. 3. 19 (a) Ceramic substrate provided with comb-like Pt-electrodes in front and a Pt-heater on the back; (b) CNT/TiO_2/Pt sample deposited on the ceramic substrate.

Sensing tests were carried out in the "Sensors Laboratory" of the University of Messina (DIIECI). A dedicated apparatus was composed of a stainless steel box, where the sensor was allocated (Fig. 3.20), connected to a Bronkhorst E700 gas controller and an Agilent E3632A power supply. Such an apparatus was interfaced with a personal computer, which allowed to set and control the working temperature, and to measure the resistance values of the sensors by means of an Agilent 34970A multimeter.

Before carrying out the sensing tests, sensors were pre-treated in air, in order to stabilize the system and register a baseline. Then the sensor was maintained under hydrogen (H_2)/air mixtures flow (100 ml/min), keeping H_2 concentrations beyond the lower explosive limit (around 4%).

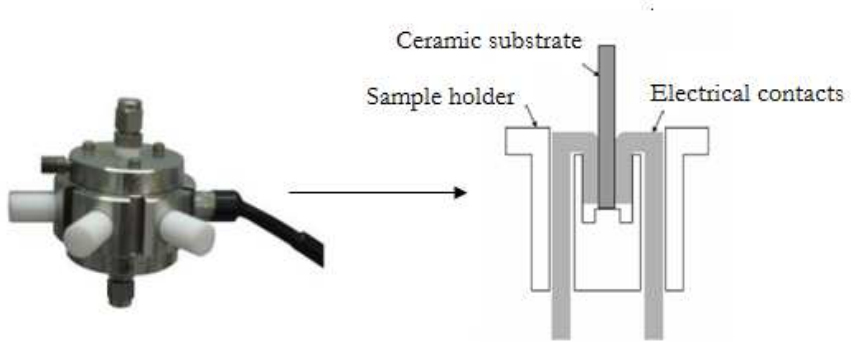

Fig. 3. 20 Stainless steel box and detail of the sample holder.

Tests were performed at different gas concentrations (H_2 0-4 %). The sensor response was given by $100 \cdot [(R–R_0)/R_0]$, where R_0 and R are the resistances measured under gas carrier (baseline) and analyte/carrier flow, respectively.

As described in detail in Chapter 2, two different CNT/TiO_2/Pt hybrid materials, ME-1P and ME-2P, were realized by few modifications of the micro-emulsion synthesis process and tested for hydrogen monitoring in air. As discussed, samples showed different morphological and structural characteristics. In order to link such modifications to their gas sensing performances, they were both tested towards gas sensing in the same experimental conditions.

Hydrogen sensors are of increasing importance due to the development and expanded use of H_2 gas as an energy carrier. As H_2 forms explosive atmospheres with air (the lower explosive level is 4% of H_2 in air), the

development of H_2 leak sensors is of great importance. Moreover, these sensors should also be able to detect hydrogen at temperatures as low as possible, near room temperature, so to reduce considerably the power consumption of the sensing devices. As already reported [22] the sensor response is found to increase with increasing operating temperature. Therefore sensors were tested from 25°C up to 200°C. In order to appreciate a clear response at the lowest possible temperature, 100°C was chosen as the operating temperature of the sensors.

Fig. 3.21 displays the results of the hydrogen sensing tests. ME-1P and ME-2P sensors responses are compared towards low H_2 concentrations. A good linearity is obtained in the explored concentration range and very slight differences are detected for the two samples.

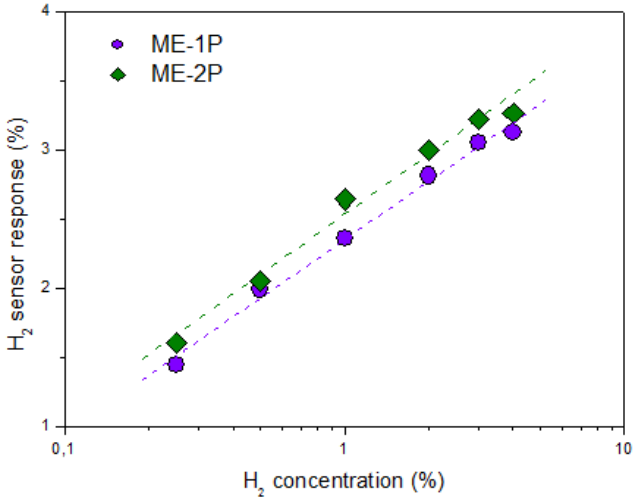

Fig. 3. 21 Results of sensing test carried out at 100°C.

Responses are comparable to each other but more interestingly are also better to those previously recorded using CNT/TiO_2/Pt nanohybrids prepared by sol-gel technique [129]. Indeed, a similar response was obtained under the same concentrations of H_2 in air, but measurement had been carried out at higher operating temperature conditions (150°C). As already pointed out [23], formation of the more active anatase phase of the oxide, good surface contact and interfacial CNT/TiO_2 interaction are beneficial for the sensor responsiveness. Thus, it is not surprising that samples ME-1P and ME-2P behave similarly because of the balance of competing effects. In sample ME-1P the formation of larger titania agglomerates, resulting in

diminished surface contact and weaker interaction with the nanotubes, reduces positive effects deriving from the formation of anatase phase. Oppositely, in sample ME-2P the formation of rutile partly limits benefits associated to the presence of smaller TiO_2 agglomerates highly dispersed-on and strongly interacting-with the CNT.

Therefore, conductometric sensing of low concentration of hydrogen in air by means of the synthesized materials appeared to be little influenced by the different morphological and structural features, when prepared within the same method. Indeed, it should be highlighted the effect of the different synthesis method with respect to the previously used SG technique, able to provide great improvement in the sensors performance. This in turn proves the importance of the synthesis techniques in tailoring materials features and devices characteristics.

However, it should be also pointed out the prominent role of the synergic action among all the components of the nanohybrids.

The working mechanism of the CNT/TiO_2/Pt based sensor has been previously attributed to the synergistic action of the three components (CNT, TiO_2 and Pt) of the nanohybrids. It has been explained in terms of quenching of the CNT conductance following the oxide mediated electron transfer from the metal. In particular, it has been hypothesized [23] that a Schottky barrier forms at the interface platinum/oxide owing to the electron transfer from TiO_2 to Pt due to the higher value of the work function of the metal, ϕ_{Pt} = 5.4 eV, with respect to the electron affinity of TiO_2, χ_{TiO2} = 4.3 eV. In addition a n-/p-type hetero-junction can be assumed to form at the interface oxide/nanotubes, being χ_{CNTs} = 4.8 eV (Fig. 3.22 a, b).

Platinum acts as a catalyst promoting the dissociation of the H_2 molecules that diffuse into the metallic matrix, according to a spill-over mechanism, hence lowering the work function of platinum, as sketched in Fig. 3.22 c. Activated hydrogen species then chemisorbed onto the TiO_2 surface acting as surface donors, with consequent e^- transfer to the titania conduction band. The relative position of the CNT and TiO_2 conduction band edge [23] allows for the transfer to the graphitic network of the electrons injected into the oxide. Such a process finally brings about a

reduction of the hole concentration in the CNT, thus causing the electrical resistance of the nanocomposite to increase.

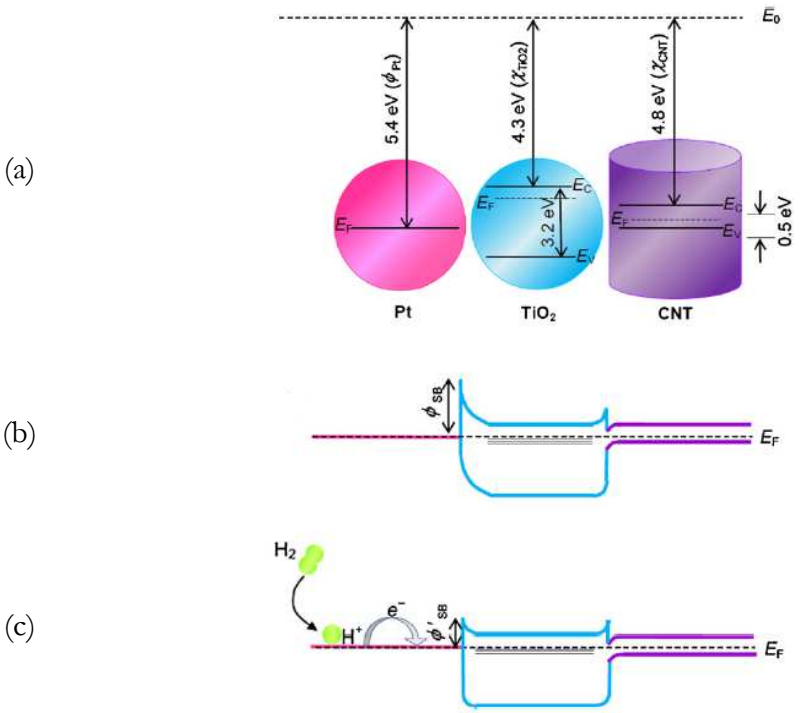

Fig. 3.22 Qualitative band diagrams of (a) Pt, TiO_2 (large gap n-type semiconductor) and CNTs (p-type semiconductor), and (b) Pt/TiO_2/CNTs nanocomposites. (c) Sketch of the charge transfer from H_2 accounting for the sensing mechanism [23].

However, the electronic mechanism of CNT, TiO_2 and Pt interaction is still investigated to further improve the sensing of this devices.

Interestingly, the same devices were even tested towards other different gas analytes such as CO_2 and NH_3 but no significant changes in resistance response was detected, thus proving their high selectivity.

3.3 CNT/TiO_2/Pt electrochemical sensor

Electrochemical measurements were also performed at the "Sensors Laboratory" of the University of Messina (DIIECI). To this purpose a Dropsens μStat 400 potentiostat able to work with planar sensors consisting of three electrodes, namely a carbon screen-printed working electrode (4 mm diameter), a carbon auxiliary electrode and a silver pseudo-reference

electrode, was used. The structure of the commercial sensor is shown in Fig. 3.23.

Fig. 3. 23 Planar sensor consisting of three electrodes: carbon screen-printed working electrode, carbon auxiliary electrode and silver pseudo-reference electrode equipped with insulating cover and substrate.

The sensing material was synthesized as shown in the previous Chapter 2. The nanohybrids already tested as metal oxide semiconductor gas sensors were further investigate in the electrochemical field [111], proving their versatility. Water suspensions of CNT/TiO_2/Pt nanomaterials were mixed with Nafion (5 wt%) in order to confer mechanical stability to the sensible material, as well as to provide an appropriate ionic conductivity. The solutions were sonicated for 15 min in order to obtain a homogeneous dispersion. The suspensions were then printed on the working electrode (small black circle) and the printed films were allowed to dry at room temperature. The typical realized sensor is shown in Fig. 3.24.

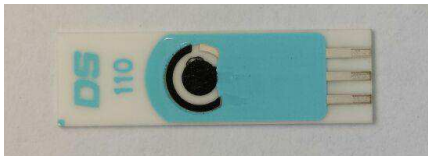

Fig. 3. 24 CNT/TiO_2/Pt hybrid deposited on a commercial electrode.

3.3.1 Electrochemical sensing tests

Cyclic voltammetry (CV), linear sweep voltammetry (LSV) and chrono-amperometry were used to test the so-fabricated sensors towards hydrogen peroxide sensing (H_2O_2). As first discussed, hydrogen peroxide plays an important role in many biological processes and, thus, it is broadly investigated in biology, food production and environment monitoring [130].

CV tests were carried out at different scan rates (50–250 mV/s) in the range of potentials between –0.2 V and 0.8 V, in the presence of different concentrations (0–4660 μM) of hydrogen peroxide in pH 7.4 phosphate buffer solution (PBS).

The most representative cyclic voltammograms measured in the presence of 2 mM H_2O_2 in PBS solution are shown in Fig. 3.25. In order to understand the role of the single components, the Pt loaded anatase-TiO_2 reference sample (ME-0P) and anatase/CNT nanohybrid (ME-1) were firstly considered. ME-0P exhibits the lowest electrocatalytic activity, occurring on the metal particles thanks to their high reactivity toward this species. However, the low electrical conductivity of TiO_2, slowing the electron transfer, severely limits the reaction. Instead, in the case of ME-1 no relevant peak is observed in the investigated range of potential (Fig. 3.25 a).

Carbon nanotubes/Pt effect have also been investigated and deepened by the comparison with different other carbon nanostructures [110].

As for the two three-phase hybrids (ME-1P and ME-2P), the cyclic voltammogram, (Fig. 3.25 b) of sample ME-1P looks very similar to that of the unloaded sample (ME-1). The only difference is represented by an increase of the anodic current, probably due to the electro-catalytic effect of the Pt toward H_2O_2.

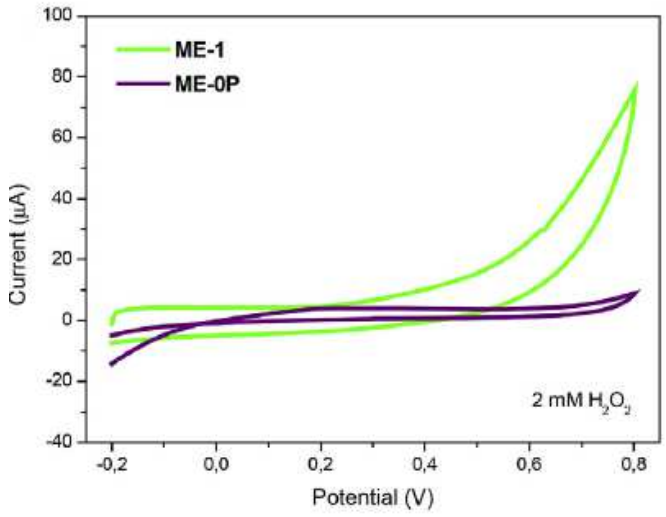

(a)

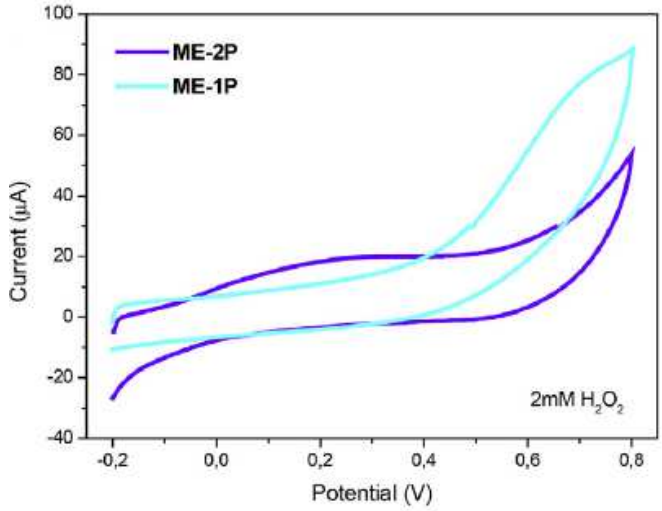

(b)

Fig. 3. 25 Cyclic voltammograms measured in the presence of 2 mM H_2O_2 in PBS solution for (a) ME-1/ME-0P and (b) ME-1P and ME-2P samples (scan rate:100 V/s).

The voltammogram of sample ME-2P is completely different; an oxidation peak is clearly observable at a potential of 0.3 V. First of all, the lower oxidation over-potential shown by the sample ME-2P is not attributable to the presence of defects (and, in particular, of sp^2 defects) on CNT since the density of sp^2 defects, as monitored by the Raman I_D/I_G intensity ratio, in sample ME-1P is significantly higher than in sample ME-2P. This result is in full agreement with previous reports, which showed that the presence of defects on the CNT has little influence on the electro-chemical interaction between them and H_2O_2 [131]. Rather, the diverse morphology of the two samples can account for their different electrochemical behaviour. As previously discussed, nanohybrid ME-1P is featured by large TiO_2 agglomerates and bad dispersion on nanotubes; oppositely, in sample ME-2P the smaller-sized titania agglomerates are homogeneously dispersed over the CNT mat. In turn, this reflects on different degrees of dispersion of the Pt on the TiO_2 phase. Moreover, the different average size of Pt nanoparticles (larger in ME-1P and smaller in ME-2P), results in different exposed surface for the interaction of the metal catalyst with H_2O_2.

On the basis of the obtained results, it can be assumed that the oxidation of H_2O_2 at potential lower than 0.3 V is due to the presence of platinum nanoparticles that act as catalysts favouring the redox reaction. The

presence of smaller sized and better dispersed Pt nanoparticles plays a key role in the sensing mechanism of the H_2O_2 improving the sensitivity and, at the same time, reducing the over-potential. Moreover, the presence of CNT, increasing the conductivity of the nanocomposite, allows the rapid electron transfer to the surface of the electrode.

Likely, titania is not directly involved in the process of sensing, but has the only role to facilitate the dispersion of the platinum within the composite nanostructure. Thus, the good electrochemical behaviour shown by ME-2P toward H_2O_2 oxidation arises from the synergistic action of the three components phases, the smaller size and the homogeneous distribution of the metal nanoparticles.

The linear sweep voltammetry patterns obtained with sample ME-2P is shown in Fig. 3.26. At fixed scan rate (Fig. 3.26 a), the anodic peak current (iP) increases linearly (inset of Fig. 3.26 a) with H_2O_2 concentration (c) in PBS solution, as described by the equation iP(μA) = 3.67 c(mM) + 12.63, with a correlation coefficient (R^2) of 0.995. At fixed H_2O_2 concentration (Fig. 3.26 b), the anodic peak current exhibits a linear dependence (inset Fig. 3.26 b) on the square root of scan rate (v), namely iP(μA) = 2.66 v1/2(mV1/2/s1/2) – 7.67 (with R^2=0.992). The latter result indicates that the electrochemical kinetics is controlled by diffusion of H_2O_2.

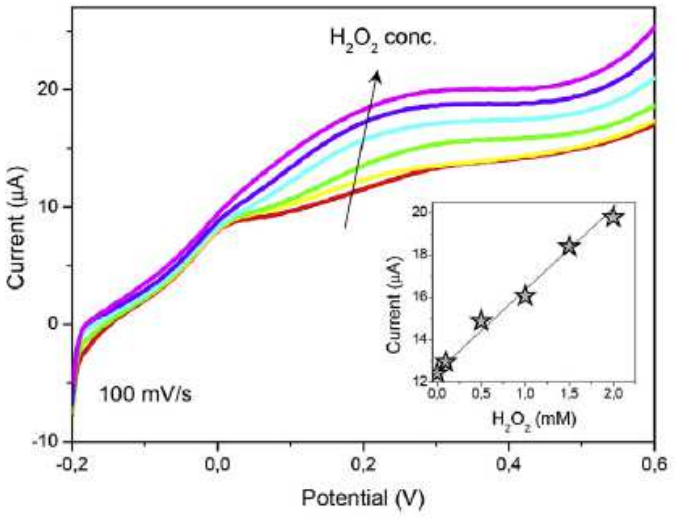

(a)

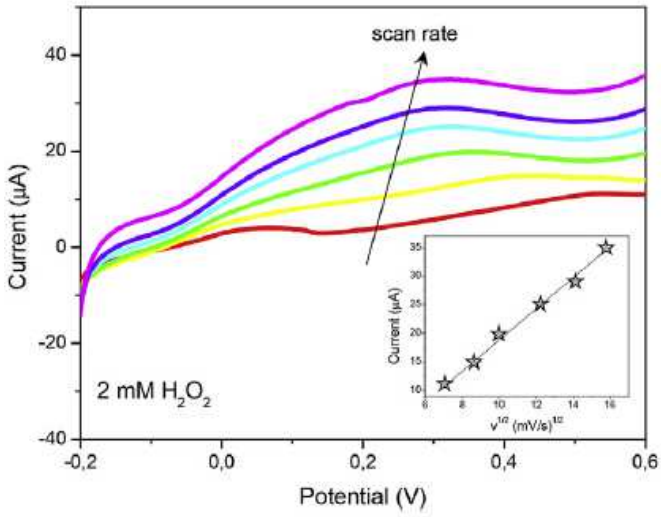

(b)

Fig. 3. 26 (a) Linear sweep voltammetry patterns in the presence of different concentrations of H_2O_2 in PBS solution (scan rate: 100 mV/s). Inset shows anodic peak current as function of H_2O_2 concentration. (b) LSV patterns in the presence of 2 mM H_2O_2 in PBS solution at different scan rates. Inset shows anodic peak current as function of the square root of scan rate.

Current responses obtained, at applied potential of 0.3 V, for samples ME-2P, ME-0P and ME-1 with different concentrations of H_2O_2 in PBS is displayed in Fig. 3.27. At any concentration the electro-catalytic activity increases in the order ME-1 < ME-0P < ME-2P, in accordance with the results of CV analysis.

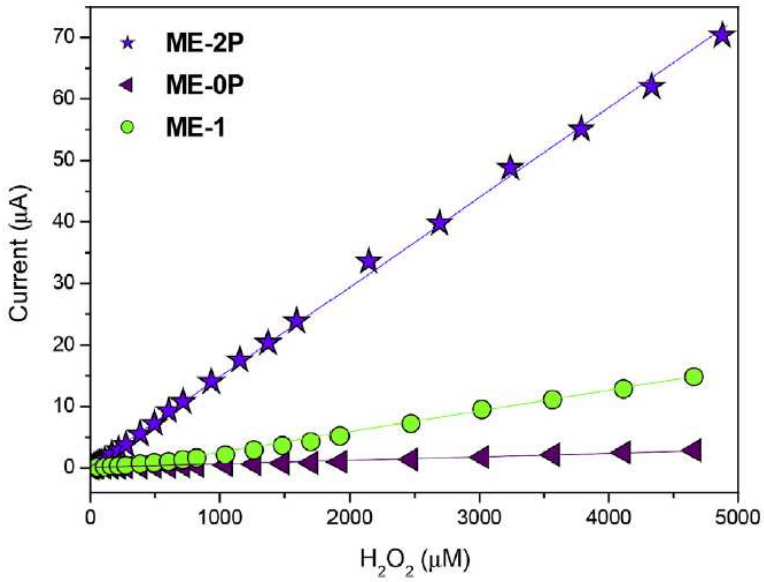

Fig. 3. 27 Current responses measured at 0.3 V applied potential for different concentrations of H_2O_2 in PBS.

Chrono-amperometric curves were obtained recording the oxidation current at fixed potential, while an appropriate volume of H_2O_2 solution was added into the PBS maintained under magnetic stirring conditions. Figure 3.28 a displays the chrono-amperometric response obtained for sample ME-2P, at applied potential of 0.3 V, for addition of different concentrations of H_2O_2 in stirred PBS solution. The relative calibration curves are shown in Figs. 3.28 b and 3.28 c. The current signal increases very fast when H_2O_2 is dropped in solution in a time less than 3 s. The current increases linearly with H_2O_2 concentration. In the range 0–70 μM the increase follows the law iP(μA) = 0.009 c(μM) + 0.001 (R^2 = 0.999); in the range 0.08–5 mM it is described by the equation iP(μA) = 0.0145 c(mM) + 0.28 (R^2 = 0.999). The sensitivity correspondingly calculated is 74 and 120 μA $mM^{-1}cm^{-2}$ in the two ranges, respectively.

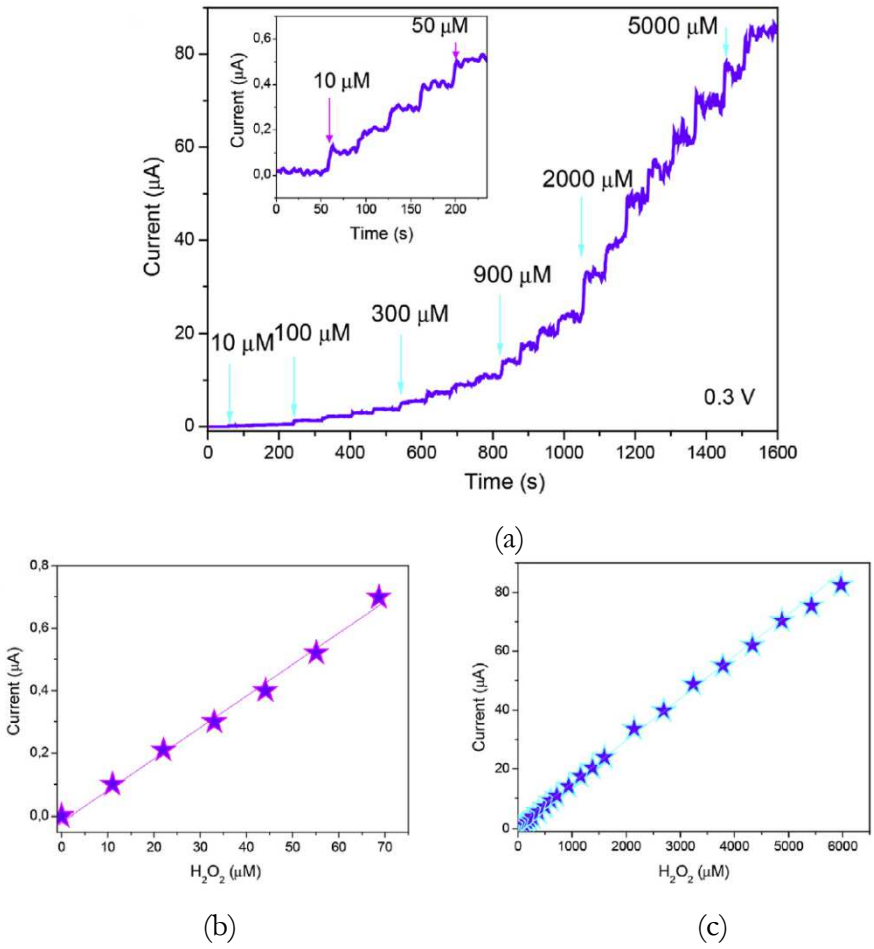

Fig. 3. 28 (a) Chrono-amperometric response for addition of different amounts of H_2O_2 at applied potential of 0.3 V and relative calibration curves at (b) low and (c) high concentrations.

The detection limit is evaluated to be 5 µM for a signal to noise ratio of 3. Reproducibility was estimated from the response to 0.1 mM H_2O_2 for nine different acquisitions and an acceptable RSD of 2.58% was obtained.

The selectivity of the ME-2P based sensor was also examined by recording the responses towards some of the most common substances that are present in biological and environmental samples and could cause interferences during electrochemical determination of the target analyte [132].

Fig. 3.29 shows the chrono-amperometric response to an addition of 0.1 mM H_2O_2, different salt and biomolecules in PBS solution.

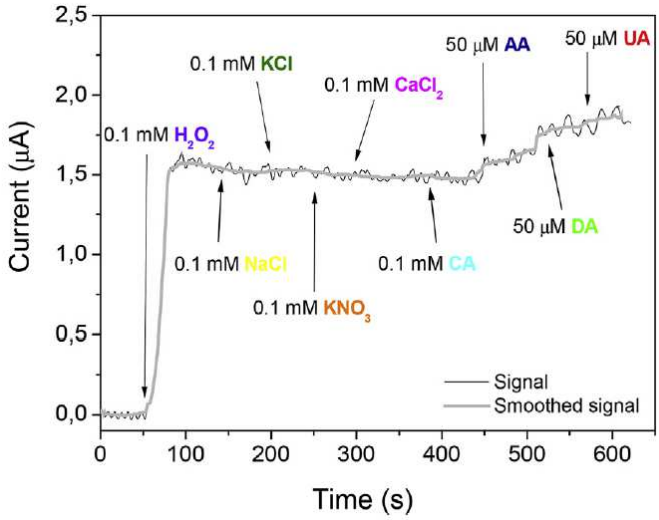

Fig. 3. 29 Chrono-amperometric response at applied potential of 0.3 V for addition of different interfering species in stirred PBS solution.

A clear and fast increase of the current is observed when H_2O_2 is added, no significant response is observed instead for 0.1 mM of NaCl, KCl, KNO_3, $CaCl_2$ salts, also no response is shown for the same concentration of citric acid (CA). As regards the biomolecules ascorbic acid (AA), dopamine (DA) and uric acid (UA), no significant interference is observed for concentrations up to 5 µM. However, for a concentration of 50 µM the current responses compared to 0.1 mM H_2O_2 are estimated to be 5, 8 and 9% for UA, AA and DA respectively. Very few works are found in the literature about the detection of H_2O_2 with CNT/TiO_2/Pt composite electrodes [133, 134]. These sensors provide sensitive detection of H_2O_2 in both anodic and cathodic regions. However, in the negative potential range, the sensors may

suffer from the instability of the amperometric responses, due to the interferences by oxygen of air. Comparing their performances in the anodic region (Table 3.2), it can be noted that detection limit of the present sensor is high compared to other H_2O_2 sensor devices using CNT/TiO_2/Pt -modified electrodes. On this purpose, it is worthwhile noticing that disposable screen printed carbon electrodes, like that here utilized, have more practical advantages (such as low costs) and are more suitable for on field, portable electrochemical instrumentation, but on the other hand, their use could produce more noise than a conventional three electrodes cell, thus resulting in high detection limit, as obtained. As shown, the realized sensor is able to work at lower potential (0.3 V). This is of obvious advantage because it limits the interfering of other oxidizable species and provides a much wider linear dynamic range. What is more, the composite electro-catalytic material results simpler and cheaper to be prepared with respect to previous materials, which are based on SWCNTs and TiO_2 nanotubes.

Table 3.2 Comparison of the electro-analytical characteristics of different Pt/TiO_2/CNT-modified electrodes.

	Pt/TiO_2/SWCNT [134]	**TiO_2/CNT/Pt** [133]	**fCNT/TiO_2/Pt** This work [111]
Sensitivity ($\mu AmM^{-1}\ cm^{-2}$)	571.7	240	120
Detection limit (μM)	0.73	1	5
Potential (V)	0.7	0.4	0.3
Linear range (mM)	0 –1.5	0 – 2	0 – 6

In conclusion, this time the differences in material synthesis played a key role in differentiating the sensing behaviour of the samples. It appeared that when smaller titania and Pt particles were obtained, better electrochemical properties were registered. A suitable device for hydrogen peroxide sensing in terms of fabrication simplicity, fast response, reliability, repeatability and low cost was realized. Furthermore important is that a great selectivity was also proved.

4
Physical Sensors

Physical sensors are devices able to measure a physical quantity, as for example light, strain, pressure, temperature, magnetic field, etc., and convert it to a signal which can be easily read. Due to the variety of applications many different kinds of physical sensors are continuously being developed.

Among the huge family of physical sensors the optical ones have been considered. In particular, in this chapter, the main physical and electrical concepts at the root of the operation of photodetectors will be reviewed.

4.1 Introduction

A rough classification of sensors can be based on their operating mechanism, whether it involves chemical or physical principles. Basically, a physical sensor is a device that provides information about a physical property of the system. It is able to measure a physical quantity, as for example light, strain, pressure, temperature, magnetic field, etc., and to convert it into a signal which can be easily read and used by other devices. Nowadays, there are many kinds of physical sensors available and due to the variety of applications, it is quite hard to take account of all the existent typologies. In addition, novel methods and materials, enabling more advanced sensing devices, are continuously being developed.

Among this huge family of sensors the optical ones have been considered. An optical sensor is a device that converts electromagnetic radiation , the measured physical quantities, into electronic signals, able to be read by a proper instrument. Optical sensors are used in numerous applications such as for quality and process control, medical technologies, imaging, remote sensing, etc. .

The basic optical devices able to convert infrared, visible or ultraviolet light to electric signals, are known as photodetectors.

Nowadays, the development and the fabrication of photo-detectors is becoming increasingly important, because of their wide use [135]. In particular, among the variety of photo-detectors, particularly useful are those operating in the ultraviolet (UV) range, from the visible (400 nm, 3.1 eV) down to X-rays (10 nm, 124 eV) [136]. To this regard, the most challenging applications of UV radiation detection are related for example to medical imaging [137], disinfection and decontamination [138], space observation [139], control and safety [140]. The many scientific and industrial applications of these devices continuously demand for high performing characteristics. High sensitivity is among the most important features, any quantum efficiency loss or recombination of photo-generated carriers in the detector should be prevented. Time stability of the performance is also required; the detector should offer long-term radiation hardness and be able to operate reliably under special conditions. At the same time, durability in harsh environments should also be an essential characteristic to prevent electrical/optical performance decline.

In this scenario, materials play a crucial role being able to tailor devices characteristic. Among these, wide band gap semiconductors as silicon carbide (SiC) are largely used. SiC, especially in its 4H hexagonal structure, has been reported to be a promising semiconductor material being endowed with outstanding properties [141]. Compared to other semiconductors, 4H-SiC allows the production of UV photodetectors with a very low dark current, significantly higher operating temperature and blindness to visible/IR background. Previous studies reported SiC-based UV photodetectors focused on different electronic structures and SiC polytypes, such as 6H-SiC [142] and 3C-SiC [143]. UV photodiodes based on 4H-SiC have also been reported and mainly based on p-n, Schottky, avalanche and mesa-type p-i-n diodes [144, 145, 140].

In this work, a p-i-n photodiode based on 4H silicon carbide was studied and addressed to the specific realization of a UV flame detector. In the following, photo-detector operating principles and its characterization will be first introduced.

4.2 Operating principle of photodetector

Photodetectors are basically semiconductor devices able to convert optical signals into electrical ones.

Their characteristics and operating principles can be understood starting from the simplest photodetector, the so-called photoconductor. It consists simply of a slab of semiconductor, of length L, width W and thickness D, with two ohmic contacts on the opposite ends, as shown in Fig.4.1.

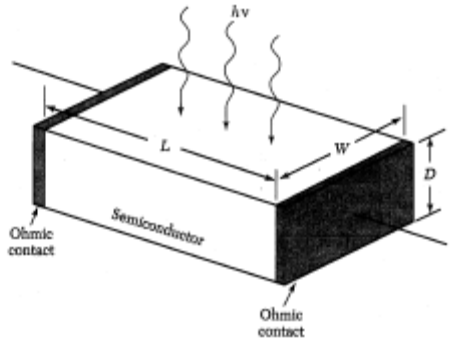

Fig. 4. 1 Geometry of the semiconductor slab of length L, width W, and thickness D.

When its surface is illuminated with incident light ($h\nu > E_g$, with E_g energy gap of the semiconductor) electron-hole pairs are generated either by band-to-band transition (intrinsic) or by transitions involving forbidden-gap energy levels (extrinsic), resulting in an increase in conductivity.

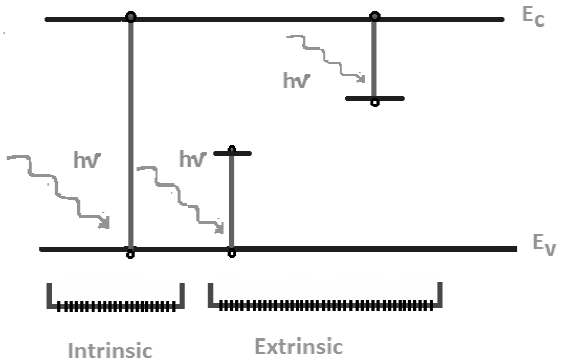

Fig. 4. 2 Process of intrinsic and extrinsic photo-excitation.

For the intrinsic photoconductor, the conductivity is given by:

$$\sigma = q\left(\mu_n n + \mu_p p\right) \tag{4. 1}$$

where q is the electric charge, n and p are electron and hole concentrations respectively, μ_n is the electron mobility and μ_p is the hole mobility. An increase in conductivity under illumination is mainly due to the increase in the number of carriers.

A necessary condition have to be imposed on the wavelength of the incident light. Indeed, just for wavelengths shorter than the cut-off wavelength λ_c, corresponding to the semiconductor band gap E_g the incident radiation is absorbed by the semiconductor and there is a consequent generation of hole-electron pairs. The long-wavelength cut-off for an intrinsic photoconductor is given by:

$$\lambda_c(\mu m) = \frac{hc}{E_g} = \frac{1.24}{E_g(eV)} \tag{4. 2}$$

For the extrinsic photoconductor, photoexcitation may occur between the band edge and an energy level in the energy gap. In this case, the long-wavelength cut-off is determined by the depth of the trap/defect level within the forbidden gap.

The principle of operation of a photoconductor under illumination assumes that at time t=0, the number of carriers generated in a unit volume by a given photon flux is n_0. At a later time t, the number of carriers n(t) in the same volume decays by recombination as:

$$n = n_0 e^{-t/\tau} \tag{4. 3}$$

where $1/\tau$ is the recombination rate.

Considering a steady flow of photons impinging uniformly on the surface of a photoconductor with an area A = WL, the total number of photons per unit time arriving at the surface is $(P_{opt}/h\upsilon)$, where P_{opt} is the incident optical power and $h\upsilon$ is the photon energy. At steady state, the carrier generation rate G must be equal to the recombination rate. If the detector

thickness D is much larger than the light penetration depth $1/\alpha$, the total steady-state carrier generation rate per unit volume is given by equation (4.4):

$$G=\frac{n}{\tau}=\frac{\eta\left(P_{opt}/h\upsilon\right)}{WLD} \tag{4. 4}$$

where η is the quantum efficiency, that is the number of carriers generated per incident photon, and n is the carrier density, the number of carriers per unit volume.

The photocurrent flowing between the electrodes is

$$I_p=(\sigma E)WD=\left(q\mu_n nE\right)WD=(qnv_d)WD \tag{4. 5}$$

where E is the electric field inside the photoconductor and v_d is the carrier drift velocity. By combining the last two equations (4.4) and (4.5), it is obtained:

$$I_p=q\left(\eta\frac{P_{opt}}{h\upsilon}\right)\left(\frac{\mu_n\tau E}{L}\right) \tag{4. 6}$$

If the primary photocurrent I_{ph} is defined as:

$$I_{ph}=q\left(\eta\frac{P_{opt}}{h\upsilon}\right) \tag{4. 7}$$

the photocurrent gain is given by:

$$Gain=\frac{I_p}{I_{ph}}=\frac{\mu_n\tau E}{L}=\frac{\tau}{t_r} \tag{4. 8}$$

where $t_r=L/v_d=L/\mu_n E$ is the carrier transient time. The gain depends on the ratio of the carrier lifetime τ to the transit time t_r.

4.3 Photodiode characteristics

Photodiodes are frequently used photodetectors. They are semiconductor devices whose family includes p-n junction diode, metal-semiconductor junction diode, heterojunction photodiode and p-i-n diode.

These devices usually operate under large reverse biasing voltages. When incident light is absorbed by the photodiode, electron-hole pairs are generated in the depletion region. The photogenerated e-h pairs are then separated by the electric field and, as a consequence, an electric current flows in the external circuit.

The general characteristics of a photodiode are the quantum efficiency, responsivity and response speed.

The quantum efficiency, previously defined as the number of electron-hole pairs generated for each incident photon, can be experimentally determined by:

$$\eta = \frac{\left(\frac{I_{ph}}{q}\right)}{\left(\frac{P_{opt}}{h\upsilon}\right)} \qquad (4.\ 9)$$

The quantum efficiency is generally expressed in a percentage and it basically measures the effectiveness of the radiant energy for producing electrical current in a detector. It can be either internal or external. The internal quantum efficiency is the number of electron-hole pairs created divided by the number of photons absorbed. Instead, the external quantum efficiency depends on a number of factors as the material absorption coefficient and the thickness of the absorbing region. It is a measure of how many photons are detected or counted by the device.

A related figure of merit is the responsivity, which gives a measure of photodetector sensitivity to incident optical energy. It is defined as the ratio of the photocurrent to the optical power, measured in A/W:

$$R = \frac{I_p}{P_{opt}} = \frac{\eta q}{h\upsilon} = \frac{\eta\,\lambda(\mu m)}{1.24} \qquad (4.\ 10)$$

Therefore for a given quantum efficiency, the responsivity increases linearly with wavelength. The spectral response, generally plotted as responsivity versus wavelength, is reported in Fig. 4.3, in the general case of a silicon photodiode, where real and ideal characteristics are compared [146].

The reflection and absorption characteristics of the detector material change with wavelength. In particular, since the absorption coefficient α is a strong function of the wavelength, for a given semiconductor, the wavelengths range in which appreciable photocurrent can be generated is limited. As previously mentioned, the long wavelength cut-off is determined by the energy gap of the semiconductor. For wavelength longer than this value absorption is too small to give appreciable absorption. The short wavelength cut-off of the photo-response comes about because the value of absorption for short wavelength is very large and the radiation is absorbed very near to the surface, where the recombination time is short. Responsivity not only depends on wavelength but even on bias voltage and temperature. Indeed, responsivity may vary with voltage due to depletion width widening, which increases the active area of the photodiode with the applied electric field [147]. As the temperature changes, the optical constants of the detectors material and its collection efficiency change too [148].

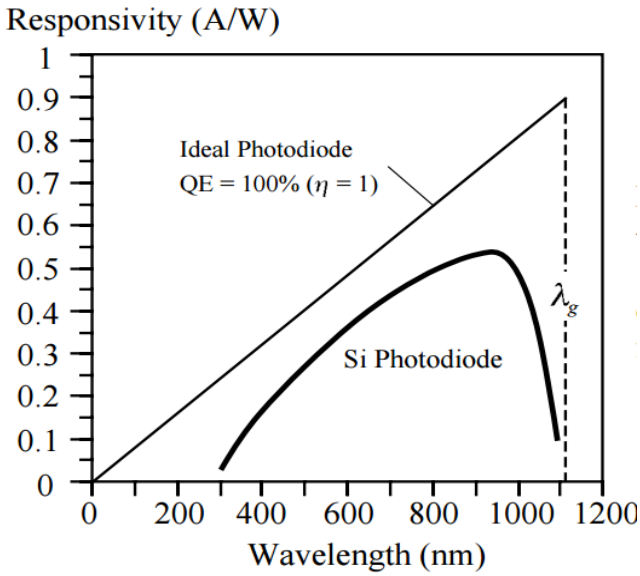

Fig. 4. 3 Responsivity vs. wavelength for an ideal photodiode with quantum efficiency QE = 100% (η = 1) and for a typical commercial Si photodiode [146].

As regard the response speed, it is generally limited by diffusion of carriers, drift time in the depletion region, and capacitance of the depletion region. Carriers generated outside the depletion region must diffuse to the

junction resulting in considerable time delay. To minimize the diffusion effect, the junction should be formed very close to the surface. The greatest amount of light will be absorbed when the depletion region is wide. However, the depletion layer must not be too wide or transit time effects will limit the frequency response. It also should not be too thin, or excessive capacitance C will result in a large *RC* time constant, with *R* the load resistance. The optimal compromise is the width at which the depletion layer transit time is approximately one half the modulation period.

On one hand, in order to increase the quantum efficiency, the depletion layer must be sufficiently thick to allow a large fraction of the incident light to be absorbed. On the other hand, for high-frequency operation, the depletion region must be kept thin to reduce the transit time. Thus, a trade-off between the response speed and quantum efficiency must be found.

4.4 P-i-n photodiode

Among the most common structures for photodetection there is the p-i-n photodiode, schematically shown in Fig. 4.4. It consists of a highly p-doped and a highly n-doped regions separated by an intrinsic region of high resistivity.

When the structure is adequately illuminated, light passes through the very thin p-doped top layer (deliberately made thin enough so that a negligible absorption occurs in it) and most photons reach the depletion region (the intrinsic layer) where an electric field exists.

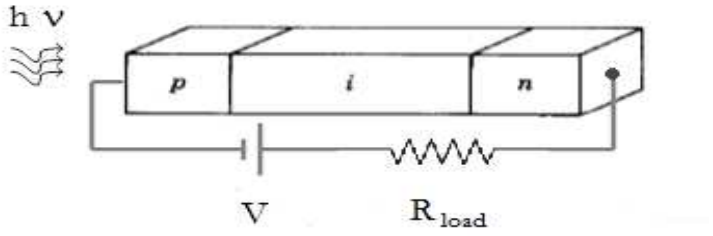

Fig. 4. 4 Schematic representation of a p-i-n photodiode.

A p-i-n photodiode is normally reverse biased to fully deplete the intrinsic region to collect photo generated carriers. Fig.s 4.5 a-b show the energy band diagram of the p-i-n diode under reverse bias condition and its optical absorption characteristic. Light absorption in the semiconductor produces electron-hole pairs. Pairs produced in the depletion region or within a diffusion length of it will eventually be separated by the electric field, whereby a current flows in the external circuit as carriers drift across the depletion layer.

Under steady-state conditions the total current density through the reverse-biased depletion layer is given by [12]:

$$J_{tot}=J_{dr}+J_{diff} \qquad (4.\ 11)$$

where J_{dr} is the drift current due to carriers generated inside the depletion region and J_{diff} is the diffusion current density due to carriers generated outside the depletion layer in the bulk of the semiconductor and diffusing into the reverse-biased junction. The total current can be derived under the assumptions that the thermal generation current can be neglected and that the surface p layer is much thinner than $1/\alpha$.

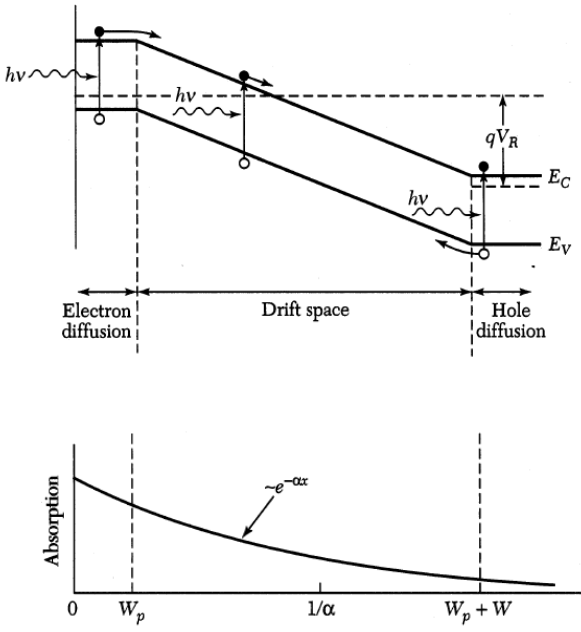

Fig. 4. 5 Energy band diagram under reverse bias [12].

Referring to Fig. 4.5 b, the hole-electron generation rate is given by:

$$G(x) = \Phi_0 \alpha e^{-\alpha x} \tag{4. 12}$$

where Φ_0 is the incident photon flux per unit area given by:

$$\Phi_0 = \frac{P_{opt}(1-R)}{A h\upsilon} \tag{4. 13}$$

where R is the reflection coefficient and A is the device area. The drift current J_{dr} is thus given by:

$$J_{dr} = -q \int_0^W G(x)dx = q\Phi_0 \left(1-e^{-\alpha W}\right) \tag{4. 14}$$

where W is the depletion layer width. For x>W, the minority-carrier density (holes) in the bulk semiconductor is determined by the one-dimensional diffusion equation:

$$D_p \frac{\partial^2 p_n}{\partial x^2} - \frac{p_n - p_{n0}}{\tau_p} + G(x) = 0 \tag{4. 15}$$

where D_p is the diffusion coefficient for holes, τ_p the lifetime of excess carriers, and p_{n0} the equilibrium hole density. The solution of the previous equation, under the boundary conditions $p_n = p_{n0}$ for $x=\infty$ and $p_n = 0$ for x=W is given by:

$$p_n = p_{n0} - \left(p_{n0} + C_1 e^{-\alpha W}\right) e^{\frac{(W-x)}{L_p}} + C_1 e^{-\alpha x} \tag{4. 16}$$

with $L_p = \sqrt{D_p \tau_p}$ and $C_1 = \left(\frac{\Phi_0}{D_p}\right) \frac{\alpha L_p^2}{1-\alpha^2 L_p^2}$. The diffusion current density is given by $J_{diff} = -qD_p \left(\frac{\partial p_n}{\partial x}\right)_{x=W}$, therefore:

$$J_{diff} = q\Phi_0 \frac{\alpha L_p}{1+\alpha L_p} e^{-\alpha W} + q p_{n0} \frac{D_p}{L_p} \tag{4. 17}$$

The total current density is finally obtained as:

$$J_{tot}=q\Phi_0\left(1-\frac{e^{-\alpha W}}{1+\alpha L_p}\right)+qp_{n0}\frac{D_p}{L_p} \qquad (4.\ 18)$$

The electric field (Fig. 4.6) is relatively constant in the intrinsic region because of its high resistivity (i.e. low doping concentration), so that few volts of reverse bias are needed to cause the depletion region to extend all the way through to the n region and thus provide a large sensitive volume. The depletion region width in a p-i-n structure is then practically independent of the applied voltage and thus much better delineated than in a p-n structure where the depletion region width will vary appreciably with applied voltage [149].

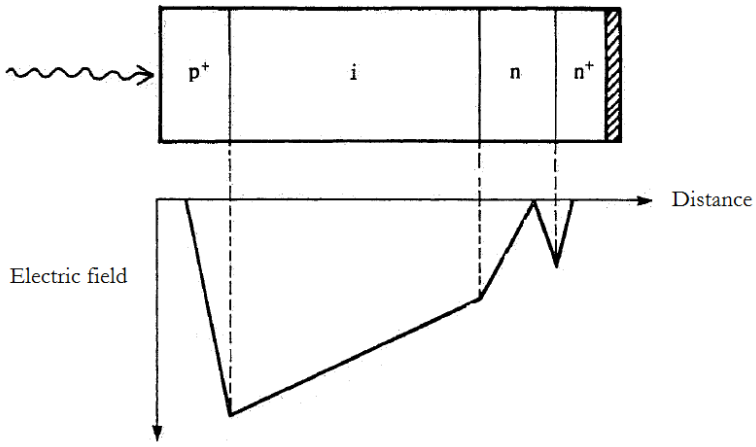

Fig. 4. 6 Electric field distribution within a p-i-n structure [149].

4.4.1 Electrical Characterization of a pin photodiode

Among the main parameters used to study a pin photodiode, beyond the previously discussed responsivity and quantum efficiency, dark current is also used.

The current-voltage characteristic of a photodiode with no incident light is similar to a rectifying diode. In particular, when the photodiode is forward biased, there is an increase in the current. When a reverse bias is applied, a small reverse saturation current appears. It is related to dark current as:

$$I_D=I_{SAT}\left(e^{\frac{qV_A}{kT}}-1\right) \qquad (4.\ 19)$$

where I_D is the photodiode dark current through the diode for zero illumination and it will be non zero due to background radiation and thermally excited minority saturation current; I_{SAT} is the reverse saturation current, q is the electron charge, V_A is the applied bias voltage, k the Boltzmann constant and T is the absolute temperature.

Illuminating the photodiode with optical radiation, produce a shift in the I-V curve by the amount of photocurrent (I_P). Thus:

$$I_{Total}=I_{SAT}\left(e^{\frac{qV_A}{kT}}-1\right)+I_P \qquad (4.\ 20)$$

As the applied reverse bias increases, there is a sharp increase in the photodiode current. The applied reverse bias at this point is referred to as breakdown voltage. This is the maximum applied reverse bias, below which, the photodiode should be operated (also known as maximum reverse voltage). In Fig. 4.7 a schematic representation of dark and photo-generated currents is shown together with the breakdown voltage.

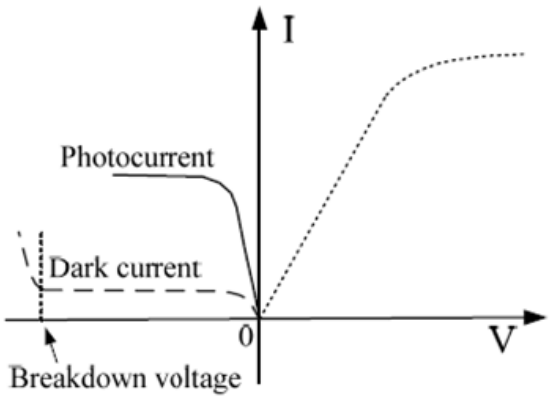

Fig. 4. 7 Schematic representation of I-V characteristic showing photocurrent and dark current.

5
Bulk carbon-based material: Silicon Carbide

Carbon is a very special element because it is able to form a variety of compounds. Among the most stable, silicon carbide has currently gained a lot of attention. Indeed, since silicon devices are reaching their physical limits, associated to the narrow bandgap, low thermal conductivity and low critical electric field, and will not be able to further improve, silicon carbide is regarded as the most suitable substitute. Due to its unique electrical and chemical properties, this material is becoming very attractive in the electronics field.
In this chapter an overview of the most important properties of silicon carbide together with its experimental characterization will be presented.

5.1 Introduction

Carbon is among the most abundant elements in the universe. It is found in large quantities in the sun, stars, comets, and atmospheres of most planets. It is even present dissolved in all natural waters. In general, carbon is the elementary building block of all organic molecules and, therefore, responsible for life on earth.

Carbon is very special because it can form lots of compounds with others elements. The explanation lies deep inside the carbon atom. Indeed, due to carbon electronic configuration, atoms can form strong covalent bonds with four other atoms. If carbon atoms link together, long chains or rings can be formed. These kind of compounds are the so-called hydrocarbons, such as polymers and petroleum.

Among the most stable compounds, great attention has been recently devoted to silicon carbide (SiC). Indeed, due to its excellent properties, SiC has been envisaged as a possible substitute to silicon in specific applications, where more performing properties are required.

Conventional electronics mainly based on traditional materials, such as silicon, has greatly advanced throughout the past decades, with increasingly improved performance thanks to the well established manufacturing technology. Indeed, these materials are still dominating the semiconductor industry, completely fulfilling Moore's law. The size of electronic devices has progressively decreased allowing their integration onto a single chip, thereby realizing smaller and more efficient systems. However the increasing demand for faster and more affordable devices is slowly revealing the limits of traditional materials for electronics. New challenges in terms of increasing complexity, operation in high-power, high frequency and high radiation-dose regimes, have to be faced.

Silicon carbide, the most mature among the wide-bandgap semiconductors, seems to be able to embody this scenario.

5.2 Silicon Carbide

Silicon carbide (SiC) is considered a promising semiconductor material that, owing to its outstanding properties, shows many advantages compared to the conventional semiconductors, especially in harsh environments applications [141]. In fact, the strong covalent bonds and wide band gap confer to SiC excellent physical stability and large breakdown electric fields. These characteristics promote the development of high-temperature, high-power and high-frequency applications as well as UV optoelectronic devices [150]. The knowledge of material characteristics is essential for the design and development of devices based on it.

Therefore in this chapter, silicon carbide structure and properties will be briefly introduced, along with the experimental characterization performed on a 4H-SiC sample, of basic importance for the analysis of the physical sensor realized in this work.

5.2.1 Silicon Carbide structure

Silicon carbide is a binary compound of carbon and silicon atoms in a 1:1 ratio. The smallest element of any SiC lattice is a tetrahedron of a C atom

surrounded by four Si atoms in strong sp^3 bonds, as shown in Fig. 5.1. The distance between the C atom and each of the Si atoms is approximately 2.52 Å.

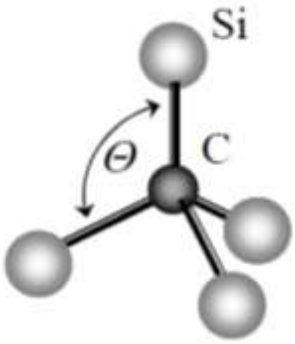

Fig. 5. 1 Silicon carbide tetrahedral cell.

Crystalline SiC forms long range ordered structures and, according to the possible stacking sequence along the crystallographic axis direction, it is characterized by many different polytypes, each one identified by their own electrical and optical properties [151]. To date more than 200 different polytypes of SiC are known to exist. The crystalline structure of any SiC polytype can be viewed as the stacking sequence of close-packed spheres, where each plane of spheres represents a Si-C bilayer.

Usually, each polytype is identified by Ramsdell notation [152], with a number followed by a letter. The number denotes the count of double layers in one period, and the letter stands for the symmetry of the Bravais lattice, which can be cubic (C), hexagonal (H) or rhombohedral (R). Each SiC bilayer can be characterized by one of the three stacking sequences of layers (A, B, or C). If the stacking assumes ABCABC order, the structure will be zincblende, also known as 3C-SiC; if the stacking sequence is ABAB, wurtzite or equivalently 2H-SiC will be obtained. Other polytypes are mixtures of zincblende and wurtzite structures and among these the most common are the hexagonal polytypes such as 4H-SiC, characterized by ABAC staking and consisting of equal amounts of cubic and hexagonal bonds, and 6H-SiC whose staking sequence is ABCACB and mainly cubic. More complex structures are the rhombohedral ones, characterized by increasingly complex stacking sequence along the axial direction, ABCACBCABACABCB [153].

In Fig. 5.2 the main SiC polytypes are displayed.

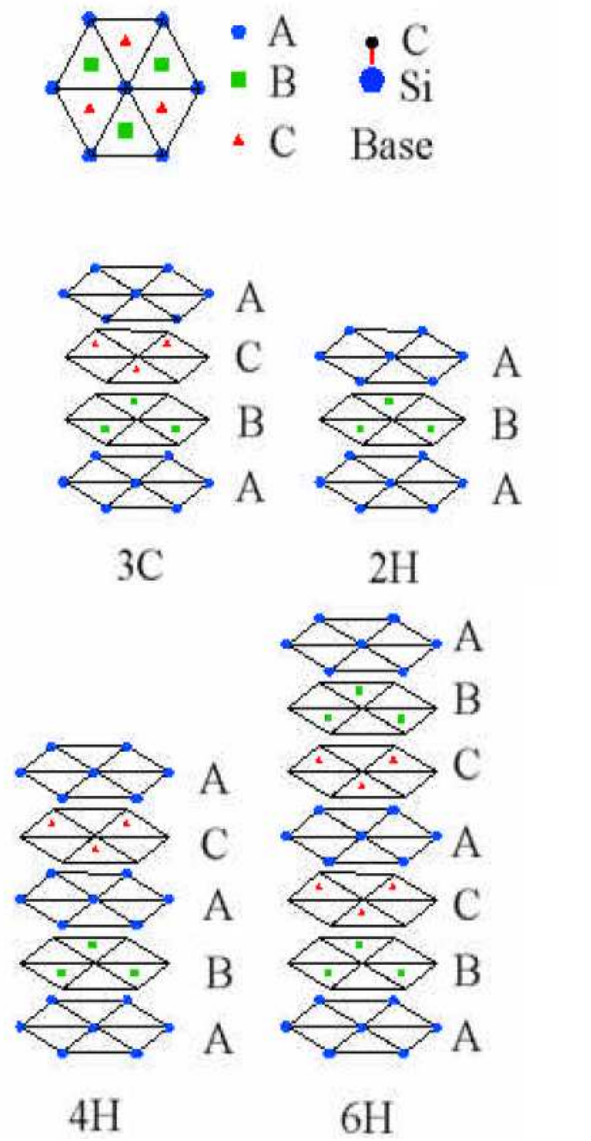

Fig. 5. 2 Stacking order of silicon carbide hexagonal planes. The most common structures 3C (cubic) and 2H, 4H, 6H (hexagonal) are shown [154].

At present, there is no satisfactory theory in all regards, capable of explaining why SiC crystallizes in the form of a large number of polytypes. In addition, it is not completely clear what factors favor the formation of one or another polytype [155].

5.2.2 Silicon Carbide Synthesis

Silicon carbide is a very rare compound in nature and till nowadays has not been found freely. It was first discovered by Moissan in 1905, who found small hexagonal platelets in a meteorite, even if in 1824 Berzelius had already

observed it in an attempt to synthesize diamond [156]. In the 1950s some interest arouse around SiC and the possibility to use it as a semiconductor material in the field of solid state electronics. It was just the beginning of its study. Thus, crystal growth techniques, able to produce high quality bulk SiC, were proposed [157].

The production of bulk SiC crystals defect-free, of large-area and with well-controlled dopant concentrations are among the main requirements for the full use of SiC in electronic applications. In order to grew bulk samples, seeded sublimation growth is the principle technique. Briefly it consist in the transport of materials from the source to the seed. In particular, in a closed system, thanks to a temperature gradient, a solid SiC powder is transported to the seed. The growth process needs very high temperatures up to 2500°C.

Instead, High Temperature Chemical Vapor Deposition (HTCVD) consists of the chemical vapor deposition of gases, containing Si and C such as silane (SiH_4) and ethylene (C_2H_4). When heated they decompose and form solid particles as a mixture of Si and C. With a further sublimation process they are transported to the seed resulting in the production of high-purity material.

Anyway, the quality obtained with this process is not good enough for electronic devices. For this reason thin layers, with thickness in the micrometer range, are usually grown on the top of a bulk substrate through epitaxial growth. Vapor phase epitaxy (VPE) is used to this purpose. Usually, the substrate is placed into a CVD reactor under a precursor gas flow containing Si and C. Lower temperatures with respect to the bulk growth, around 1500°C, are used. The technique is able to lead to a higher crystalline quality [158], this time suitable for active layer fabrication in electronic devices. Anyway, some intrinsic defects are always present due to the SiC production process, such as dislocations, stacking faults and the so-called micropipes.

It should be also pointed out that it is not so simple to obtain the desired polytype. Indeed, 4H and 6H-SiC are commonly obtain since the seeded sublimation growth technique is suitable for their production. 2H-SiC for example cannot be grown in large-area stable pieces such as 15R-SiC. 3C-

SiC is difficult to obtain too, even if in the last years bulk crystals of large diameter have been successfully produced [159].

Moreover, a large range of doping concentrations can be achieved for both n- and p-type during the CVD growth process. In fact, the doping of SiC occurs by addition of a gas containing the atoms of the dopant species. Usually, for n-type doping nitrogen and phosphorus are commonly used, whereas p-type doping is obtained with aluminum or boron dopant. In case of selective doping over determined regions and with particular dopant atoms, ion implantation is instead commonly applied.

5.2.3 Silicon Carbide Properties

Silicon carbide has attracted so much attention due to its excellent properties. It is chemically inert, hard and temperature resistant. Thanks to its chemical inertness, 4H-SiC does not react with other materials at room temperature. Thanks to the strong covalent bonds it is the ideal candidate for high temperature applications, where silicon cannot operate. For these reasons SiC is commonly regarded as one among the best materials able to efficiently operate even in harsh environments [141].

In Table 5.1 physical and electrical characteristics of 4H-SiC are reported together with those of silicon, the most used material in electronics, and diamond, wide bandgap material well known for its extreme properties but quite difficult to grew in the form of large single-crystals and to dope with donor impurities.

From a direct comparison of the fundamental electrical properties, the advantages of SiC with respect to Si are basically the higher bandgap, more than twice increase of the thermal conductivity, the higher saturation velocity and the higher critical electric field. It is evident that 4H-SiC, is a very promising material in high performance electronic devices, where a higher critical electric field brings to power devices with higher breakdown voltages.

Indeed, high-purity SiC material has a higher thermal conductivity value, compared to silicon. For this reason, SiC is able to work at high power levels and dissipate, away from the chip, large amounts of generated heat, which causes a temperature increase that could alter devices performance.

This obviates the need to have bulky and expensive cooling systems, contrary to other semiconductors, such as Si. This is undoubtedly a great advantage in relation to cost, size and weight of power electronic systems [160].

Table 5. 1 Physical characteristics of Diamond, Si and 4H-SiC [161, 162, 163].

Property	**Diamond**	**Si**	**4H-SiC**
Bandgap (eV)	5.48	1.12	3.26
Electron mobility ($cm^2/V\ s$)	2200	1400	900
Hole mobility ($cm^2/V\ s$)	1600	480	600
Thermal conductivity (W/cm K)	20	1.5	3.7
Saturation velocity (cm/s)	$2.7 \cdot 10^7$	$1 \cdot 10^7$	$2.7 \cdot 10^7$
Breakdown voltage (V/cm)	$1 \cdot 10^7$	$3 \cdot 10^5$	$30 \cdot 10^5$
Critical electric field	10	0.3	3.5
Dielectric constant	5.7	11.8	9.6
Hardness (Kg/mm^2)	10000	1000	2130
Young modulus (GPa)	1134	160	410.47

Moreover, SiC is also characterized by high saturation velocity. Electrons and holes are accelerated by electric fields, but they lose momentum because of various scattering mechanisms such as scattering from optical phonons, impurity ions, crystal defects, or other material imperfections [164]. Electrical field E and drift velocity v_D, are proportional by means of mobility, which is dependent on the local electric field, doping concentration, polytype, crystal quality, local scattering at defects, etc.. As an example, if the doping concentration increases, the mobility decreases due to scattering. However, for ever increasing fields, the direct proportionality fails, and v_D becomes saturated so it does no more increase with increasing electrical fields. Then, the mobility is no longer a useful quantity, but the saturation electron/hole drift velocity is used instead. In this way, the maximum speed of devices operating at high field strengths is directly related to this quantity. Thus a high-saturated drift velocity is advantageous in order to obtain as high channel currents and high frequencies as possible, and clearly SiC is an ideal material.

SiC is also reported to have a high breakdown electric field and it can withstand an electric field greater than GaAs or Si without undergoing avalanche breakdown. This high breakdown electric field enables the fabrication of very high-voltage, high-power devices. Additionally, it allows the devices to be placed very close together, providing high device packing density for integrated circuits [165].

In general, even if over than 200 SiC polytypes exist, they can be thought as a whole class of materials that have common physical properties [166]. Although the physical properties are similar for all of the polytypes, different is the case of the electronic properties. Many of the favorable transport parameters in SiC are related to its large bandgap. Indeed, along with conduction and valence band structure, it defines the electric properties of the semiconductor. For instance, all of them have an indirect bandgap, even if it varies in a wide range from 2.3 (3C) to 3.33 eV (2H), according the degree of hexagonality [167].

For this reason, when considering electronic devices, each polytype has its specific advantages. For example, 4*H* is better suited for high power and high temperature, while 3*C* should be better for high frequency applications. Another example could be the saturation drift velocity of carriers which is higher in 4H than in 6H-SiC, making the propagation of electronic signals faster in 4H-SiC.

5.3 4H-SiC characterization

Among all of the polytypes, the hexagonal structure 4H-SiC was considered thanks to the rapid increase of its use as a suitable material for optoelectronic applications. Indeed, it is characterized by visible blindness (bandgap of 3.26 eV), and radiation-hardness [168, 169]. Such properties, combined with controllable n- and p- type doping make it an ideal material for several potential applications.

The 4H silicon carbide used in this work was a commercially available n-doped wafer provided by CREE Research supplier. As previously reported, an affordable and reliable synthesis technique is still lacking. Moreover, due to

the high number of parameters that must be controlled during the process as well as the possible production of low quality crystals, laboratory synthesis may be a difficult task.

The substrate was processed in order to grew an almost intrinsic epilayer on it and a further aluminum-doped region was ion implanted, as it will be better described in Chapter 6. Basically, a three-layer p-i-n structure was obtained. Multiple characterizations were performed in order to prove and verify the good quality of the material, as well to assess its crystalline structure, morphology and properties. For this purpose micro-Raman spectroscopy, Raman mapping and spectroscopic ellipsometry were used.

Raman spectroscopy technique has been introduced in Chapter 2 for the characterization of low dimensional carbon materials and continue to be valid in the case of bulk carbon materials too. Obviously, a different Raman response is obtained and peaks assume other meanings, according to the different phonon dispersion relation in SiC [170].

As regard spectroscopic ellipsometry, it is an optical technique used to investigate the dielectric properties of thin films, such as refractive index and extinction coefficient. Typically, a polarized incident radiation, interacts with the sample and changes its polarization (Fig. 5.3). This change is quantified by the amplitude ratio, Ψ, and the phase difference between p- and s-polarized light waves, Δ. The technique is also sensitive to several material properties such as optical parameters, thickness, surface and interface roughness of stacked thin films and substrates.

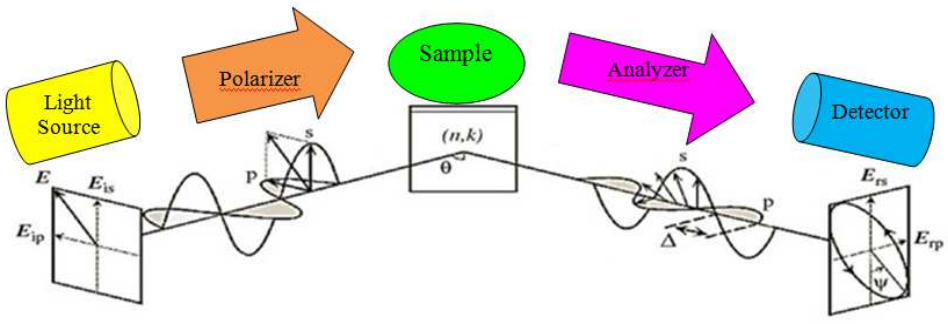

Fig. 5. 3 Schematic representation of ellipsometry operating principle.

Material properties have been measured, at room temperature, by a Variable Angle Spectroscopic Ellipsometry (VASE by J.A. Woollam Co.) at photon energies E ranging between 0.5 and 4.1 eV (λ range 300-2500 nm), Fig. 5.4. The rotating-analyzer ellipsometer was equipped with an automated compensator function that allowed accurate determination of the ellipsometric parameter, Ψ and Δ. In order to increase the information available about sample, measurements were carried out at multiple angles of incidence 65°, 70° and 75°, near the material Brewster's angle.

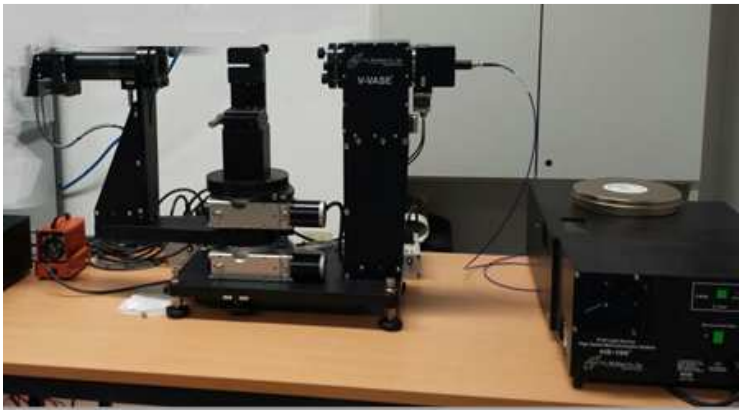

Fig. 5. 4 Variable Angle Spectroscopic Ellipsometry, VASE by J.A. Woollam Co. (Optical Spectroscopy Laboratory - Mediterranea University of Reggio Calabria).

However, the measured data Ψ and Δ, namely the amplitude ratio and the phase difference between *p*- and *s*-polarized light waves, are not useful by themselves, but must be compared with an appropriate model in order to extract correctly the information of interest. Thus, the measured light polarization states has to be converted in terms of refractive index (n) and extinction coefficient (k) by means of a model-based regression analysis. Briefly, in the modeling process, the number of layers of the analyzed sample should be declared and the optical functions of each layer need to be determined. If the layer optical functions are well known, the tabulated data can be used; on the other hand, for materials with unknown optical functions, more complex models must be employed [171].

5.3.1 4H-SiC Raman Spectroscopy

The intrinsic 4H-SiC, p- and n-type doped layers were investigated by Raman spectroscopy [172]. As well known, Raman modes are representative of a unique crystal structure and it is therefore possible to discern among the different SiC polytypes [151]. Moreover, Raman scattering efficiency in SiC is relatively high because of strong covalent chemical bonds, and a number of other information, such as disorder, damage, lattice strain and impurities can be extracted [173].

Fig. 5.5 (a, b) shows the measured first- and second-order Raman spectra from intrinsic 4H-SiC, taken at room temperature, in back scattering configuration. The first-order 4H-SiC Raman spectrum is in accordance with the literature data [174]. In the spectrum (Fig. 5.5 a), the peak at 203.6 cm^{-1} is an E_2 transverse acoustic (TA) mode, 609.5 cm^{-1} is A_1 longitudinal acoustic mode (LA), 776.1 cm^{-1} is an E_2 transverse optical (TO) mode, 796.7 cm^{-1} is an E_1 transverse optical (TO) mode and 963.5 cm^{-1} is an A_1 longitudinal optical (LO) mode [175, 174]. Furthermore, weaker peaks are observed in the spectrum at 196.7 and 264.9 cm^{-1} (E_2 and E_1 transverse acoustic mode, respectively). In addition, the second-order Raman scattering is also displayed (Fig. 5.5 b). It can be seen that the Raman peaks are labeled *a* (1475.8 cm^{-1}), *b* (1515.8 cm^{-1}), *c* (1541.8 cm^{-1}), *d* (1622.1 cm^{-1}), *e* (1654.8 cm^{-1}), *f* (1688.6 cm^{-1}), *g* (1712.6 cm^{-1}), *h* (1924.2 cm^{-1}), in accordance with reported assignment [174].

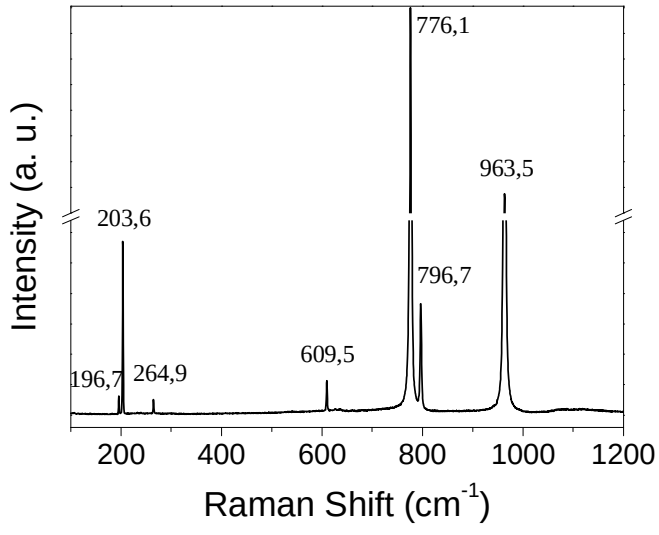

(a)

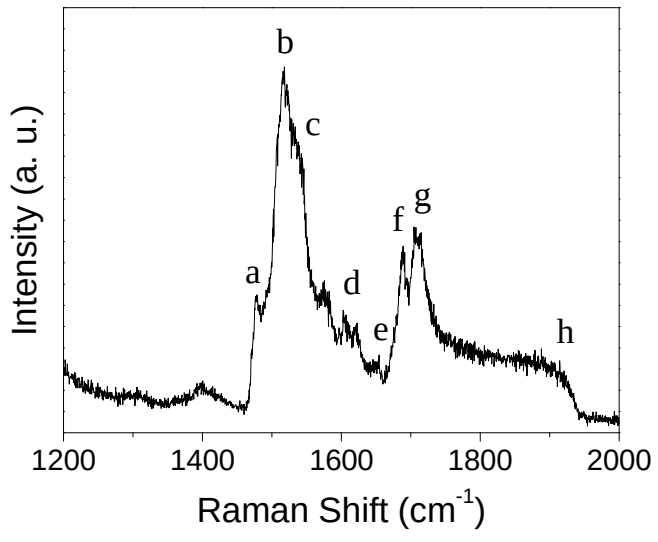

(b)

Fig. 5. 5 4H-SiC intrinsic sample Raman spectra (a) first-order, (b) second-order.

The second-order Raman scattering spectrum, rarely reported in the literature, is barely considered since its peaks are nearly independent of polytypes and impurities [176, 175]. On the contrary, according to the change in bandwidth, intensity, and frequency of first-order Raman peaks, useful information on 4H-SiC crystalline structure, such as defects, doping effects and stress evaluation can be obtained [175]. Indeed, being the frequency of E_2 (TO) Raman mode nearly unaffected by the presence of carrier concentration, it can be used as a qualitative measure of the internal strain [177]. The peak stress free value of 4H-SiC is regarded to be 777 cm^{-1}. It has been reported that a shift towards lower (higher) frequency is an index of the presence of a tensile (compressive) stress within the sample [178].

The analyzed intrinsic sample was proved to be spatially uniform and of good crystalline quality.

Fig. 5.6 shows typical Raman data of variously doped 4H-SiC (a, n-type and c, p-type) compared with the intrinsic one (b).

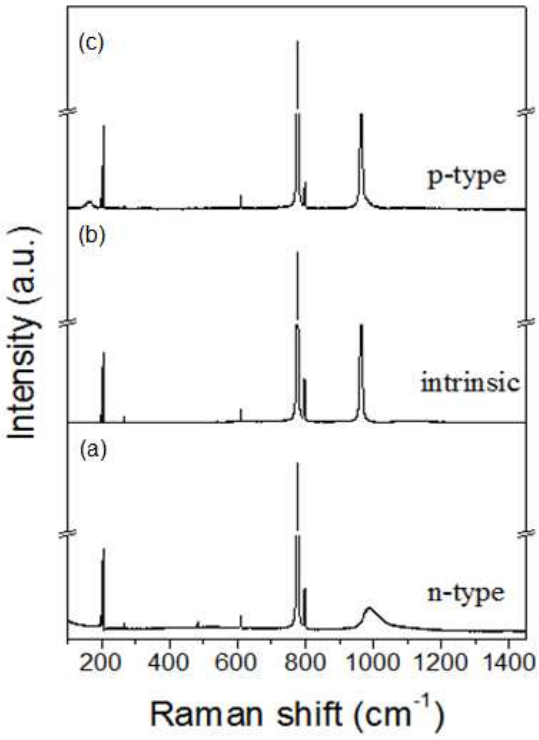

Fig. 5. 6 4H-SiC Raman spectra recorded on samples: (a) p-type doped (b) intrinsic and (c) n-type doped.

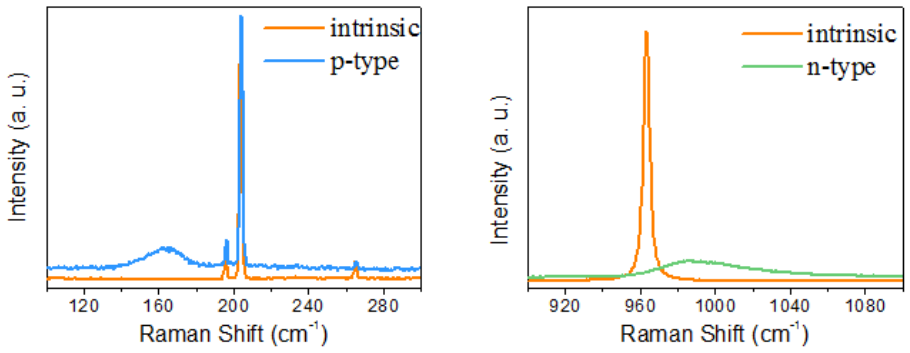

(a) (b)

Fig. 5. 7 Detail of the Raman spectra of 4H-SiC (a) at low and (b) high frequency. Both p- and n-type spectra are compared with the intrinsic one.

Raman spectrum of n-doped sample is shown in Fig. 5.6 c. The featuring peaks are still the same as reported for the intrinsic sample, unless for the A_1 (LO) mode at ~964 cm^{-1}. Significant changes are observed in the shape and position of this band as a function of increasing doping concentration [178, 175]. The presence of nitrogen determines a broadening

and a shift to higher frequency of the peak, while its intensity decrease sharply (Fig. 5.7 a). In particular, it has been assumed that the carrier concentration shifts the peak towards the high wavenumbers while a decrease in mobility contributes to increase the asymmetry of the line [177]. Such a behavior is generally ascribed to the phonon-plasmon coupling mechanism [179]. None of the other strong Raman peaks shifts or broadens in the studied doping concentration range. In Fig. 5.6 c, p-type doped sample spectrum is displayed. The strongest modes, quite sensitive to the type and degree of crystallization are roughly centered as for the intrinsic sample. An increase of the low frequency baseline, proportional to the doping level, is evidenced [180]. Moreover, a new peak, characterized by low intensity and high width, is registered at about 164 cm^{-1} (Fig. 5.6 b).

Since inhomogeneous doping of layers produces not uniform properties and subsequently poor quality material, micro-Raman mapping was further use to prove the spatial uniformity of the p-type implanted region and the underlying intrinsic epilayer. Raman imaging measurements were performed on a rectangular area enclosing p-doped and intrinsic region as shown in Fig. 5.8.

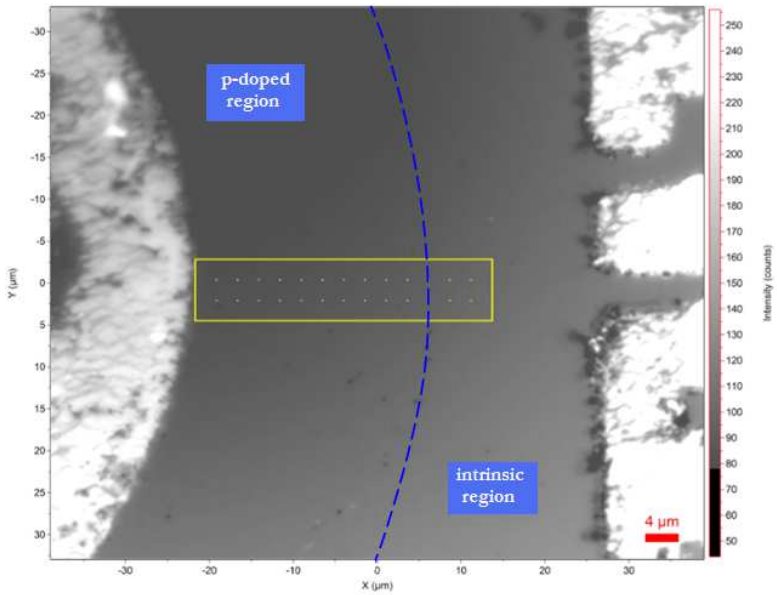

Fig. 5. 8 Raman map showing the p-type implanted region over the intrinsic 4H-SiC epilayer. The blue dashed line delimits the two different doped regions.

Individual spectra, recorded for each point of the map, showed in Fig. 5.9 a, are perfectly overlapped, proving film uniformity, unless for the peak at about 164 cm^{-1}, assumed to be a typical feature of p-doped sample.

The variation in intensity of the Raman peaks centered at 164, 797.5 and 963.6 cm^{-1} was monitored (Fig. 5.9 b-d). The intensities of the peaks are reported towards the x position of the map points. Band at 164 cm^{-1} shows a sharp decrease in intensity indicating the transition from p-type doped to intrinsic region, where such peak is no more evident. The constant plateau registered before the separation zone and the rapid variation, suggest the high quality of the p-implanted region. On the contrary, the most intense bands being not sensitive to dopants impurities, show a constant intensity value over the analyzed area hinting at a spatially uniform intrinsic epilayer.

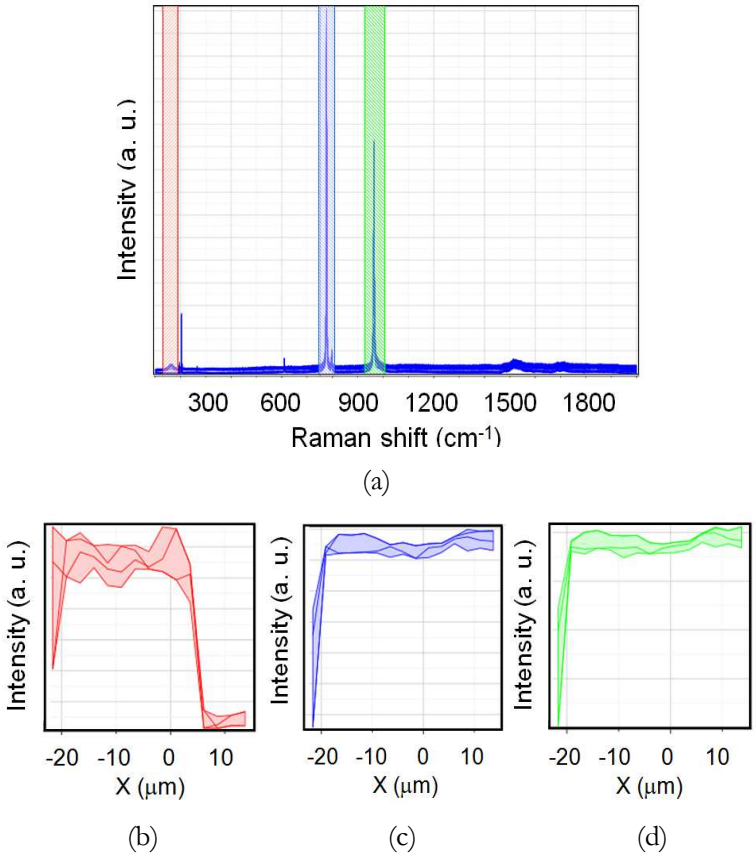

Fig. 5. 9 (a) Raman spectra recorded for each map point; intensity of the monitored peak centered at (b) about 164 cm^{-1}, (c) 797.5 cm^{-1} and (d) 963.6 cm^{-1}.

5.3.2 4H-SiC ellipsometric characterization

4H SiC intrinsic sample was studied by spectroscopic ellipsometry in the 0.5 ~ 4.1-eV photon-energy range. The Tauc-Lorentz multi-oscillator model, introduced by Jellison and Modine [181] was used as the parameterization model of the optical constants, conveniently corrected for the surface roughness. It resulted to work very well since in curves fitting no significant differences was found between the experimental data and generated model ones. The measured dispersion curves of intrinsic 4H-SiC optical constants, index of refraction and extinction coefficient, are shown in Fig. 5.10 a, b.

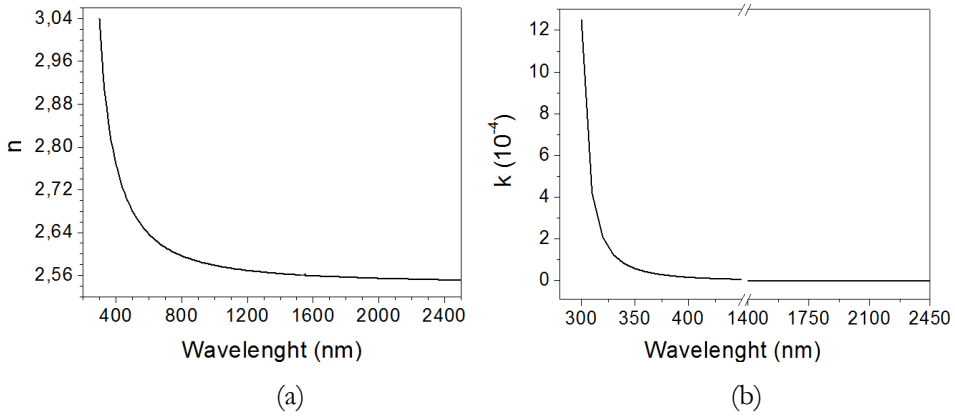

Fig. 5. 10 (a) 4H-SiC refractive index, n, and (b) extinction coefficient, k.

It is clearly displayed that upon decreasing wavelength n increases and the dispersion becomes larger towards the band edge. Reported values are in good agreement with those reported in other works [182]. The same fitting analysis was used to determine the extinction coefficient. It is clear that k increases rapidly at energy higher than the energy bandgap (E_g=3.2 eV) and is equal to zero for lower energies, where no light absorption in media can be detected (Fig. 5.10 b). In fact, being the extinction coefficient related, by Lambert-Beer equation [171], to absorbance $\alpha = \frac{4\pi k}{\lambda}$ it reveals that the intrinsic sample is transparent under the bandgap value. On the contrary, in the high-energy region, light absorption in sample generally increases and penetration depth of light becomes smaller.

6
4H-SiC UV photodetector

The outstanding properties of the hexagonal 4H silicon carbide have been exploited for the realization of a photodetector able to work in the UV range. In particular, a flame detector configured as a p-i-n diode structure was characterized and tested in the UV region.
In this chapter the experimental results on the p-i-n performance will be presented along with a simulative analysis aimed at providing more insight in the obtained results.

6.1 Introduction

Photodetectors based on wide band gap semiconductors are commonly used in a variety of applications. Silicon carbide (SiC), as already discussed, is considered particularly suitable for UV detection. In particular, an application as flame detector will be discussed in the following.

An ideal flame detector should be unaffected by ambient conditions and at the same time it should reliably sense the flame of interest, while totally ignoring all the other signal sources. Therefore, being flame monitoring essential in any combustion safety system, a selective detector is strongly required. For instance, when natural gas is burned, optical energy, especially in the UV/Visible region, resulting from the chemical transformations during the combustion process, is more significant than heat emissions [140]. Therefore the emission of UV radiations is strong in the very early stages of combustion. The spectral lines, resulting from chemical reaction, give the natural gas flame a unique signature.

Till nowadays UV flame detectors have been mostly based on gas photomultiplier tubes. But extremely sensitive UV detectors able to withstand high temperatures are required and the possibility to use UV sensitive solid-state detectors may lead to several advantages. A great deal of research has been carried out to develop high- performance 4H-SiC UV photodiodes with different device structures, such as Schottky, metal-semiconductor-metal, p-n

junction, p-i-n junction, and avalanche photodiodes [145, 140, 144]. Among these structures, p-i-n photodiodes are of particular interest due to a lot of advantages such as low dark current, high response-speed, and high photosensitivity [183]. The developed p-i-n devices are mainly fabricated by mesa-type technology, due to its simplicity. However, many problems may arise in these structures. Basically, reliability in photodetectors is determined by a number of factors as material quality, processing procedures, and amount of leakage current. In poor quality materials, crystal defects may strongly increase the dark current. Device processing, planar technology versus mesa technology, is crucial in photodetectors reliability, strongly affecting the leakage current. Indeed, mesa photodiode typically is formed by wet chemical etching of an epitaxial grown p-n structure, while in a planar process, a p-n junction is formed by diffusing a suitable *p* or *n* dopant in the substrate (Fig. 6.1). Planar structure is reported to be more reliable than a mesa since in a well-designed planar process the p-n junction is never exposed to ambient conditions. Exposure or impurities introduced during processing can cause surface corrosion, leading to an increase in the leakage current and poorer reliability, as a consequence. Alternative structures, as the planar ones, even if more complex, are necessary.

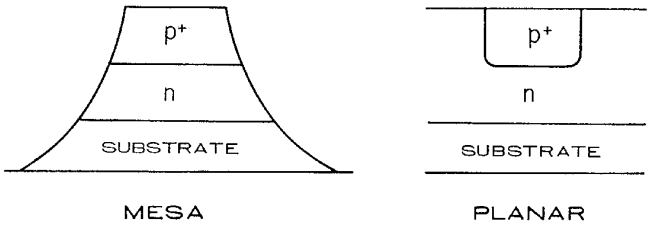

Fig. 6. 1 Sketch of a mesa and planar photodetector .

Local doping of SiC in a planar structure is performed by ion-implantation [184], since conventional diffusion techniques cannot be used, due to the small diffusivity of impurities in the material. Doping of SiC is easier in n-type case, since it is characterized by an almost complete electrical activation of the implanted dopant ions at the annealing temperature of 1500°C. Instead, p-type doping requires annealing at higher temperatures up to 1800°C in order to promote the electrical activation of the dopant in

substitutional lattice sites [185]. Therefore ion-implantation is the only technique suitable for selective doping with Al, B or N, P in SiC. In addition, doping concentrations and doping profiles can be precisely controlled and varied over a wide range. However, this process may introduce modifications in the surface morphology of SiC that, as a consequence, needs further treatment in order to avoid modifications in transport properties and electrical characteristics.

Therefore, on these preliminary remarks a p-i-n photodiode, realized by ion implantation and a complete planar technology, was first characterized and then its efficacy as a flame detector was proved.

6.2 P-i-n photodiode configuration

A 4H-SiC p-i-n configuration, structured in p-doped/intrinsic/n-doped layers, was considered. The device was fabricated at CNR-IMM Bologna defined using a completely planar technology, as reported elsewhere [184]. In particular, it was used a commercially available 8° off-axis n^+-type 4H-SiC substrate of 300 μm and conductivity equal to 0.021 Ω cm, at a doping concentration of $1 \cdot 10^{19}$ cm^{-3}. On it, an epilayer of 16.5 μm was grown (n-type concentration $3 \cdot 10^{15}$ cm^{-3}). The anode region (p^+-type; $1 \cdot 10^{18}$ cm^{-3}), 500 nm thick, was obtained by implantation of aluminum ions into the epilayer. Finally, circular ohmic contacts were made by deposition of Ti/Al and Ni on the p^+ implanted region and the n^+ back surface of the wafer, respectively, by means of a photo-lithography process. The sketch of the analyzed structure is shown in Fig. 6.2.

The p-i-n diode was firstly characterized, as previously reported (Chapter 5) by means of Raman spectroscopy in order to investigate the three different layers and evaluate their structure and quality. Then, Ti/Al top contact and Ni back contact were opportunely wire bonded in order to perform measurement tests.

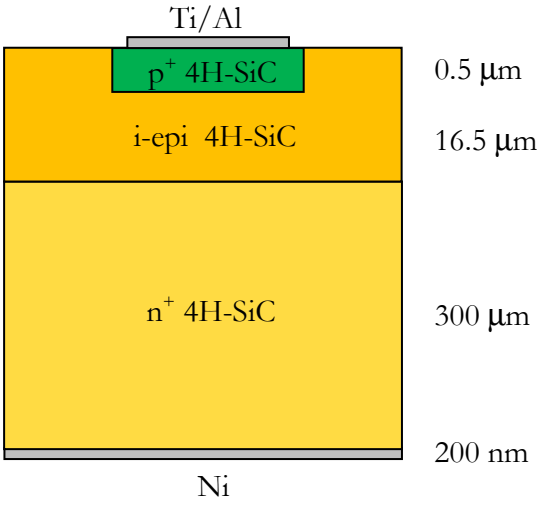

Fig. 6. 2 Schematic structure of the 4H-SiC p-i-n photodiode.

6.3 Characterization of 4H-SiC p-i-n photodiode

The electrical properties of the p-i-n device were studied at room temperature, in both forward and reverse bias. A characterization system composed of a semiconductor parameter analyzer AGILENT 4155C and a Probe Station MPS150 was used to this purpose. A maximum reverse bias of 60V was applied to the diode.

Being known the active area of the photodiode ($7.21 \cdot 10^{-4}$ cm^2), the J-V characteristics were registered. The current density is firstly reported vs forward (0-5 V) and reverse bias (0-60 V), under dark conditions to avoid any kind of light interference.

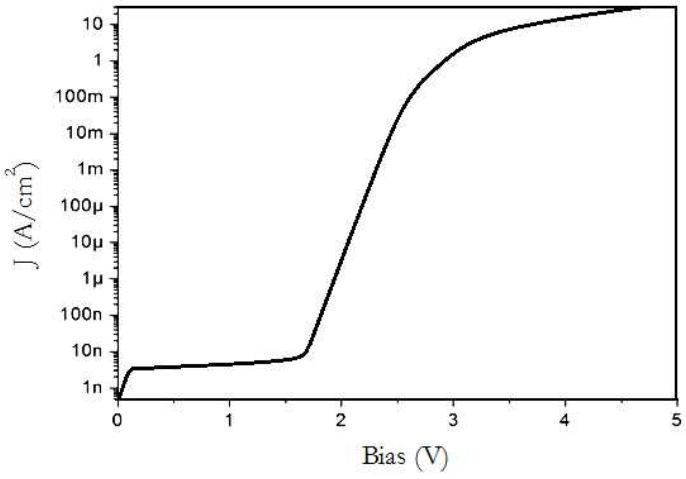

Fig. 6. 3 J-V characteristic of the p-i-n diode in forward bias.

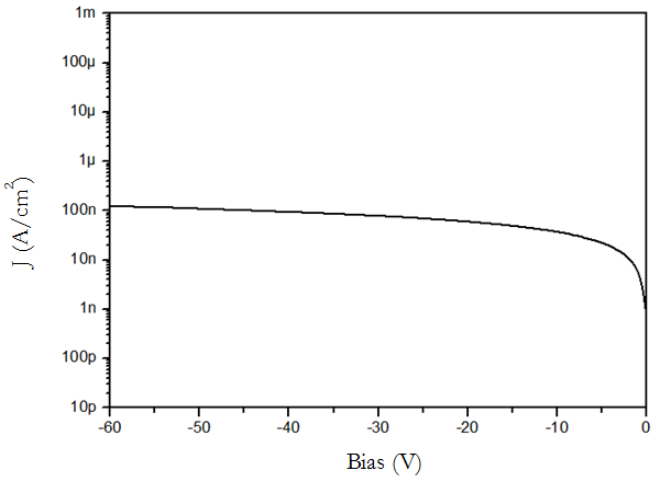

Fig. 6. 4 J-V characteristic of the p-i-n diode in reverse bias.

Diode dark currents are plotted in Fig. 6.3 and Fig. 6.4, in forward and reverse bias, respectively. When the diode is forward biased at 5 V the measured dark current density is equal to 27.63 A/cm^2. In reverse bias, when applied voltage is increased from 0.5 to 6 V, the dark current density increases from 1.80 nA/cm^2 (1.2 pA) up to 26 nA/cm^2 at 6V (18.7 pA). For applied reverse bias values between 6 and 60 V, the dark current density slowly increases to 120 nA/cm^2 (87.8 pA) at 60 V. The registered values of current were below those reported in literature for similar devices [145]. Indeed, Chen et al. [145] reported an increment of the dark current from 0.3 pA to 2 nA when the applied reverse bias was increased from 0.5 to 6 V. The higher current values may be ascribed to the different structure of the p-i-n diodes, planar or mesa. Likely, compared to a planar device, the mesa diode has a more defective junction, which underwent a chemical etching process during fabrication, and is moreover exposed to air. As a consequence this may result in the generation of a dark current higher than that reported for the analyzed planar p-i-n. Furthermore, as reported in Chapter 5, the good crystalline quality of the 4H-SiC p-i-n structure was proven by Raman spectroscopy.

The photo-response characteristics of the 4H-SiC UV p-i-n detector were then measured and analyzed. The UV light from a Xenon lamp was dispersed through a monochromator and focused onto the detector photoactive window by a lens. The wavelengths of the incidence light were

set in the range from 225 nm to 400 nm and increased in steps of 5 nm. The incident light power was calibrated by a DET210 high-speed silicon detector.

The photo-generated current density values of the photodiode, recorded for the considered wavelength range and under no bias, is firstly reported (Fig. 6.5).

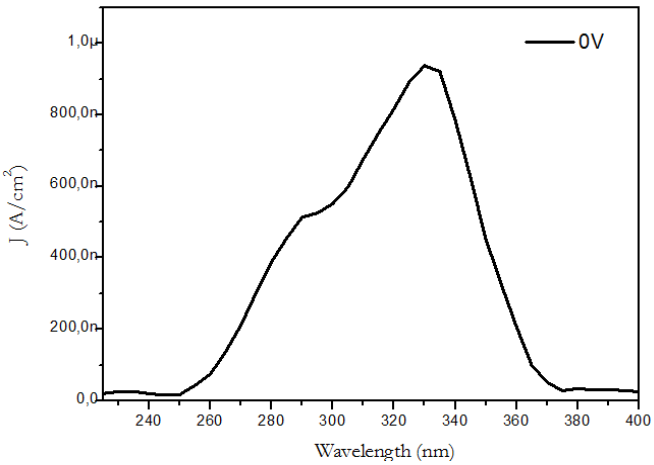

Fig. 6. 5 Photogenerated current density reported towards the analyzed wavelength range.

In order to test the photodiode response, reverse bias was only considered. As shown in the graph of Fig. 6.6, the J-V characteristic is prevalently flat over the analyzed voltage range under illuminated conditions. The integral of the photogenerated current density, in the analyzed spectral range, is reported on account of the total incident power density, $8.5 \cdot 10^{-5}$ W/cm^2.

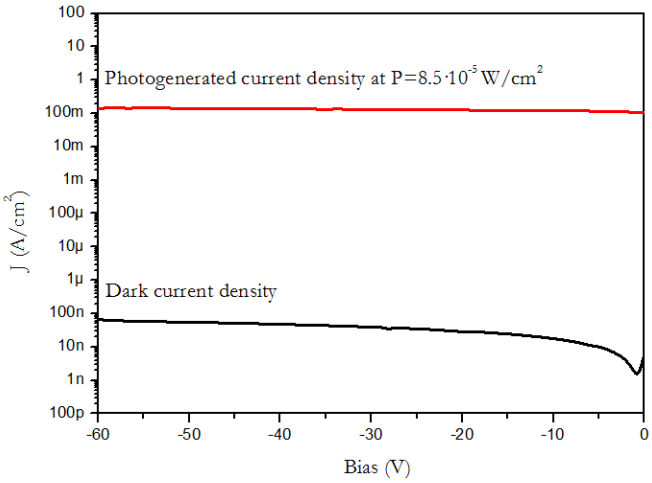

Fig. 6. 6 Reverse bias characteristic of the photodiode under dark and illumination conditions, at a power density P=8.5 10^{-5} W/cm^2

A related figure of merit for detectors is the spectral responsivity, which is the ratio of photocurrent to the incident optical power, as previously defined in Chapter 4:

$$R=\frac{I_p}{P_{opt}} \qquad (6.\ 1)$$

I_p is the photogenerated current calculated being known the voltage drop across the resistor (load resistance R_{load}=100 kΩ), considered in the equivalent circuit of the photodiode (Fig. 6.7).

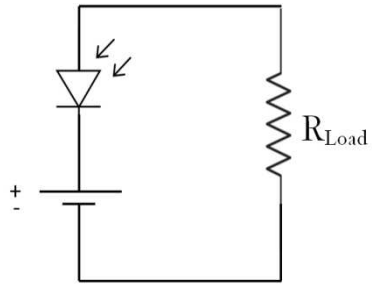

Fig. 6. 7 Equivalent operating circuit of the p-i-n photodiode.

The photodiode absorbs radiation similar to a cut-off filter. The wavelength of cut-off (λ_c) is established by the energy bangap of the semiconductor. In the case of 4H-SiC material it is λ_c=0.380 nm. Bearing in mind that the energy of photons decreases with increasing wavelength, and that near λ_c the photocurrent decreases abruptly, it can be understood that the curve of the spectral responsivity versus wavelength in the ideal case has a triangular shape [186].

The measured spectral responsivities of the 4H-SiC p-i-n diode under different reverse biases are shown in Fig. 6.8 a. The incident power density is reported in Fig. 6.8 b. Responsivities resulting from 0V and -10 V biases are compared. The photodetector shows a peak response wavelength at 300 nm and a cut-off wavelength at 380 nm. In particular, at the maximum peak response wavelength, the spectral peak responsivity reached 0.262 A/W at 0V and 0.310 A/W at -10V. The slight variation of the responsivity with reverse voltage may be attributed to the widening of the depletion zone with increasing reverse voltage, which increases the active volume of the photodiode. Analogous findings were reported by Chen et al [145]. Moreover

the calculated responsivity resulted to be higher than that reported in the literature for similar devices [145, 183].

The measured spectral characteristics implied that the fabricated photodetector has a highly improved ultraviolet to visible rejection, which makes it absolutely blind to visible/IR backgrounds.

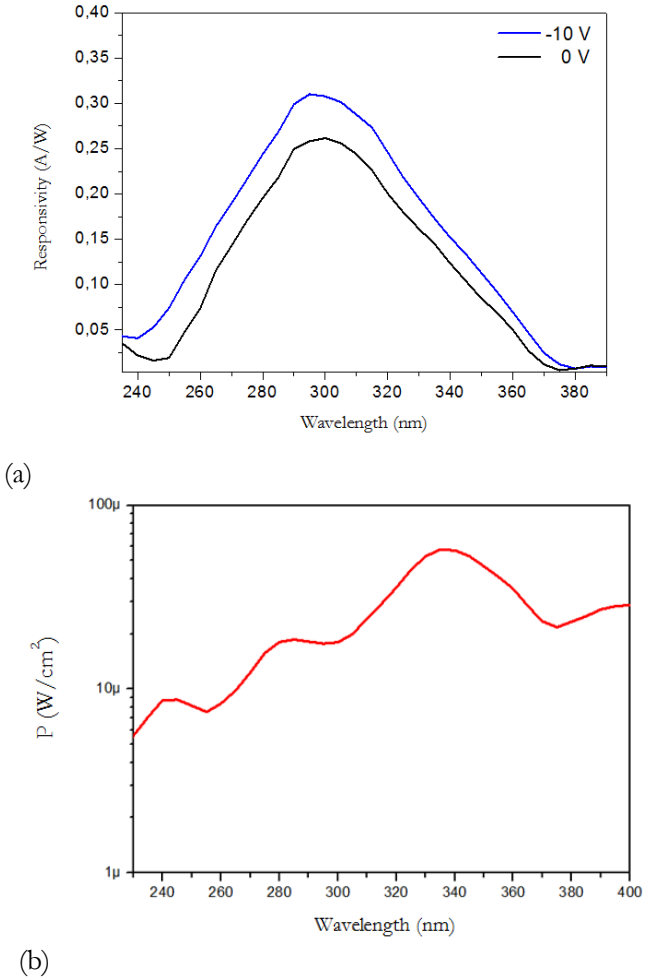

Fig. 6. 8 (a) Responsivity of 4H-SiC p-i-n photodetector under reverse biases of 0V and -10V. (b) Incident power density.

The electrical characteristics of the device were also measured as a function of temperature. An Hot Plate PC-420D was used for this purpose. The device response was tested from room temperature (25°C) up to 350°C. The measurements were performed under dark conditions, in reverse and forward bias. Curves are shown in Fig. 6.9 and Fig. 6.10.

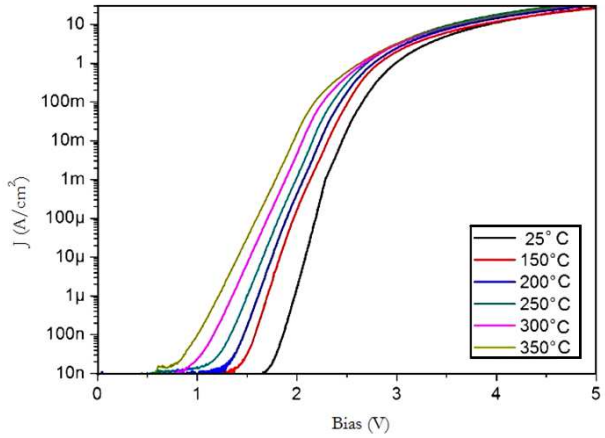

Fig. 6. 9 J-V characteristics of the p-i-n photodiode in forward bias. Curves are registered in the temperature range 25-350°C.

As can be observed from the carried out measurements, in forward bias, between 0 V and 5 V, the J-V characteristics display increasing current values and lower threshold voltages upon increasing temperature. On the other hand, in reverse bias 0-100 V the response is that reported in Fig. 6.10.

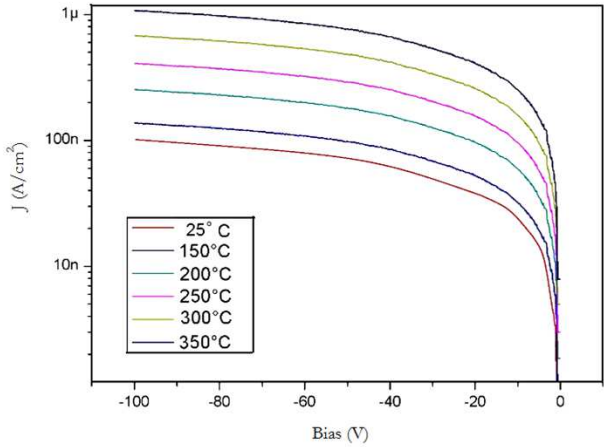

Fig. 6. 10 J-V characteristics of the p-i-n photodiode in reverse bias. Curves are registered in the temperature range 25-350°C.

As expected and in accordance with literature data [183], the dark current slowly increases with temperature, mostly due to the increase in the thermally ionized carrier concentration. The dark current at 350°C is 184 pA at -10V and increases up to 625 pA at -60V.

The photoresponse of the photodiode at 0V bias was also investigated in the same temperature range. Fig. 6.11 displays the responsivity values versus temperature. Measurements were carried out at a fixed wavelength

value, equal to 300 nm, where the maximum photoresponse was previously registered. At room temperature, the recorded peak responsivity is 0.262 A/W. When temperature is increased up to 350°C, responsivity slightly increases to 0.299 A/W, at the same wavelength value. At the wavelength of interest (300 nm) a weak increase of the responsivity with increasing temperature is observed. This finding is in agreement with the literature, even if lower temperatures were investigated [183]. The enhanced responsivity at higher temperature may be ascribed [183, 148] to the increased phonon population that promotes the indirect transitions in 4H-SiC.

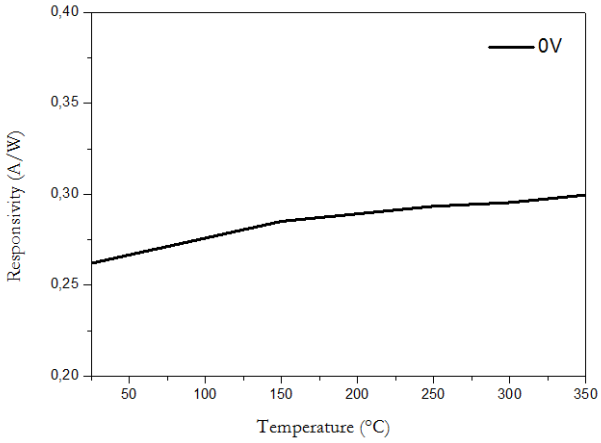

Fig. 6. 11 Responsivity values recorded at 300 nm under different temperature conditions.

These findings suggest that the fabricated 4H-SiC p-i-n photodiode, behind the visible/infrared blindness feature, results to be also suitable for UV detection in extreme temperature conditions where conventional silicon detectors usually fail.

6.3.1 Flame photodetector tests

The principle of operation of the investigated photodiode is the detection of the ultraviolet component of a flame. It is known that a flame emits a very broad spectrum of radiations, ranging from the ultraviolet to the infrared. When a flame is generated due to fire starting from hydrocarbons such as natural gas, UV radiations are emitted in the early stages that precede the development of the flame itself. Such radiations are readily detected by the sensor which, through appropriate associated electronics, will trigger an

output signal as an alarm warning. The revelation of the ultraviolet component is a certain proof of an instant generation of a flame.

It is also important to know exactly the main conditions which guarantee the detector to show the best performance in relation to its working distance and angular vision. Therefore, sensor response was also calculated and plotted for changing light source-to-photodiode distance. The result is displayed in Fig. 6.12.

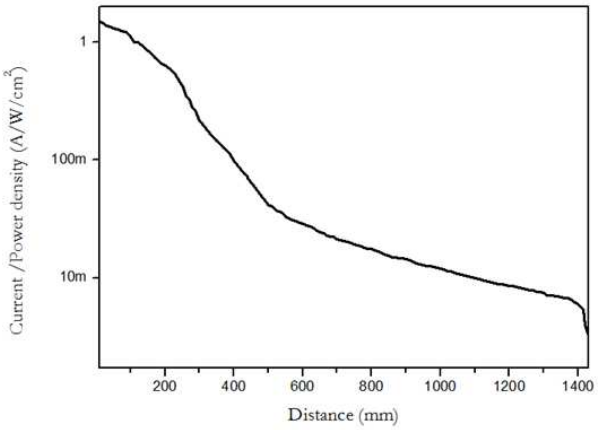

Fig. 6. 12 Sensor response at variable operating working distance.

The wavelength at which the maximum responsivity value was detected has been used for this purpose, namely 300 nm. Distances between 10 mm and 1430 mm were tested in steps of 10 mm. For each set distance, the photo-generated current was calculated by the detected voltage drop across the resistor on the device, as previously reported:

$$I_p = \frac{V}{R_{load}} \qquad (6.\ 2)$$

As evident, the photodiode response decreases by increasing the distance. The limit value of distance beyond which the diode does not give response any more is 1400 mm.

In addition, the photodiode response was investigated on account of different incidence angles of the light. At normal incidence conditions, light comes in perpendicular to the diode, whereas the light strikes the sample in a range of angles between -45 and 45 degrees under tilted incident conditions. The output voltage of the device was measured for different relative angles between the normal to photodiode surface and the incident light. Photo-

generated current was then calculated being known the load resistance, as previously reported. The measurements results are shown in Fig. 6.13.

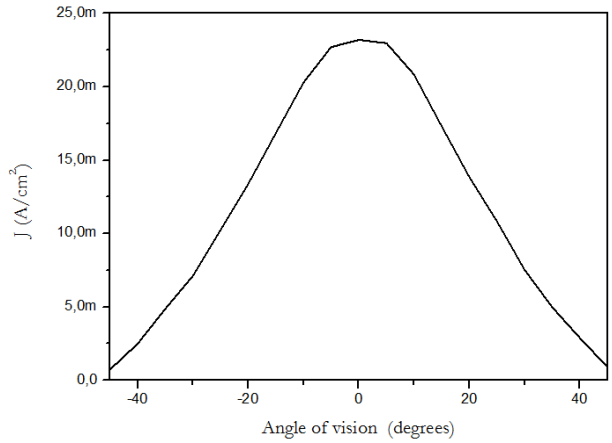

Fig. 6. 13 Photocurrent of the p-i-n photodiode generated at different incident angles.

As can be seen from the plot, response is better when the incident radiation is perpendicular to the photodiode sensitive surface (angle of vision equal to zero). As the relative angle is increased, the photocurrent decreases. When the incident radiation does not completely cover the entire active area of the device, the responsivity will fall off with the cosine of the angle of incidence as follows:

$$R_0 = R \cos\theta \qquad (6.\ 3)$$

where R is the responsivity at normal incidence.

6.4 ATLAS simulation of the p-i-n photodiode

Numerical modeling and simulations are useful for the analysis and optimization of electronic devices, especially if based on unconventional semiconductors, as the case of SiC. Therefore, a simulation program was used to outline the role of physical models and the related parameters in determining the electrical characteristics found in the experimental photodetector. Silvaco Atlas software [187] a commercial finite-element device simulator, was used for this purpose.

A minimum set of 4H-SiC specific properties data together with proper physical models were supplied by the program itself. P-i-n photodiode

experimental data and simulated characteristics were combined to study the main physical parameters affecting the device performance. The 4H-SiC electronic properties employed in the numerical simulation are summarized in Table 6.1. As to obtain the best agreement between experimental and simulative data, both literature data and fitting parameters were used [188].

Table 6. 1 Set of data employed in ATLAS simulation.

Simulation model parameters	
$E_g\ (eV)$	3.2
$v_s(cm^2/s)$	$2x10^7$
$N_i\ (cm^{-3})$	$2x10^{-8}$
$N_{n,p}(cm^{-3})$	$5x10^{-31}, 2x10^{-31}$
$E_A\ (eV)$	0.23
$E_D\ (eV)$	0.05
$\tau_{p,n}\ (s)$	$3x10^{-9}$
$C_{n,p}\ (cm^6/s)$	$5x10^{-31}, 2x10^{-31}$
$\mu_{\max\ n,p}\ (cm^2/V\ s)$	50, 20
$\mu_{\min\ n,p}\ (cm^2/V\ s)$	6, 2
$N_{crit\ n,p}\ (cm^{-3})$	$1x10^{16}$
$\alpha_{n,p}$	-0.5
$\beta_{n,p}$	-0.2
$\delta_{n,p}$	-1
$\gamma_{n,p}$	-7, 6

6.4.1 Physical models

The simulation process took into account physical models able to describe mobility, carrier lifetime as a function of both doping and temperature, bandgap temperature dependence and incomplete ionization of dopants.

The carrier mobilities were modeled with the Caughey -Thomas analytic model for 4H-SiC [189]:

$$\mu_{n,p}=\mu_{0n,p}^{min}\left(\frac{T}{300}\right)^{\alpha_{n,p}}+\frac{\mu_{0n,p}^{max}\left(\frac{T}{300}\right)^{\beta_{n,p}}-\mu_{0n,p}^{min}\left(\frac{T}{300}\right)^{\alpha_{n,p}}}{1+\left(\frac{T}{300}\right)^{\gamma_{n,p}}\left(\frac{N}{N_{n,p}^{crit}}\right)^{\delta_{n,p}}} \qquad (6.4)$$

where N is the doping density, $N_{n,p}^{crit}$ is the doping concentration at which the mobility is halfway between the mobility in highly doped and undoped material, α, β, δ, and γ are fitting parameters.

The carrier lifetimes useful to define the Shockley–Read–Hall (SRH) recombination rate are modeled as functions of doping and temperature by means of a relation derived by the Scharfetter's model [190]:

$$\tau_{n,p}=\frac{\tau_{0n,p}\left(\frac{T}{300}\right)^{\gamma}}{1+\left(\frac{N}{N_{n,p}^{SRH}}\right)^{k}} \quad (6.\ 5)$$

being N the total doping density, $N_{n,p}^{SRH}=7\cdot10^{16}$ cm^{-3} a reference constant, and τ_0 a process-dependent fitting parameter. The temperature dependence of the 4H-SiC band-gap is [191]:

$$E_g(T)=E_{g0}-\frac{\alpha T^2}{\beta+T} \quad (6.\ 6)$$

where $E_{g0}=3.2$ eV is the assumed band-gap energy at 300 K, $\alpha=3.3\cdot10^{-4}$ eV/K and $\beta=0$ are specific material parameters and T is the lattice temperature. An apparent band-gap narrowing effect as a function of the activated doping in the p-type and n-type regions, i.e. ΔE_a and ΔE_d respectively, is also included during the simulations according to the Lindefelt's model of the band edge displacements [192]:

$$\Delta E_{ga}=A_a\left(\frac{N_a^-}{10^{18}}\right)^{1/2}+B_a\left(\frac{N_a^-}{10^{18}}\right)^{1/3}+C_a\left(\frac{N_a^-}{10^{18}}\right)^{1/4} \quad (6.\ 7)$$

$$\Delta E_{gd}=A_d\left(\frac{N_d^+}{10^{18}}\right)^{1/2}+B_d\left(\frac{N_d^+}{10^{18}}\right)^{1/3}+C_d\left(\frac{N_d^+}{10^{18}}\right)^{1/4} \quad (6.\ 8)$$

where $A_{a,d}$, $B_{a,d}$ and $C_{a,d}$, are appropriate 4H-SiC constants.

As regards the incomplete ionization, due to the wide bandgap of 4H-SiC, not all doping atoms can be assumed as fully activated. Using the Fermi–Dirac statistics, the carrier concentration $N_a^-$and N_d^+ (i.e. the number of ionized acceptors and donors) can be expressed as [193]:

$$N_A^- = \frac{N_A}{1+g_A \exp\left(\frac{E_A - E_{F_p}}{kT}\right)} \quad (6.9)$$

$$N_D^+ = \frac{N_D}{1+g_D \exp\left(\frac{E_{F_n} - E_D}{kT}\right)} \quad (6.10)$$

where, N_A and N_D are the p-type and n-type doping concentrations, E_a and E_d are the acceptor and donor energy levels, E_{Fn} and E_{Fp} are the quasi-Fermi energy levels for electrons and holes, whereas g_D and g_A are the appropriate degeneracy factors for the conduction and valence band [194].

6.4.2 Material and geometry definitions

The device was virtually fabricated in ATLAS following the previously sketched geometry and layers doping configuration (Fig. 6.2). The sizes of the p-i-n diode layers were reproduced as shown; the width of the device was established equal to 20 μm, whereas its depth, 1 μm, was set as default by the software.

The doping profile of the p-type region was considered Gaussian shaped with a peak doping of $1 \cdot 10^{18}$ cm^{-3} at the surface. The intrinsic and n-type doped layers were instead uniform in concentration (Table 6.2).

Table 6. 2 Doping concentration of p-i-n layers.

4H-SiC regions	Doping (cm^{-3})
p^+	$1 \cdot 10^{18}$
n^-	$3 \cdot 10^{15}$
n^+	$1 \cdot 10^{19}$

The device ohmic contacts were simulated by considering a layer of nickel on the back of the structure and a layer of aluminum, covering approximately the 80% of the top of the p-i-n. Contacts material parameters were considered as default by the software.

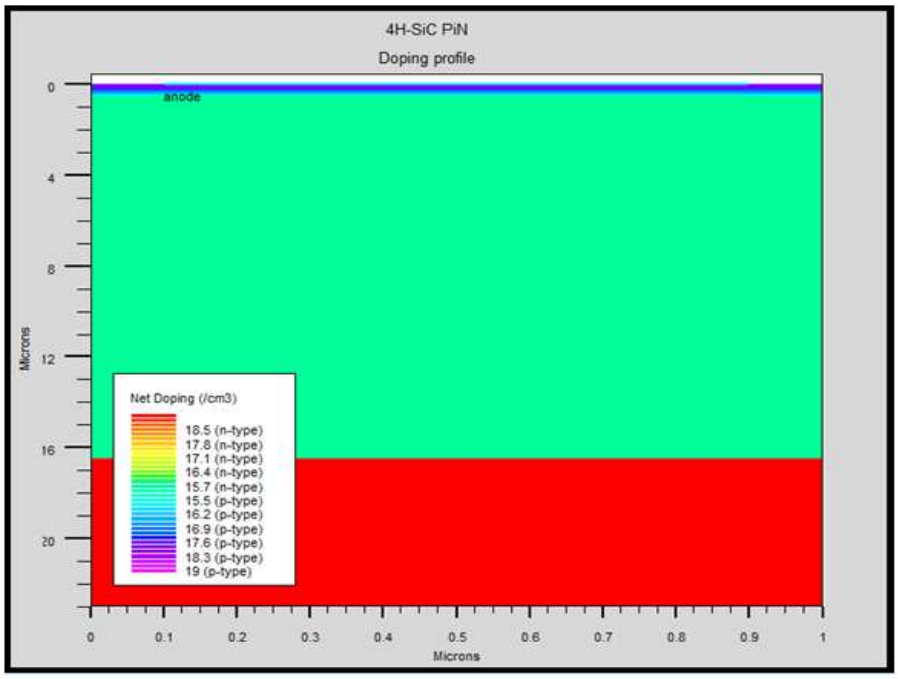

Fig. 6. 14 Cross-section of a selected region of the 4H-SiC p-i-n diode. Doping concentrations are shown.

6.4.3 Simulations of p-i-n characteristics

The measured J–V characteristics were imported and used for comparison to the ATLAS outputs. Simulated dark J-V characteristic was performed in forward bias. Fig. 6.16 shows the variation of dark current density with voltage as obtained both experimentally and from ATLAS simulation. It is clear that a good agreement has been achieved between experimental and simulated data.

As already stated in similar p–i–n structures [195], different current regimes can be determined. In particular, the current is dominated by carrier diffusion in the region (I) and recombination in the region (II). The diffusion and recombination current mechanisms produce a quick rise in slope, which is a characteristic of high quality, low resistance, and efficient operation. At voltages higher than 2.8 V, the plots tend to become flat and the current is entirely dominated by a series resistance (III) sum of the contact contributions and the diode internal resistance.

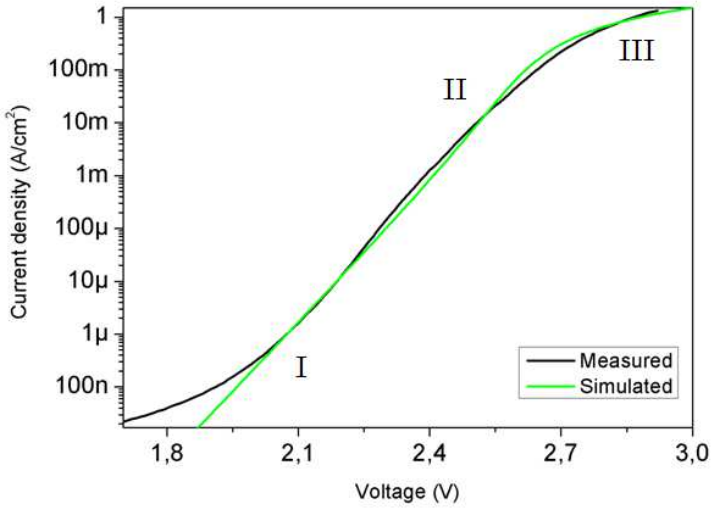

Fig. 6. 15 J-V characteristic in forward bias obtained from measured data and ATLAS simulation.

In order to investigate the performance of the p-i-n structure as a photodiode, the sensitivity of the photosensor to optical radiation of different wavelengths, in the UV range, was recorded. The optoelectronic simulator module "LUMINOUS" of ATLAS was used to simulate the electronic response to optical radiation. Basically, it is able to calculate optical intensity profiles within the semiconductor device, and to convert these profiles into photogeneration rates. The optical beam was properly modeled specifying the direction of propagation as a vertical illumination from the top. The beam was automatically split into a series of rays so that the sum of the rays covered the entire width of the illumination window.

Simulations were carried out in the UV spectral range, between 220 and 400 nm and a uniform and constant power of 1 $W/\mu m^2$ was set. Moreover, the experimental index of refraction of 4H-SiC obtained by spectroscopic ellipsometry (reported in Chapter 5) was imported and used together with the other material properties reported in Table 6.1. The simulated spectral responsivity, evaluated as the photocurrent-power ratio, is shown in Fig. 6.17. As reported in the experimental case, the simulated photodetector responsivity varies according to the operation wavelength, showing a maximum at 300 nm. The maximum of the simulated spectral response resulted quite in agreement with that experimentally measured.

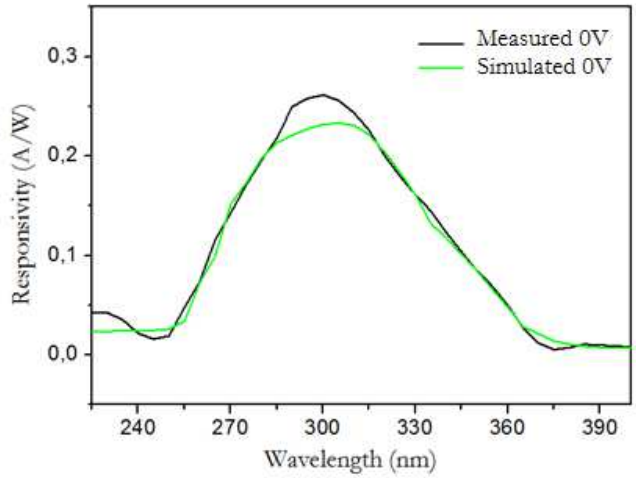

Fig. 6. 16 Comparison of responsivity curves obtained upon varying the operation wavelength for both measured and ATLAS simulated case.

Finally, the simulation of the responsivity curves was performed at different temperatures, as in the experimental case. In Fig. 6.18, responsivities obtained at 25°C and 350°C, respectively the lowest and highest investigated temperatures, are compared. Once again simulations are in agreement with experimental results. Indeed, at the maximum peak response (300 nm) the simulated responsivities show a similar behavior to those measured. A shift at the wavelength of interest, ascribed to the temperature effect, is observed even in this case. At room temperature responsivity value is 0.224 A/W and slightly increases to 0.236 A/W upon increasing temperature up to 350°C.

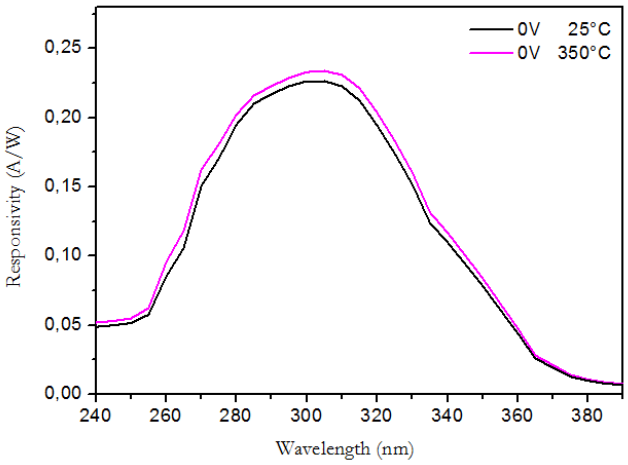

Fig. 6. 17 Comparison of responsivity curves obtained at 25°C and 350°C from ATLAS simulation.

CONCLUSIONS

In summary, this thesis was aimed at providing a contribute in the sensing devices research field. Recently the choice of alternative materials and advanced technologies to realize sensing structures allowed to greatly improve the existing devices, leading to a further miniaturization of the sensors and their easier integration with microelectronics. Indeed, carbon-based materials, characterized by outstanding electrical properties, have been recently introduced as a possible alternative to the traditional ones for niche applications. Moreover their nanostructured configuration seems to be particularly suitable for sensing applications thanks to the high surface to volume ratio.

In this work, graphene and carbon nanotubes-oxide composites were properly synthesized and their properties suitably tailored to sensing applications. A detail characterization of the obtained products was also performed by means of complementary techniques. Along with low dimensional carbon materials, even bulk carbon, in the form of silicon carbide, was investigated because of its potentialities in specific electronic devices.

A graphene/silicon Schottky diode was electrically characterized and tested as sensor of gaseous analytes detecting small traces of gas in a real environment. Indeed the device was able to work at room temperature and at 50% of relative humidity, and was able to detect very low concentrations of ammonia. It shows a strong specificity towards this analyte and sensor performances appear extremely stable and repeatable. Moreover very fast recovery times, at room temperature without resorting to techniques such as thermal annealing or exposure to UV radiation, were reported.

The development of the Metal Oxide Semiconductor sensor, based on the CNT/TiO_2/Pt nanohybrid, provided the detection of H_2 in air. The device was characterized by good response, selectivity, small size and low cost. Furthermore, it was even able to work at relative low temperature, with

a reduced power consumption. The prominent role of the synergic action among all the components of the synthesized nanohybrid was inferred, even if not completely clarified.

The electrochemical sensor, suitable for H_2O_2 sensing was based on the same CNT/TiO_2/Pt material of the MOS device. The versatility of the synthesized nanohybrid was therefore proved considering its performances even towards a liquid analyte as H_2O_2. The electrochemical sensor resulted particularly appealing in terms of fabrication simplicity, fast response, reliability, repeatability and low cost. What is more important a great selectivity was also proved.

The realized chemical devices have shown substantial advantages in terms of detectable concentrations, recovery times and selectivity, compared to the available sensors.

Finally, a 4H-SiC p-i-n structure was characterized as a photodiode and proved to act as an UV optical sensor. SiC excellent properties, such as the wide band gap and the physical stability, have been exploited to this purpose. The photodiode, working as a flame detector, resulted particularly suitable in a specific range of wavelengths and in harsh environments, especially under high temperature conditions. More insights on the physics of the device were also provided by means of simulation methods.

References

[1] Hulanicki A., et al., Chemical sensors: definitions and classification, Pure and Applied Chemistry 63 (1991) 1247-1250.

[2] Lilienfeld E.J., Method and apparatus for controlling electric currents, U.S. Patent No. 1,745,175. 28 Jan. 1930.

[3] Sze. S., Physics of Semiconductor Devices, Wiley-Interscience publication, John Wiley & Sons, 1981.

[4] Shivaraman M. S., et al., Hydrogen sensitivity of palladium–thin-oxide–silicon schottky barriers, Electronics Letters 12 (1976) 483-484.

[5] Ito K., Hydrogen-sensitive Schottky barrier diodes, Surface Science 86 (1979) 345-352.

[6] Potje-Kamloth K., Semiconductor junction gas sensors, Chemical reviews 108 (2008) 367-399.

[7] Tongay S., et al., Graphene/GaN Schottky diodes: Stability at elevated temperatures, Applied Physics Letters 99 (2011) 102102.

[8] Kim H.Y., et al., Chemically modulated graphene diodes, Nano letters 13 (2013) 2182-2188.

[9] Uddin M.A., et al., Functionalized graphene/silicon chemi-diode H2 sensor with tunable sensitivity, Nanotechnology 25 (2014) 125501.

[10] Di Bartolomeo A., Graphene Schottky diodes: An experimental review of the rectifying graphene/semiconductor heterojunction, Physics Reports 606 (2016) 1-58.

[11] Rhoderick E.H., and Williams. R.H., Metal-semiconductor contacts, Vol. 129. Oxford: Clarendon Press, 1988.

[12] Sze. S., Semiconductor Devices: Physics and Technology, 2a ed. John Wiley & Sons, Limited, 1985.

[13] Tung R.T., Electron transport of inhomogeneous Schottky barriers, Applied physics letters 58 (1991) 2821-2823.

[14] Cheung S. K., and Cheung N. W., Extraction of Schottky diode parameters from forward current-voltage characteristics, Applied Physics Letters 49 (1986) 85-87.

[15] Fine G.F., et al., Metal oxide semi-conductor gas sensors in environmental monitoring, Sensors 10 (2010) 5469-5502.

[16] Brattain W.H., and Bardeen J., Surface properties of germanium, Bell System Technical Journal 32 (1953) 1-41.

[17] Seiyama T., and Kagawa S., Study on a Detector for Gaseous Components Using Semiconductive Thin Films, Analytical Chemistry 38 (1966) 1069-1073.

[18] Taguchi N., Semiconductor gas detecting device, U.S. Patent No. 3,732,519. 8 May 1973.

[19] Neri G., First Fifty Years of Chemoresistive Gas Sensors, Chemosensors 3 (2015) 1-20.

[20] Elmi I., et al., Development of ultra-low-power consumption MOX sensors with ppb-level VOC detection capabilities for emerging applications, Sensors and Actuators B: Chemical 135 (2008) 342-351.

[21] Jun Y.K., et al., High H 2 sensing behavior of TiO 2 films formed by thermal oxidation, Sensors and Actuators B: Chemical 107 (2005) 264-270.

[22] De Luca L., et al., Hydrogen sensing characteristics of Pt/TiO 2/MWCNTs composites, International journal of hydrogen energy 37 (2012) 1842-1851.

[23] Santangelo S., et al., On the hydrogen sensing mechanism of Pt/TiO 2/CNTs based devices, Sensors and Actuators B: Chemical 178 (2013) 473-484.

[24] Wang C., et al., Metal oxide gas sensors: sensitivity and influencing factors, Sensors 10 (2010) 2088-2106.

[25] Pitcher S., et al., Current/voltage characteristics of a semiconductor metal oxide gas sensor, Sensors and Actuators B: Chemical 93 (2003) 454-462.

[26] Naisbitt S.C., et al., A microstructural model of semiconducting gas sensor response: The effects of sintering temperature on the response of chromium titanate (CTO) to carbon monoxide, Sensors and Actuators B: Chemical 114 (2006) 969-977.

[27] Bolis V., Fundamentals in Adsorption at the Solid-Gas Interface, Concepts and Thermodynamics." Calorimetry and Thermal Methods in Catalysis, Springer Berlin Heidelberg (2013) 3-50.

[28] Power A.C., and Morrin A., Electroanalytical sensor technology, INTECH Open Access Publisher, 2013.

[29] Qiu J., et al., Recent applications of TiO 2 nanomaterials in chemical sensing in aqueous media, Sensors and actuators B: Chemical 160 (2011) 875-890.

[30] Jiang L.C., et al., Electrodeposition of TiO2 nanoparticles on multiwalled carbon nanotube arrays for hydrogen peroxide sensing, Electroanalysis 21 (2009) 988-993.

[31] Daobao C., et al., Electrocatalytic oxidation, of glucose on carbon nanotube/nanocrystalline TiO2-polyaniline film loaded Pt complex electrode, CHINESE JOURNAL OF ANALYTICAL CHEMISTRY 34 (2006) 1269-1272.

[32] Grieshaber D., et al., Electrochemical biosensors-sensor principles and architectures, Sensors 8 (2008) 1400-1458.

[33] Liu C.C., Electrochemical sensors, Biomedical Engineering Handbook, CRC Press, Boca Raton Fla (1995) 758-763.

[34] Wang J., Analytical electrochemistry, John Wiley & Sons, 2006.

[35] Madduri N., Electrochemical capacitance measurements to study molecular surface interactions (2012).

[36] Bard A.J., et al., Electrochemical methods: fundamentals and applications, Vol. 2. New York: Wiley, 1980.

[37] Scholz F., Electroanalytical methods, Vol. 1. Berlin-Heidelberg: Springer, 2010.

[38] Strømme M., et al., Voltammetry on fractals, Solid state communications 96 (1995) 151-154.

[39] Bertolazzi S., et al., Exploring flatland: AFM of mechanical and electrical properties of graphene, MoS2 and other low-dimensional materials, Microsc. Anal 27 (2013) 21-24.

[40] Butler S. Z., et al., Progress, challenges, and opportunities in two-dimensional materials beyond graphene, ACS nano 7 (2013) 2898-2926.

[41] Pan L. S. and Don R. K., eds. Diamond: electronic properties and applications, Springer Science & Business Media, 2013.

[42] Torres L.E.F., et al., Introduction to graphene-based nanomaterials: from electronic structure to quantum transport, Cambridge University Press, 2014.

[43] Schedin F., et al.,Detection of individual gas molecules adsorbed on graphene, Nature materials 6 (2007) 652-655.

[44] Kong J.M. et al., Functionalized carbon nanotubes for molecular hydrogen sensors, Advanced Materials 13 (2001) 1384-1386.

[45] Bianco A., et al., Applications of carbon nanotubes in drug delivery, Current opinion in chemical biology 9 (2005) 674-679.

[46] Qian M., et al., Electron field emission from screen-printed graphene films, Nanotechnology 20 (2009) 425702.

[47] Bonaccorso F., et al., Graphene photonics and optoelectronics, Nature photonics 4 (2010) 611-622.

[48] Geim A. K. and K. S. Novoselov, The rise of graphene, Nature materials 6 (2007) 183-191 .

[49] Eizenberg J. and Blakely M., Carbon interaction with nickel surfaces: Monolayer formation and structural stability, The Journal of Chemical Physics 71 (1979) 3467-3477 .

[50] Bohem H.P., et al.,Nomenclature and terminology of graphite intercalation compounds (IUPAC Recommendations 1994), Pure and Applied Chemistry 66 (1994) 1893-1901.

[51] Mermin, N.D., Crystalline Order in Two Dimensions, Physical Review 176 (1968) 250.

[52] Novoselov K.S., et al., Electric field effect in atomically thin carbon films, Science 306 (2004) 666-669.

[53] Novoselov, K.S., et al., Two-dimensional gas of massless Dirac fermions in graphene, Nature 438 (2005) 197-200.

[54] Avouris P.,Graphene: electronic and photonic properties and devices, Nano letters 10 (2010) 4285-4294.

[55] Neto AH C., et al., The electronic properties of graphene, Reviews of

modern physics 81 (2009) 109.

[56] Geim A.K. and A.H. MacDonald, Graphene: exploring carbon flatland, Physics today 60 (2007) 35.

[57] Allain P. E., et al., Klein tunneling in graphene: optics with massless electrons, The European Physical Journal B 83 (2011) 301-317.

[58] Lin Y.M., et al, 100-GHz transistors from wafer-scale epitaxial graphene, Science 327 (2010) 662-662.

[59] Novoselov K. S., et al., Room-temperature quantum Hall effect in graphene, Science 315 (2007) 1379-1379.

[60] Katsnelson M. I., et al., Chiral tunnelling and the Klein paradox in graphene, Nature physics 2 (2006) 620-625.

[61] Nair R., et al., Fine structure constant defines visual transparency of graphene, Science 320 (2008) 1308.

[62] Hamberg I, et al., Evaporated Sn-doped In2O3 films: Basic optical properties and applications to energy-efficient windows, Journal of Applied Physics 60 (1986) 123-160.

[63] Lee C., et al.,Measurement of the elastic properties and intrinsic strength of monolayer graphene, Science 321 (2008) 385-388.

[64] Balandin A.A., et al., Superior thermal conductivity of single-layer graphene, Nano letters 8 (2008) 902-907.

[65] Liu H., et al., Chemical doping of graphene, Journal of materials chemistry 21 (2011) 3335-3345.

[66] Hill E.W.,et al., Graphene sensors, Sensors Journal, IEEE 11 (2011) 3161-3170.

[67] Iijima S., Helical microtubules of graphitic carbon, Nature 354 (1991) 56-58.

[68] Dresselhaus M. S., et al., Physics of carbon nanotubes, Carbon 33 (1995) 883-891.

[69] Dresselhaus M. S., et al., Raman spectroscopy of carbon nanotubes, Physics reports 409 (2005) 47-99.

[70] Wilder J. W.G., et al., Electronic structure of atomically resolved carbon nanotubes, Nature 391 (1998) 59-62.

[71] Javey A. and Kong J., Carbon nanotube electronics, Springer Science & Business Media, 2009.

[72] Kane C. L. and Mele E.J., Size, shape, and low energy electronic structure of carbon nanotubes, Physical Review Letters 78 (1997) 1932.

[73] Ruoff R. S., et al., Mechanical properties of carbon nanotubes: theoretical predictions and experimental measurements, Comptes Rendus Physique 4 (2003) 993-1008.

[74] Kong J., et al., Nanotube molecular wires as chemical sensors, Science 287 (2000) 622-625.

[75] Li J., et al., Carbon nanotube sensors for gas and organic vapor detection, Nano Letters 3 (2003) 929-933.

[76] Bonaccorso F., et al., Production and processing of graphene and 2d

crystals, Materials Today 15 (2012) 564-589.

[77] La Via F.,et al., Mechanisms of growth and defect properties of epitaxial SiC, Applied Physics Reviews 1 (2014) 031301.

[78] Emtsev K. V., et al., Towards wafer-size graphene layers by atmospheric pressure graphitization of silicon carbide, Nature materials 8 (2009) 203-207.

[79] Coleman J. N., Liquid exfoliation of defect-free graphene, Accounts of chemical research 46 (2012) 14-22.

[80] Santangelo S., et al., Taguchi optimized synthesis of graphene films by copper catalyzed ethanol decomposition, Diamond and Related Materials 41 (2014) 73-78.

[81] Faggio G., et al., Fast growth of polycrystalline graphene by chemical vapor deposition of ethanol on copper." Nanotechnology Materials and Devices Conference (NMDC), 2014 IEEE 9th. IEEE, 2014.

[82] Capasso A., et al., Nitrogen-doped graphene films from chemical vapor deposition of pyridine: influence of process parameters on the electrical and optical properties, Beilstein journal of nanotechnology 6 (2015) 2028-2038.

[83] Li X., et al., Large-area synthesis of high-quality and uniform graphene films on copper foils, Science 324 (2009) 1312-1314.

[84] Li X., et al., Evolution of graphene growth on Ni and Cu by carbon isotope labeling, Nano letters 9 (2009) 4268-4272.

[85] Reina A., et al., Large area, few-layer graphene films on arbitrary substrates by chemical vapor deposition, Nano letters 9 (2008) 30-35.

[86] Choi D. S., et al., Effect of Cooling Condition on Chemical Vapor Deposition Synthesis of Graphene on Copper Catalyst, ACS applied materials & interfaces 6 (2014) 19574-19578.

[87] Ahn Y.,et al., Procedure of removing polymer residues and its influences on electronic and structural characteristics of graphene, Applied Physics Letters 102 (2013) 091602.

[88] Capasso A., et al., Cyclododecane as support material for clean and facile transfer of large-area few-layer graphene, Applied Physics Letters 105 (2014) 113101 .

[89] Ago H., et al., Gas analysis of the CVD process for high yield growth of carbon nanotubes over metal-supported catalysts, Carbon 44 (2006) 2912-2918.

[90] Raman C.V. and Krishnan K. S., A new type of secondary radiation, Nature 121 (1928) 501-502.

[91] Califano S., Vibrational states, John Wiley & Sons, 1976.

[92] Le Ru E., and Etchegoin P., Principles of Surface-Enhanced Raman Spectroscopy: and related plasmonic effects, Elsevier, 2008.

[93] Ferrari A.C. and Robertson J.F., Interpretation of Raman spectra of disordered and amorphous carbon, Physical review B 61 (2000) 14095.

[94] Ferrari, A. C., et al., Raman spectrum of graphene and graphene layers, Physical review letters 97 (2006) 187401.

[95] Malard L. M., et al., Raman spectroscopy in graphene, Physics Reports 473 (2009) 51-87.

[96] Edwards D.F., Raman scattering in crystals, UCID-21510, Lawrence Livermore National Laboratory, Livermore, Calif (1988).

[97] Hayes W., and Loudon R., Scattering of light by crystals, Courier Corporation, 2012.

[98] Basko D. M., et al., Electron-electron interactions and doping dependence of the two-phonon Raman intensity in graphene, Physical Review B 80 (2009) 165413.

[99] Ferrari A. C., and Basko D. M., Raman spectroscopy as a versatile tool for studying the properties of graphene, Nature nanotechnology 8 (2013) 235-246.

[100] Santangelo S., et al., Micro-Raman Analysis of Three-Dimensional Macroporous Sponge-Like Network of Carbon Nanotubes under Tension, The Journal of Physical Chemistry C 118 (2014) 13912-13919.

[101] Di Leo R.A., et al., Purity assessment of multiwalled carbon nanotubes by Raman spectroscopy, Journal of Applied Physics 101 (2007) 064307.

[102] Milone C., et al., Influence of the Cobalt Phase on the Highly Efficient Growth of MWNTs, Nanomaterials and Nanotechnology 4 (2014).

[103] Faggio G., et al., High-temperature growth of graphene films on copper foils by ethanol chemical vapor deposition, The Journal of Physical Chemistry C 117 (2013) 21569-21576.

[104] Fedi F. et al., A study on the physicochemical properties of hydroalcoholic solutions to improve the direct exfoliation of natural graphite down to few-layers graphene, Materials Research Express 2 (2015) 035601.

[105] Polichetti T., et al., Graphene-Si Schottky diode in environmental conditions at low NH 3 ppm level, Nanotechnology Materials and Devices Conference (NMDC), 2014 IEEE 9th. IEEE, 2014.

[106] Eckmann A., et al., Probing the nature of defects in graphene by Raman spectroscopy, Nano letters 12 (2012) 3925-3930.

[107] Torrisi F., et al., Inkjet-printed graphene electronics, Acs Nano 6 (2012) 2992-3006.

[108] Khan U., et al. "High-Concentration Solvent Exfoliation of Graphene, Small 6 (2010) 864-871.

[109] Zhang Y. H., et al. Improving gas sensing properties of graphene by introducing dopants and defects: a first-principles study, Nanotechnology 20 (2009) 185504.

[110] Malara A., et al., Origin of the different behavior of some platinum decorated nanocarbons towards the electrochemical oxidation of hydrogen peroxide, Journal of Electrochemical Society, under review.

[111] Frontera P., et al., Characterisation and H2O2 sensing properties of TiO2-CNTs/Pt electro-catalysts, Materials Chemistry and Physics 170 (2016) 129-137.

[112] Kamat P. V. TiO2 nanostructures: recent physical chemistry advances,

The Journal of Physical Chemistry C 116 (2012) 11849-11851.

[113] Wu J., et al., An ultraviolet responsive hybrid solar cell based on titania/poly (3-hexylthiophene), Scientific reports 3 (2013).

[114] Marichy C., et al. Gas sensing properties and p-type response of ALD TiO2 coated carbon nanotubes, Nanotechnology 26 (2015) 024004.

[115] Frontera P., et al, A new approach to the synthesis of titania nano-powders enriched with very high contents of carbon nanotubes by electro-spinning, Materials Chemistry and Physics 153 (2015) 338-345.

[116] Gupta S. K., et al., Titanium dioxide synthesized using titanium chloride: size effect study using Raman spectroscopy and photoluminescence, Journal of Raman Spectroscopy 41 (2010) 350-355.

[117] Inoue F., et al., Raman evidence of the interaction between multiwalled carbon nanotubes and nanostructured TiO2, Journal of Raman Spectroscopy 42 (2011) 1379-1383.

[118] Murphy H. P. et al., Raman study of multiwalled carbon nanotubes functionalized with oxygen groups, Journal of Vacuum Science & Technology B 24 (2006) 715-720.

[119] Hu Y., et al., Phase transformation of precipitated TiO2 nanoparticles, Materials Science and Engineering: A 344 (2003) 209-214.

[120] Polichetti T. et al. "Graphene-based Schottky Device Detecting NH 3 at ppm level in Environmental Conditions, Procedia Engineering 87 (2014) 232-235.

[121] Solanki C. S., Solar photovoltaics: fundamentals, technologies and applications, PHI Learning Pvt. Ltd., 2015.

[122] Lu C.S., et al., Investigation of film-thickness determination by oscillating quartz resonators with large mass load, Journal of Applied Physics 43 (1972) 4385-4390.

[123] Chen C. C., et al., Graphene-silicon Schottky diodes, Nano letters 11 (2011) 1863-1867.

[124] Tongay S., et al., Rectification at graphene-semiconductor interfaces: zero-gap semiconductor-based diodes, Physical Review X 2 (2012) 011002.

[125] Das A., et al, Monitoring dopants by Raman scattering in an electrochemically top-gated graphene transistor, Nature nanotechnology 3 (2008) 210-215.

[126] Yang H., et al, Graphene barristor, a triode device with a gate-controlled Schottky barrier, Science 336 (2012) 1140-1143.

[127] Yuan W., and Shi G., Graphene-based gas sensors, Journal of Materials Chemistry A 1 (2013) 10078-10091.

[128] Lu G., et al., Toward practical gas sensing with highly reduced graphene oxide: a new signal processing method to circumvent run-to-run and device-to-device variations, ACS nano 5 (2011) 1154-1164.

[129] Trocino S., et al., Pt-TiO2/MWCNTs hybrid composites for monitoring low hydrogen concentrations in air, Sensors 12 (2012) 12361-12373.

[130] Chen W., et al., Recent advances in electrochemical sensing for hydrogen peroxide: a review, Analyst 137 (2012) 49-58.

[131] Cañete-Rosales P., et al., Influence of size and oxidative treatments of multi-walled carbon nanotubes on their electrocatalytic properties, Electrochimica Acta 62 (2012) 163-171.

[132] He S., et al., A novel non-enzymatic hydrogen peroxide sensor based on poly-melamine film modified with platinum nanoparticles, RSC Advances 4 (2014) 45185-45190.

[133] Pang X., et al, An amperometric glucose biosensor fabricated with Pt nanoparticle-decorated carbon nanotubes/TiO 2 nanotube arrays composite, Sensors and Actuators B: Chemical 137 (2009) 134-138.

[134] Han K.N., et al., Development of Pt/TiO 2 nanohybrids-modified SWCNT electrode for sensitive hydrogen peroxide detection, Sensors and Actuators B: Chemical 174 (2012) 406-413.

[135] Monroy E., et al., Wide-bandgap semiconductor ultraviolet photodetectors, Semiconductor Science and Technology 18 (2003) R33.

[136] Omnès F., et al., Wide bandgap UV photodetectors: A short review of devices and applications, Integrated Optoelectronic Devices 2007, International Society for Optics and Photonics, 2007.

[137] Legres L.G., et al., The Laser Technology: New Trends in Biology and Medicine, Journal of Modern Physics 2014 (2014).

[138] Würtele M.A., et al., Application of GaN-based ultraviolet-C light emitting diodes–UV LEDs–for water disinfection, Water research 45 (2011) 1481-1489.

[139] Roming P.W.A., et al., The Swift ultra-violet/optical telescope, Space Science Reviews 120 (2005) 95-142.

[140] Mazzillo M., and Sciuto A., 4H-SiC Schottky photodiodes for ultraviolet flame detection, Journal of Instrumentation 10 (2015) P10029.

[141] Lindquist O. P. A., et al., Infrared to vacuum ultraviolet optical properties of 3C, 4H and 6H silicon carbide measured by spectroscopic ellipsometry, Thin solid films 455 (2004) 235-238.

[142] Bin C., et al., Simulation and optimization of a 6H-SiC metal-semiconductor-metal ultraviolet photodetector, Journal of Semiconductors 31 (2010) 064010.

[143] Hirabayashi Y., et al., High Temperature Characteristics for UV Responsivity of 3C-SiC pn Photodiode, Materials Science Forum. Vol. 615. 2009.

[144] Guo X., et al., Study of reverse dark current in 4H-SiC avalanche photodiodes, Quantum Electronics, IEEE Journal of 41 (2005) 562-567.

[145] Chen X.,et al., Visible blind p–i–n ultraviolet photodetector fabricated on 4H-SiC, Microelectronic engineering 83 (2006) 104-106.

[146] Kasap S., et al., An illustrated dictionary of optoelectronics and photonics: important terms and effects, Concise Second Student Edition Version 1.1 (2002).

[147] Hastings A.S., et al., Minimizing photodiode nonlinearities by compensating voltage-dependent responsivity effects, Journal of Lightwave Technology 28 (2010) 3329-3333.

[148] Cha H.Y., et al., Temperature dependent characteristics of nonreach-through 4H-SiC separate absorption and multiplication APDs for UV detection, Sensors Journal, IEEE 8 (2008) 233-237.

[149] Wilson J. and Hawkes J.F.B., Optoelectronics-an introduction, (1989).

[150] Kildemo M., Optical properties of silicon carbide polytypes below and around bandgap, Thin solid films 455 (2004) 187-195.

[151] Neudeck P. G., Progress in silicon carbide semiconductor electronics technology, Journal of Electronic Materials 24 (1995) 283-288.

[152] Jepps N. W., and Page T.F., Polytypic transformations in silicon carbide, Progress in crystal growth and characterization 7 (1983) 259-307.

[153] Ching W. Y., et al., The electronic structure and spectroscopic properties of 3C, 2H, 4H, 6H, 15R and 21R polymorphs of SiC, Materials Science and Engineering: A 422 (2006) 147-156.

[154] Kordina O., Growth and characterization of silicon carbide power device material (1994).

[155] Lebedev A.A., Deep level centers in silicon carbide: a review, Semiconductors 33 (1999) 107-130.

[156] Trew R. J., et al., The potential of diamond and SiC electronic devices for microwave and millimeter-wave power applications, Proceedings of the IEEE 79 (1991) 598-620.

[157] Tairov Y. M., et al., Investigation of growth processes of ingots of silicon carbide single crystals, Journal of crystal growth 43 (1978) 209-212.

[158] Kordina O., et al., High quality 4H-SiC epitaxial layers grown by chemical vapor deposition, Applied physics letters 66 (1995) 1373-1375.

[159] Zorman C. A., et al., Epitaxial growth of 3C–SiC films on 4 in. diam (100) silicon wafers by atmospheric pressure chemical vapor deposition, Journal of Applied Physics 78 (1995) 5136-5138.

[160] Casady J.B., and Wayne Johnson R., Status of silicon carbide (SiC) as a wide-bandgap semiconductor for high-temperature applications: A review, Solid-State Electronics 39 (1996) 1409-1422.

[161] Levinshtein M. E., et al., Properties of Advanced Semiconductor Materials: GaN, AIN, InN, BN, SiC, SiGe. John Wiley & Sons, 2001.

[162] Ask S., Density Functional Theory and Defects in semiconductors, Project Report (2000).

[163] Hopcroft M., et al., What is the Young's Modulus of Silicon?, Journal of Microelectromechanical Systems, 19 (2010) 229-238.

[164] Grundmann M., The physics of semiconductors: an introduction including devices and nanophysics, Springer Science & Business Media, 2006.

[165] BhatnagarM., and Baliga B.J., Comparison of 6H-SiC, 3C-SiC, and Si for power devices, Electron Devices, IEEE Transactions on 40 (1993)

645-655.

[166] Bechstedt F., et al., Polytypism and properties of silicon carbide, physica status solidi (b) 202 (1997) 35-62.

[167] Choyke W. J., et al., Optical properties of cubic SiC: luminescence of nitrogen-exciton complexes, and interband absorption, Physical Review 133 (1964) A1163.

[168] Liu X. F., et al. Vertical PIN ultraviolet photodetectors based on 4H-SiC homoepilayers, physica status solidi (c) 4 (2007) 1609-1612.

[169] Akturk A., et al. Comparison of 4H-SiC impact ionization models using experiments and self-consistent simulations, Journal of Applied Physics 104 (2008) 026101.

[170] Nowak S., Crystal lattice dynamics of various silicon-carbide polytypes, International Conference on Solid State Crystals 2000, International Society for Optics and Photonics, 2001.

[171] Fujiwara H., Spectroscopic ellipsometry: principles and applications, John Wiley & Sons, 2007.

[172] Malara A., Optical characterization of variously doped 4H-SiC for optoelectronic devices, submitted.

[173] Harima H., Raman scattering characterization on SiC, Microelectronic engineering 83 (2006) 126-129.

[174] Nakashima S.I. and Harima H., Raman investigation of SiC polytypes, physica status solidi (a) 162 (1997) 39-64.

[175] Burton J. C., et al., Spatial characterization of doped SiC wafers by Raman spectroscopy, Journal of Applied Physics 84 (1998) 6268-6273.

[176] Lin S., et al., Effect of impurities on the Raman scattering of 6H-SiC crystals, Materials Research 15 (2012) 833-836.

[177] Mermoux M., et al., Raman imaging analysis of SiC wafers, Materials Science Forum, 433 (2003).

[178] Canino A., et al., Large area optical characterization of 3 and 4 inches 4H–SiC wafers, Thin Solid Films 522 (2012) 30-32.

[179] Chafai M., et al., Raman scattering from LO phonon-plasmon coupled modes and Hall-effect in n-type silicon carbide 4H–SiC, Journal of Applied Physics 90 (2001) 5211-5215.

[180] Sartel C., et al., Control of Al-doping in 4H–SiC homo-epitaxial layers grown with a HMDS/TMA/P mixture, physica status solidi (a) 202 (2005) 550-554.

[181] Jellison Jr G. E. and Modine F. A., Parameterization of the optical functions of amorphous materials in the interband region, Applied Physics Letters 69 (1996) 371-373.

[182] Watanabe N., et al., Thermo-Optic Coefficients of 4H-SiC, GaN, and AlN for Ultraviolet to Infrared Regions up to 500° C, Japanese Journal of Applied Physics 51 (2012) 112101.

[183] Cai J., et al., High-performance 4H-SiC-based pin ultraviolet photodiode and investigation of its capacitance characteristics, Optics Communications 333 (2014) 182-186.

[184] Poggi A., et al., Effects of heating ramp rates on the characteristics of Al implanted 4H-SiC junctions, Applied physics letters 88 (2006) 162106.

[185] Mitra S., et al., Deep-level transient spectroscopy study on double implanted n+–p and p+–n 4H-SiC diodes, Journal of applied physics 95 (2004) 69-75.

[186] Brezeanu G., et al., Numerical and analytical study of 6H-SiC detectors with high UV performance, Proceedings of Semiconductor Conference, 2002.

[187] Silvaco Atlas User's Manual, Device Simulation Software; 17 October 2013.

[188] Della Corte F.G., et al., Simulation and experimental results on the forward J–V characteristic of Al implanted 4H–SiC p–i–n diodes, Microelectronics Journal 38 (2007) 1273-1279.

[189] Roschke M., et al., Electron mobility models for 4H, 6H, and 3C SiC [MESFETs], Electron Devices, IEEE Transactions on 48 (2001) 1442-1447.

[190] Pezzimenti F., Modeling of the steady state and switching characteristics of a normally off 4H-SiC trench bipolar-mode FET, Electron Devices, IEEE Transactions on 60 (2013) 1404-1411.

[191] Li X., et al., On the temperature coefficient of 4H-SiC BJT current gain, Solid-State Electronics 47 (2003) 233-239.

[192] Lindefelt U., Doping-induced band edge displacements and band gap narrowing in 3C–, 4H–, 6H–SiC, and Si, Journal of applied physics 84 (1998) 2628-2637.

[193] Jaeger R.C., et al., Simulation of impurity freezeout through numerical solution of Poisson's equation with application to MOS device behavior, Electron Devices, IEEE Transactions on 27 (1980) 914-920.

[194] Cole D.C., et al., Accounting for incomplete ionization in modeling silicon based semiconductor devices, Low Temperature Semiconductor Electronics, 1989, Proceedings of the Workshop on. IEEE, 1989.

[195] Megherbi M. L., et al., Analysis of different forward current–voltage behaviours of Al implanted 4H-SiC vertical p–i–n diodes, Solid-State Electronics 109 (2015) 12-16.

List of Publications

1. S. Santangelo, G. Messina, A. Malara, N. Lisi, T. Dikonimos, L. Ortolani ,V. Morandi, G. Faggio, Taguchi optimized synthesis of graphene films by copper catalyzed ethanol decomposition, Diamond & Related Materials, 41, 2014, 73–78, ISSN: 09259635.

2. T. Polichetti, F. Ricciardella, M.L. Miglietta, F. Fedi, R. Miscioscia, E. Massera, G. Di Francia, M.A. Nigro, G. Faggio, A. Malara, G. Messina,Graphene-based Schottky device detecting NH_3 at ppm level in environmental conditions, Procedia Engineering (ISSN 1877-7058). - EUROSENSOR 2014

3. C. Milone, E. Piperopoulos, M. Lanza, S. Santangelo, A. Malara, E. Mastronardo, S. Galvagno, Influence of Cobalt Phase on the Growth of MWNTs with High Efficiency, Nanomaterials and Nanotechnology, 4, 2014, ISSN: 18479804.

4. S. Santangelo, E. Piperopoulos, G. Faggio, A. Malara, E. Fazio and C. Milone, Micro-Raman Analysis of Three-Dimensional Macroporous Sponge-Like Network of Carbon Nanotubes under Tension, Journal of Physical Chemistry C, 118 (25), 2014, 13912–13919.

5. P. Frontera, A. Malara S. Stelitano, E. Fazio, F. Neri, L. Scarpino, P. L. Antonucci, S. Santangelo, A new approach to the synthesis of titania nano-powders enriched with very high contents of carbon nanotubes by electro-spinning, Materials Chemistry and Physics 153 (2015) 338-345.

6. G. Faggio, A. Capasso, A. Malara, E. Leoni, M. A. Nigro, S. Santangelo, G. Messina, Th. Dikonimos, F. Buonocore, N. Lisi, Fast growth of polycrystalline graphene by the chemical vapor deposition of ethanol on copper, IEEE-Xplore, DOI: 10.1109/NMDC.2014.6997424 - IEEE NMDC 2014

7. T. Polichetti, F. Ricciardella, F. Fedi, M. L. Miglietta, R. Miscioscia, E. Massera, G. Di Francia, M. A. Nigro, G. Faggio, A. Malara and G. Messina Graphene-Si Schottky diode in environmental conditions at low NH_3 ppm level, IEEE-Xplore, DOI: 10.1109/NMDC.2014.6997412. - IEEE NMDC 2014

8. A. Capasso, T. Dikonimos, F. Sarto, A. Tamburrano, G. De Bellis, M.S.Sarto, G. Faggio, A. Malara, G. Messina, N. Lisi, Nitrogen-doped graphene films from chemical vapor deposition of pyridine: Effect of process parameters on the electrical and optical properties, Beilstein Journal of Nanotechnology, 6 (2015) 2028-2038.

9. A. Malara, S. G. Leonardi, A. Bonavita, E. Fazio, G. Neri, F. Neri, S. Stelitano and S. Santangelo, Origin of the different behavior of some platinum decorated nanocarbons towards the electrochemical oxidation of hydrogen peroxide, Journal of Electrochemical Society, under review.

10. P. Frontera, A. Malara, S. Stelitano, G. Leonardi, E. Fazio,P. L. Antonucci, G. Neri, F. Neri and S. Santangelo, Characterisation and H_2O_2 sensing properties of TiO_2-CNTs/Pt electro-catalysts, Materials Chemistry and Physics, 170 (2016) 129-137.

11. A. Malara, G. Faggio, G. Messina, S. Rao, F. G. Della Corte, Optical characterization of variously doped 4H-SiC for optoelectronic devices, submitted.

12. A. Malara, G. Faggio, G. Messina, S. Rao, F. G. Della Corte, Characterization of 4H-SiC addressed to thermo-optic effect at fiber-optic communication wavelength, submitted.

Acknowledgments

There are many people who contributed to my personal and professional development during my PhD study and undoubtedly all of them deserve my acknowledgments.

Firstly, I would like to express my appreciation to my advisor Prof. Francesco G. Della Corte for his professionalism, availability and help throughout this work..

My deepest gratitude also goes to Prof. Giacomo Messina for his guidance, precious discussions, valuable contributions and for sharing with me his knowledge and experience.

I am especially grateful to Prof. Giuliana Faggio for her constant support, availability, scientific contributions and, furthermore, for sharing with me not only everyday laboratory life but everything happened in the last three years.

Sincere thanks go to Prof. Saveria Santangelo for her scientific suggestions, encouragements and for introducing me to the world of academic research.

Very special thanks go to Dr. Andrea Gnisci for his endless availability, precious help in device simulations and daily support during the last months.

I would also like to thank the group members of the Enea Portici Research Center who have contributed to this work of thesis providing inspiring ideas, advices and assistance during my activity in their laboratories.

I wish to express my acknowledgement to Prof. Giovanni Neri for his availability and help, giving to me the opportunity to carry out part of the experimental work in his laboratory at the University of Messina.

Finally, big thanks go to my long-life friends and to my PhD colleagues for their continual encouragements and kind words.

Last but not least, I would like to thank my family, especially my parents and my sister, for their unique support and endless love.

Thank you everyone,

Angela